Doctoral Dissertation
博士論文

Advancement of Millimeter-wave Polarization Modulator and Millimeter-wave Polarization Oscillation Search for Ultralight Dark Matter

（ミリ波偏光変調器の進展と
ミリ波偏光振動観測による超軽量暗黒物質の探索）

A dissertation submitted for the Degree of Doctor of Philosophy
August 2023

令和５年８月博士（理学）申請

Department of Physics, Graduate School of Science,
The University of Tokyo

東京大学大学院理学系研究科
物理学専攻

Kyohei Yamada
山田 恭平

Abstract

In this dissertation, we present two primary research products that extend and broaden the scientific reach of millimeter-wave astrophysics. First, we present the development of polarization modulators using a 0.5 m diameter cryogenic continuously rotating half-wave plate (CHWP) for the cosmic microwave background (CMB) polarization experiment, the small aperture telescopes (SATs) of the Simons Observatory (SO). The SATs precisely measure the large angular scale CMB power spectrum and search for the signal of the primordial tensor perturbation, which could be driven by the rapid expansion of the early universe called inflation. The CHWP modulator is a powerful tool for the CMB polarization measurements at large angular scales, mitigating the atmospheric $1/f$ noise and the instrumental systematics in polarization measurements. This work advances the methodologies for characterizing the polarization modulator, and introduces techniques for efficient operation. The three CHWP modulators we built and evaluated are being deployed in Chilean observation site. The scientific observations are expected to start in 2024. Our CHWP modulator development contributes not only to the SO project, but also to the design of future experiments such as CMB-S4. Second, we describe a search for ultralight dark matter. The ultralight pseudo-scalar field that couples to photons through the Chern-Simons term, called axion-like particles (ALPs), is one of the candidates for the dark matter. The ALP dark matter induces an oscillation of polarization angle of linearly polarized light traveling through the ALP background. We search for the ALP-induced polarization oscillation of the light from the Crab Nebula, the brightest polarized astronomical source in the millimeter wave. We use data acquired by the Polarbear experiment at 150 GHz from 2015 to 2016 for the purpose of calibrating the CMB polarization measurements. The polarization angle measurements of the Crab Nebula are extensively studied with systematic error tests and internal consistency tests to check their robustness before the oscillation spectra are examined. This work advances the methodologies for the calibration of polarization angle and the understanding of the systematic errors. To the best of our knowledge, this work provides the most accurate measurements of the polarization oscillation of the Crab Nebula over the oscillation frequencies from $0.75\,\mathrm{year}^{-1}$ to $0.66\,\mathrm{hour}^{-1}$ with the median 95% upper bound of the amplitude $A < 0.065^\circ/\mathrm{sinc}(f/7.6\,\mathrm{day}^{-1})$. The corresponding median 95% upper bound of ALP-photon coupling is $g_{a\gamma\gamma} < 2.16 \times 10^{-12}\,\mathrm{GeV}^{-1} \times (m_a/10^{-21}\mathrm{eV})/\mathrm{sinc}(m_a/3.7 \times 10^{-19}\,\mathrm{eV})$ in the mass range from 9.9×10^{-23} eV to 4.8×10^{-19} eV. A polarization oscillation with an amplitude of 0.11° is found at two correlated frequencies of $1/61\,\mathrm{day}^{-1}$ and $1/52\,\mathrm{day}^{-1}$ with global significance level of 2.5σ. The corresponding ALP masses are 7.8×10^{-22} eV and 9.2×10^{-22} eV, respectively. The possibilities of the residual systematics and the intrinsic variability of the Crab Nebula have been considered, resulting in no clear evidence for either of them. Interpreting this as an ALP signal leads to significant tension with other bounds. Future measurements with more statistics will give an improved interpretation for it. In summary, this dissertation presents significant advances in the instrumentation, methodology, and scientific exploitation of the millimeter-wave polarimetry.

Author's contribution

This dissertation is written based on the experimental activities within the Simons Observatory collaboration and the Polarbear collaboration. The experimental apparatus described in chapter 2 is developed, integrated, and managed by the Simons Observatory collaboration and the Polarbear collaboration, where the author contributed to the development and integration of the cryogenic continuously rotating half-wave plate polarization modulators (CHWP) of the small aperture telescopes. The CHWPs described in chapter 3 is developed within the Simons observatory collaboration. The author is one of the primary contributors for the development and evaluation of the CHWPs, and is responsible for all the contents described there. For the study described in chapter 5, the author is the primary contributor for the analysis and is responsible for all the contents described there. The development of the experimental apparatus and the observations were made by the Polarbear collaboration and were not contributed by the author. The tools for time-domain analysis and map-domain analysis used in chapter 5 were developed by the Polarbear collaboration and used in various analysis in common.

Preface

This dissertation describes the development of the key technology for the millimeter-wave polarimetry, the development of the cryogenic half-wave plate polarization modulator, and the scientific exploitation from the millimeter-wave polarimetry, the search for the axion-like particles from the precise polarimetry of the Crab Nebula.

This dissertation is structured as follows. Chapter 1 describes the physics of millimeter-wave polarization measurements, especially the polarization of the cosmic microwave background (CMB) as a probe for new physics. Chapter 2 provides a review of the modern CMB polarization experiments and their strategies. Chapter 3 discusses the development of the polarization modulator for the CMB experiment, which is a key technology for the precise measurement at large angular scales. Chapter 4 provides review of the ultralight dark matter especially the axion-like particle (ALP). Chapter 5 discusses the search for the ALP from the polarization oscillation measurements of the Crab Nebula at millimeter waves. Chapter 6 discusses the research impact and conclusion of this dissertation.

Acknowledgements

First of all, I would like to thank my advisor, Akito Kusaka. I am truly grateful to Akito for believing in me and accepting me from the Ph.D. program, and for giving me the opportunity to work on important research topics. I have always been inspired by Akito's attitude and philosophy toward research, his kind support for everyone, and his deep insight into all the aspects of the research, including science, hardware development, and data analysis.

The development of the cryogenic HWP modulator for the small aperture telescopes of the Simons Observatory experiment was a team-effort with many colleagues. Yuki Sakurai taught me all about the HWP development, working principle, design, cryogenics, and planning for experiments. The discussions and technical advice from the pioneers of the SO HWP modulator, Bryce Bixler, Peter Ashton and Charles Hill were essential. The advanced control of the HWP modulator was possible thanks to Bryce Bixler. The advancement of the motor drive technique and the detailed performance evaluation was possible thanks to Junna Sugiyama. The precise HWP angle encoder readout was developed by Haruki Nishino. The HWP motor drive electronics was designed by Paul Barton. Brian Koopman and Jack Lashner helped us with the implementation of monitoring and control software. Sean Adkins helped us in improving the control system. The validation of HWP modulators was supported by many Simons Observatory collaborators, Kam Arnold, Joelle-Marie Begin, Lance Corbett, Sam Day-Weiss, Nicholas Galitzki, Bradley Johnson, Aashrita Mangu, Lyman Page, Michael Randoll, Daichi Sasaki, Jake Spisak, Xue Song, Tran Tsan, Yuhan Wang, Paul Williams, and many others. I would also like to thank all the Simons Observatory Japan group members. I learned so much about the CMB experiments from the discussion in the Japan group.

I would like to thank all the collaborators of Polarbear. First, I would like to thank Adrian Lee, the PI of the Polarbear collaboration, for giving me an opportunity to work on data analysis. I would like to thank all the people who worked on the Simons Array experiment. I am truly grateful to the collaboration for kindly giving me the opportunity to analyze the data, even though I was not involved in the construction of the experimental apparatus, and I knew almost nothing about the CMB data analysis. I would especially like to thank Kevin Crowley, Yuyang Zhou and Tylor Adkins. Making the data analysis pipeline of the Simons Array experiment with you was a great experience for me, and I learned the CMB data analysis from the discussion through the work. I would like to thank all the people who worked on Polarbear experiment. My study using Polarbear data set was not possible without their tremendous effort, especially the well-managed data, the detailed observation log and the analysis software. I would like to thank Yuji Chinone for leading the data analysis telecon and always answering my basic questions on data analysis. I learned the basics of CMB data analysis from Yuji. I would like to thank Jake Spisak. Jake's previous axion study by CMB and his advice have been very helpful for my study. I would like to thank Satoru Takakura for always kindly answering my technical questions in detail and giving me insightful comments. I learned so much from Satoru's deep understanding of the experiment and analysis.

I would like to thank my UTokyo lab-mates: Kenji Kiuchi, Atsuto Takeuchi, Masaaki Murata, Yume Nishinomiya, Kana Sakaguri, Tomoki Terasaki, Kengo Iijima, Junna Sugiyama, Mio Sato, Singh Shrestha Yaman, Masaki Higuchi, and Daichi Sasaki. I had a great time in UTokyo thanks to you.

I would like to thank the support from XPS, WINGS Programs, the University of Tokyo, and the JSPS Research Fellowship for Young Scientists.

Finally, I would like to thank my family for their unconditional support.

Table of contents

List of figures

List of tables

Chapter 1

Physics through precise measurement of millimeter-wave polarization

The standard cosmological model, ΛCDM, includes new physics beyond the standard model of particle physics. Λ represents the dark energy responsible for the accelerated expansion of the universe. CDM stands for the Cold Dark Matter, which accounts for 25% of the energy content of the universe. Cosmic inflation, the exponential expansion of the space in early universe, is another important point of the standard cosmological model. Precise measurement of polarization at millimeter-wave could provide keys to solve all these mysteries. This chapter will serve as an introduction to the key concepts that underlie these efforts.

1.1 Standard Cosmology

The standard cosmology is based on the cosmological principle, the homogeneity and isotropy in the large scale of the universe. Under this assumption, the space-time of the universe is described by the Friedman-Robertson-Walker (FRW) metric. One of the most important predictions of the Big Bang model is the predictions of the cosmic microwave background.

The understanding of the universe has been confirmed by many measurements, including those of the cosmic microwave background (CMB), and the standard cosmological model, so-called ΛCDM model has been established with six parameters. The ΛCDM model includes an additional content of the matter called dark matter, and revealed the existence of cosmological constant (or dark energy). One of the candidates of the CDM is the ultralight dark matter especially the axion-like particle. The brief review of the ultralight dark matter is provided in chapter 4.

Despite ΛCDM's success, it has several issues including horizon problem, and flatness problem. Inflation, the rapid expansion of the early universe, is one of the most popular scenario that solves these problems [62]. This mechanism provides the primordial scalar perturbation, which explains the initial condition in the early universe, which evolved into the large scale structure. The inflation also predicts primordial tensor perturbation often referred to as primordial gravitational waves [2, 106, 105].

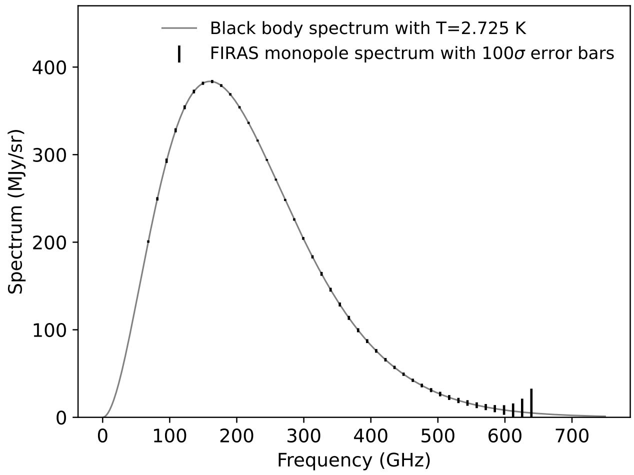

Fig. 1.1 Monopole spectrum measured by FIRAS [52] superposed on the fitted black body spectrum (Eq. 1.1). The uncertainties are 100 times magnified.

1.2 Cosmic Microwave Background

The Cosmic Microwave Background (CMB) is a remnant radiation left over from the Big Bang, which occurred around 13.8 billion years ago. It pervades the entire universe and is composed of photons that have been traveling through space since the universe was only 380,000 years old. These photons have been red-shifted due to the expansion of the universe, and is observable isotropically across the entire sky. The CMB was first discovered by Penzias and Wilson [144]. Figure 1.1 shows the spectrum of the CMB measured by the Far Infrared Absolute Spectrometer (FIRAS) on the Cosmic Background Explorer (COBE) satellite [158]. The spectrum is well described by the Planck distribution of the black body radiation

$$B(\nu, T) = \frac{2h\nu^3}{c^2} \frac{1}{\exp\left(\frac{h\nu}{k_B T}\right) - 1}, \tag{1.1}$$

with temperature of about 2.73 K [52].

1.3 Anisotropy of the Cosmic Microwave Background

The most powerful information of cosmology is obtained from the anisotropy in the CMB. The anisotropy in the CMB was first discovered by the Differential Microwave Radiometer (DMR) on the COBE satellite. and found that the angular power spectrum of anisotropy is consistent with the Gaussian statistics [22]. Figure 1.2 shows the anisotropy in the CMB measured by Planck satellite. We define the temperature fluctuation of the CMB at on the sky as $\Delta T(\hat{n}) \equiv T(\hat{n}) - \langle T \rangle$, where $\hat{n}$ is the direction on the sky, and $\langle T \rangle$ is the average temperature of the CMB, 2.73 K Since this is defined on the celestial sphere, we decompose

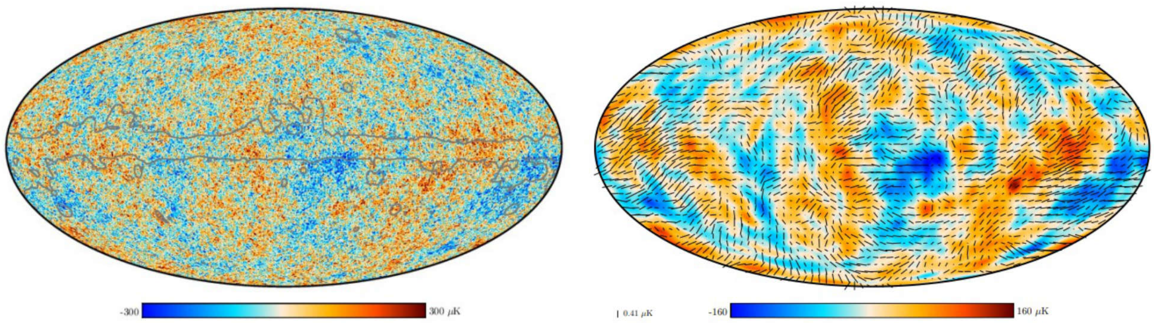

Fig. 1.2 Temperature anisotropy map (left) and polarization map (right) with the Planck satellite. Figure is taken from Planck Collaboration [147].

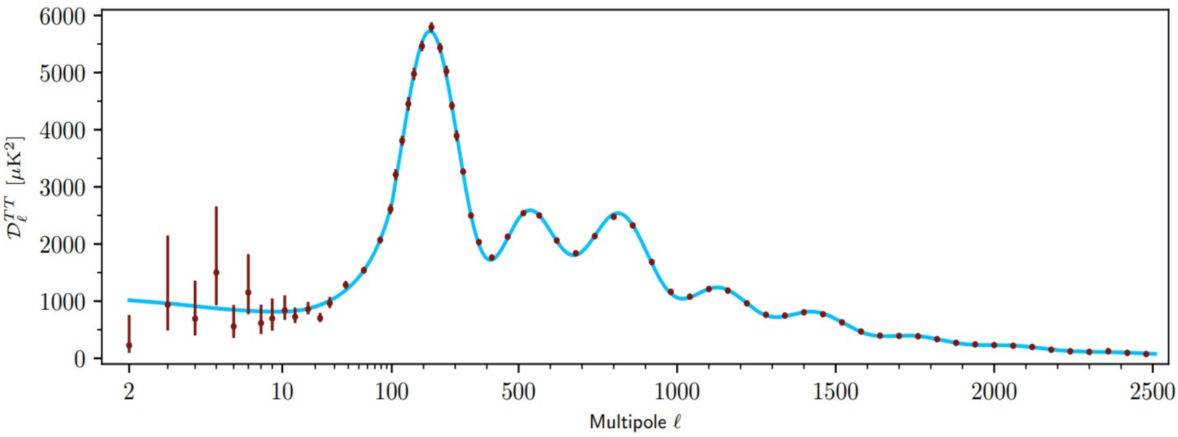

Fig. 1.3 Temperature power spectrum of the CMB. Figure is taken from Planck Collaboration [147]

it into the spherical harmonics as

$$\Delta T = \sum_{\ell=1}^{\infty} \sum_{m=-\ell}^{\ell} a_{\ell m} Y_{\ell m}. \tag{1.2}$$

As predicted by many theoretical models and measured by many experiments, the anisotropy follows largely Gaussian distribution. Therefore, the statistics is well characterized by their angular power spectrum as

$$C_\ell = \langle |a_{\ell m}|^2 \rangle \, , \tag{1.3}$$

where $\langle \cdot \rangle$ is the ensemble average. However, in the measurement of the anisotropy, there are only $2\ell + 1$ m's for given ℓ. This limited number of statistics imposes the limitation on how well we can estimate C_ℓ, and this limit is called cosmic variance. The cosmic variance of the estimator of C_ℓ is expressed as

$$\sigma\left(\hat{C}_\ell\right) = \sqrt{\frac{2}{2\ell + 1}} C_\ell. \tag{1.4}$$

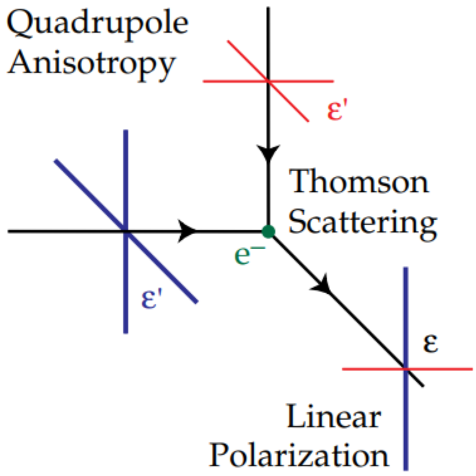

Fig. 1.4 Schematic representation of how Thomson scattering and quadratic anisotropy generate linear polarization. Figure is taken from Hu and White [73]

Figure 1.3 shows the angular power spectrum of the temperature fluctuation of CMB measured by Planck satellite. The series of peaks and troughs, acoustic peaks, in the temperature power spectrum is well described by the simple ΛCDM model and it imprints various physical processes. The detailed phenomenology of the CMB is reviewed in Hu and Dodelson [72]. In brief, the first peak informs us of the total energy density of the universe, the second tells us about the total baryonic matter of the universe, and the third is sensitive to the relative abundance of DM compared to baryonic matter. The most recent results from the Planck satellite provided a measurements of ΛCDM model in which only 16% of the matter in the universe is baryonic, with the remaining 84% accounted by DM.

1.4 Polarization of the Cosmic Microwave Background

In addition to the anisotropy of the temperature, the CMB also have fluctuations in its polarization. As shown in Fig. 1.4, the Thomson scattering in the recombination era with non-zero quadrupole temperature anisotropy generates the polarization. The polarization pattern of the CMB is decomposed into two independent modes of the E-modes and B-modes, the parity even patterns and the parity odd patterns respectively [204].

The important statistical behavior of E-modes and B-modes is that it is defined from the parity symmetry and is independent of the choice of coordinate system. The polarization of CMB is dominated by the E-modes patterns, primarily sourced from density (scalar) perturbation in the early universe [83, 204].

1.5 B-mode polarization

While the primordial scalar perturbation does not create B-mode polarization, the primordial tensor perturbations, the primordial gravitational waves, produce both E-mode and B-mode polarization patterns [82, 194]. These primordial B-modes have the largest amplitude at degree angular scales and are subdominant to E-modes. The rapid expansion of the early universe, called inflation, could produce

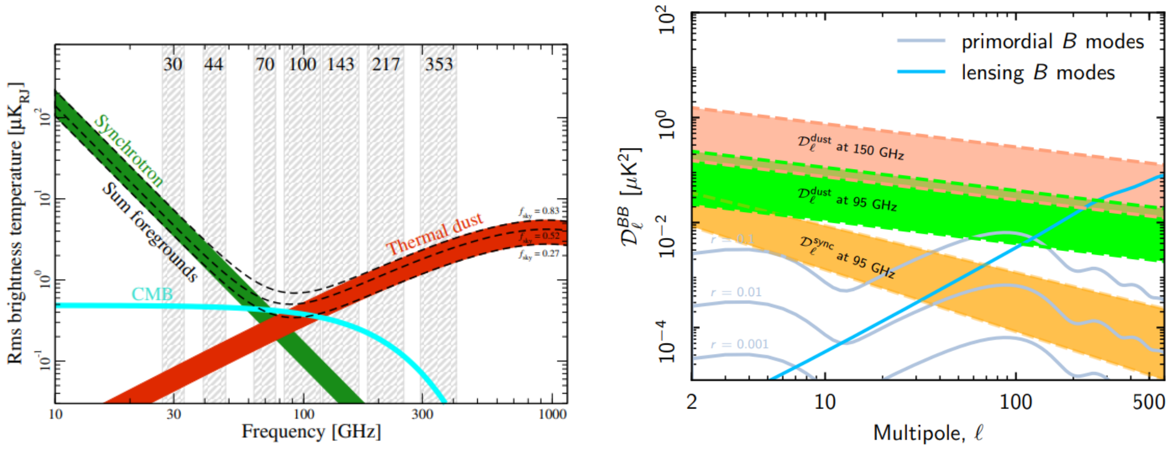

Fig. 1.5 Left: Spectrum of foreground emission. Right: Power spectrum of the foreground emission compared with the lensing B-mode spectrum and possible primordial B-mode spectrum. Both figures are taken from Planck Collaboration [148]

tensor perturbations [2, 106, 105]. The amount of the primordial tensor purturbation is characterized by adding a new parameter to the simplest ΛCDM model, the tensor-to-scalar ratio r.

Therefore, an accurate observation of primordial B-mode polarization would constrain models of the early universe and contribute to understanding the physics of grand unified theory (GUT) energy scales [167]. However, B-mode polarization is not solely produced by primordial tensor perturbations. Firstly, B-mode polarization is also produced from polarized galactic emission [136, 189], mainly from synchrotron and thermal dust (Fig. 1.5). Additionally, E-modes can be converted into B-modes through gravitational lensing, the lensing B-mode [203]. Separating B-mode polarization of the galactic foreground requires wide frequency coverage while efficient lensing B-mode separation requires high arc-minute angular resolution and large area of sky maps [92, 86, 168].

1.6 Current state of the field

The angular power-spectrum of the lensing B-mode signal was first detected by the POLARBEAR experiment [150], and other experiments also reported the measurements, which is summarized in Fig. 1.6. The search for primordial B-mode polarization is one of the major goals of the modern CMB experiments. Current best constraint on the tensor to scalar ratio is $r < 0.032$ at 95% confidence level [193]. The review of the modern CMB polarization experiments and their strategies are described in Chapter 2.

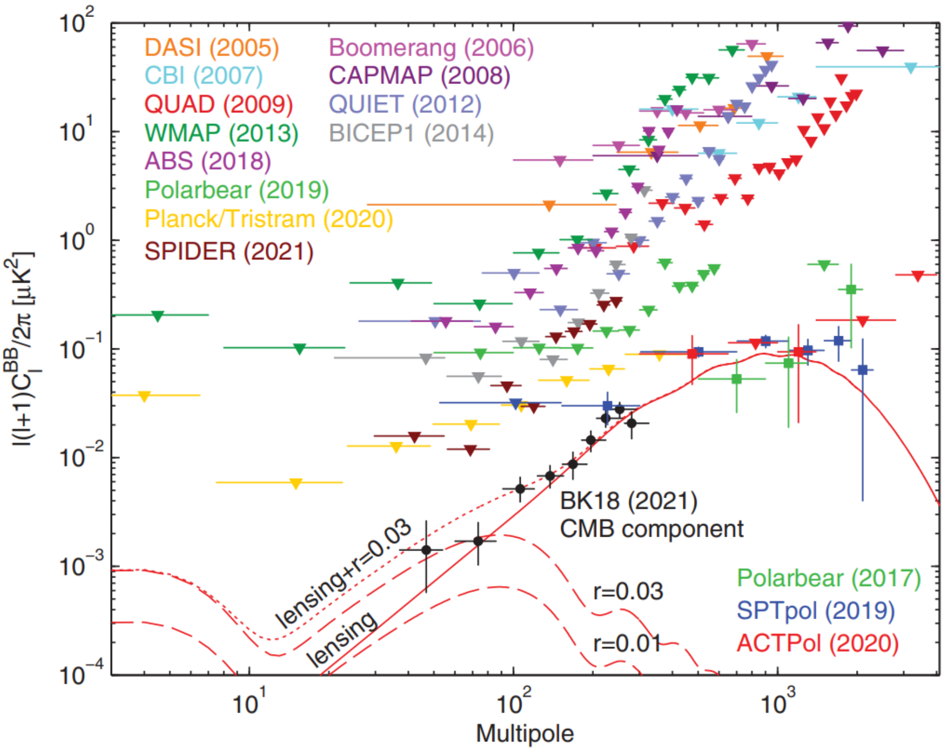

Fig. 1.6 Summary of the CMB *B*-mode polarization upper limits and detections. Figure is taken from [26]

Chapter 2

Review of the modern cosmic microwave background polarization experiments

The cosmic microwave background radiation (CMB) is the oldest detectable light in the universe, and is still observed isotropically in the entire sky [144]. The precise measurement of the CMB gives us rich information of the cosmology [158]. The CMB polarization is dominated by parity-even E-mode polarization from the density fluctuations of the universe. On the other hand, it is predicted that primordial gravitational waves from cosmic inflation produces parity-odd B-mode polarization mainly on degree angular scales in addition to E-mode polarization [194, 203].

Accurate observation of B-mode polarization at large angular scales would provide observational evidence of inflation and makes connection to reveal the physics of grand unified theory (GUT) energy scale [167]. However, there are other B-mode polarization sources besides the primordial gravitational waves: gravitational lensing [82, 203] and polarized galactic emission (foregrounds) [189] mainly from synchrotron and thermal dust. Efficient lensing B-mode separation requires high resolution and wide sky maps, and a wide frequency coverage is important for the foreground removal[92, 86, 168]. Therefore, modern CMB experiments are designed to observe a wide angular scales and a wide range of frequency bands. In addition, the statistical uncertainty is expected to be improve as increasing the number of detectors. Thus, the importance of the control of systematic uncertainties increases.

This chapter reviews the observation methods and instruments of the modern ground-based CMB polarization experiments, especially the Polarbear experiment and Simons Observatory experiment.

2.1 Observation site

The ground based CMB experiments have advantages on being able to employ larger number of detectors and larger primary mirrors for higher angular resolution, compared to the satellites experiments or the balloon-borne experiments. However, the millimeter wave emission from the atmosphere significantly limits the observation band, so called atmospheric window (Fig. 2.1). At millimeter and sub-millimeter wave the emission from water vapor and oxygen molecules are the primary source of the atmospheric

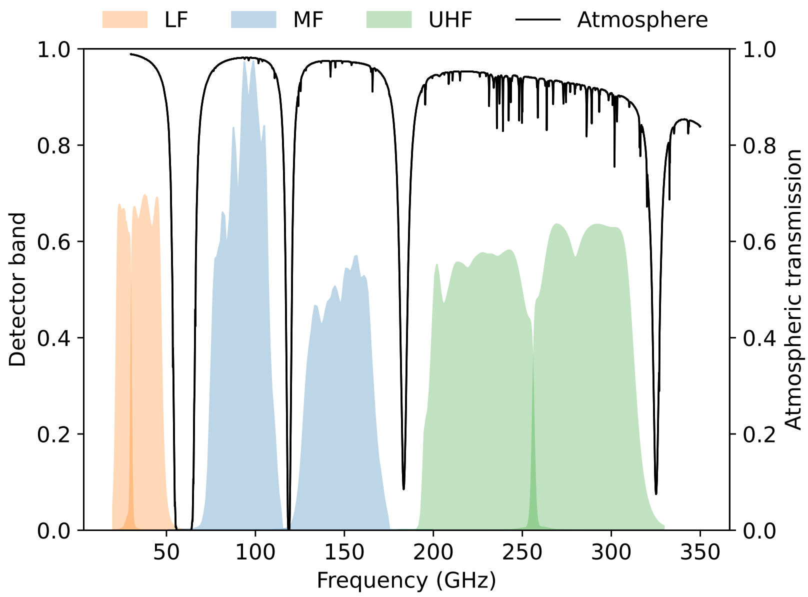

Fig. 2.1 The detector band of Simons Observatory [176] and the atmospheric transmission at PWV 1 mm.

emission. Therefore, the observation site of CMB experiments are chosen to be low atmospheric noise and stable atmospheric conditions. The precipitable water vapor (PWV) is the key parameter which characterizes the atmospheric emission (Fig. 2.2). The examples of the well-known CMB observation sites are the Atacama Desert at an altitude of 5,200 m in Chile [180], and the South Pole (altitude of 3,200 m, and average PWV of 0.5 mm.) [97]. Both the Simons observatory and POLARBEAR experiments are located at the Atacama dessert, Chile (Fig. 2.3), where the typical PWV is 1 mm.

2.2 CMB polarization experiments

This section provides an overview of the two ground based CMB polarization experiments, the POLARBEAR and the Simons Observatory.

POLARBEAR (The POLARization of the Background Radiation) experiment is a millimeter-wave polarimetry experiment designed to measure the B-mode polarization signal of the CMB on large and small angular scales [12]. Primordial gravitational waves produce B-modes at degree angular scales, whereas gravitational lensing generates them at sub-degree angular scales. The goal of measuring both sources of B-modes drives the design, location, and observation strategy of the experiments. The POLARBEAR employs total of 1274 transition-edge sensor (TES) bolometers to increase the instrumental sensitivity, and the observation band is centered at 148 GHz with 26% fractional bandwidth. The effective aperture size is 2.5 m in diameter and the angular resolution is 3.6′. The observations were conducted from 2012 through 2017. For the first two seasons, POLARBEAR observed three small $3^\circ \times 3^\circ$ patches of the sky focusing on sub-degree scale B-mode polarization [150, 149]. From third season to fifth season, POLARBEAR observed large patch (700 degree square area) of the sky [151, 153].

The Simons Observatory (SO) is a CMB polarization experiment at the Atacama Desert of Chile with the altitude of 5,200 m [6, 5]. In order to cover wide angular scales, the SO consists of three small

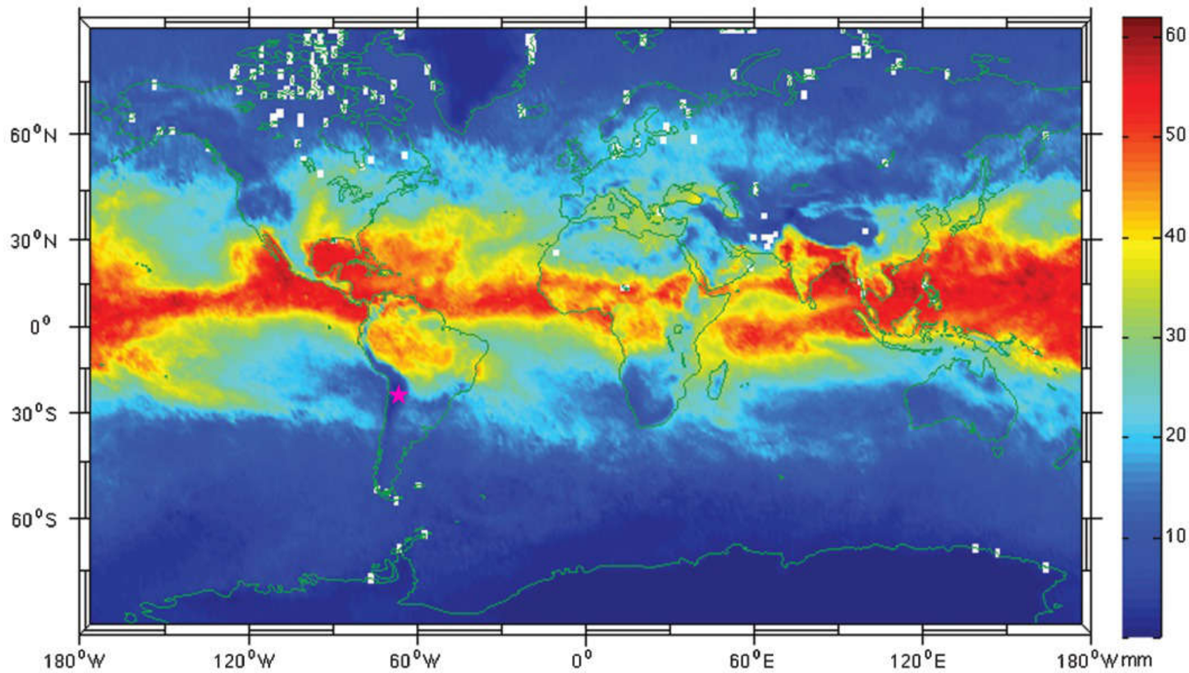

Fig. 2.2 The global distribution of PWV. The star is at the observation site of the Simons observatory and POLARBEAR. Figure is taken from Otárola et al. [135]. The data is obtained from the Atmospheric InfraRed Sounder (AIRS) database [14].

Fig. 2.3 The Huan Tran Telescope at Atacama Desert Chile.

aperture telescopes (SATs) with an aperture of 42 cm [8, 89] and one large aperture telescope (LAT) with an aperture of 6 m [57, 206, 138]. The combined arrays of the SATs and the LAT employ over 60,000 TES bolometers [66, 104, 117]. Each SAT has two frequency bands, thus covering a total of six frequency bands between 27-280 GHz at center frequency. Two SATs cover the middle frequency (MF) with center frequencies of 93 and 145 GHz and another SAT covers the ultra-high frequency with center frequencies of 225 and 280 GHz. There additional SATs are planned to be built, and one of the SAT will be developed by Japan group and observes at low frequency (LF) with center frequencies of 27 and 39 GHz. The SAT design is optimized to measure larger angular scale of $30 < \ell < 300$ with the 10% fractional sky coverage aiming to detect the primordial gravitational waves. The SATs employs a cryogenic rotating half-wave plate (CHWP) polarization modulator to realize an accurate large angular scale observation. The science observation is planned to start from 2024.

2.3 Telescope and optics tube

The section provides a brief review of the optical design of the CMB experiments and the actual optical systems of the CMB experiments. The telescopes with arrays of detectors are designed so that the all the incoming plane waves at different angles focus on different locations on the detector array. The plane where the detector array and all the focus exist is called focal plane. Therefore, all the detectors on the focal plane look at different points on the sky. The instantaneous angular scale which the telescope can observe is called field of view (FOV) of the telescope. The degree to which the incoming lights are not perfectly focused at the detectors is called aberrations.

As for the angular resolution, there is a fundamental limit to it due to the diffraction of light, called the diffraction limit. We design the optical system to be a diffraction-limited system in which the effect of the aberrations is sub-dominant to the effect of the diffraction. The smallest possible angular size is obtained from the width of the Airy pattern and approximately expressed as follows.

$$\sin\theta \simeq 1.22\,\lambda/D, \tag{2.1}$$

where λ is the wavelength, and D is the diameter of the aperture.

The optical system can be broadly divided into three categories: the refractive optics, reflective optics and the hybrid of them. The refractive optics consists only of refractive components, lenses. The small aperture telescopes of Simons Observatory [89, 8], BICEP and Keck Array, SPIDER [61] are the purely refractive CMB telescopes. The advantage of the refractive optics is its compactness and its axial symmetry which leads to smaller aberrations. The disadvantage of the refractive optics is that difficulty in fabrication. To achieve higher throughput and higher resolution, larger optics are desired, but making a large lens with high refractive and low loss material is not trivial, nor is the anti-reflective (AR) coating on the lens.

The reflective optics consists only of reflective components, mirrors. The advantage of the reflective optics is that it is easier to make larger optics and does not require AR coating. The disadvantage of the reflective optics is that it is more prone to aberrations due to its usually off-axis nature[1]. The larger aberration of the off-axis reflective optics is mitigated by the specific off-axis design, called Crossed

[1]On-axis reflective optics has low throughput due to its necessity of blocking the center portion of the FOV. Also, the support structure of the secondary mirror interferes with the beam, causing polarized side lobe contamination from the ground, sun, moon, or galaxy.

Dragone design [121, 43]. The Q/U Imaging ExperimenT (QUIET) experiment [155, 156], and the Atacama *B*-mode Search (ABS) experiment [100] are purely reflective CMB telescopes. The hybrid optics consist both the refractive optics and reflective optics. Typically, they use a large primary mirror to have a large aperture and high resolution, and then refractive optics to reduce aberrations. The POLARBEAR experiment [12], Simons Array experiment [181], and large aperture telescope of Simons Observatory are hybrid CMB telescopes with Crossed Dragone design.

Another aspect of optics which also affects the optical throughput is the transmission and emission of the optical components. To reduce the thermal emission from the optics, the optics tube of the modern CMB experiments are cooled from 50 K to 1 K. Therefore, to minimize heat on the optical components, we design the optics tube to block the IR radiation but allow mm-wave radiation to pass through.

Finally we describe the actual optical design of the POLARBEAR and the Simons Observatory. The telescope of POLARBEAR is called Huan Tran Telescope (HTT) (Fig. 2.3), and is an off-axis Gregorian-Dragone design and satisfies Mizuguchi-Dragone (MD) condition to minimize the beam distortion and cross-polarization [192]. The primary mirror is a monolithic mirror made of aluminum, 2.5 m in diameter, surrounded by a guard ring and the total diameter is 3.5 meter. The secondary mirror is 1.5 m in diameter, made of aluminum. The FWHM of the beam size is 3.6′ at 150 GHz. The diffraction-limited field of view is 2.3 degree. The telescope can scan in both azimuth and elevation direction with a maximum speed of 4 deg/sec. The cryogenic receiver is installed in the boom of the telescope. Figure 2.4 shows the cross sectional view of the POLARBEAR receiver and the components inside. The POLARBEAR employs an outer vacuum shell and the two thermal shells with the base temperature of 50 K and 4 K cooled by the Pulse Tube cooler [2]. The three stage Helium sorption fridge provides the 250 mK base temperature for the focal plane. The typical hold time is 36 hours. The foam window is used to maintain vacuum and cryogenic temperatures inside, while being transparent to microwave radiation. A series of IR blocking filters reduce the thermal loading. The cryogenic stepping half-wave plate (CHWP) is cooled to ~80 K, which rotates at 11.5 degree steps between observation to rotate the incident polarization and mitigate systematic uncertainty. The CHWP was moved frequently during the first two seasons, however was fixed after the third season that this work focuses on. Along with the cold aperture stop, the three anti-reflection coated lenses re-image the focus on the flat focal plane with the diameter of 19 cm.

The Simons Observatory consists of a large aperture telescope (LAT) and small aperture telescopes (SATs) [57]. The LAT is composed of two 6 m mirrors with the off-axis Crossed Dragone design (Fig. 2.5), and the angular resolution is 1.2′ at 145 GHz [138]. The LAT receiver shown in the right panel of Fig. 2.5 employs initially 7 dichroic optics-tubes [206]. LAT has 6 frequency bands and each optics-tube has two frequency bands of LF, MF, and UHF bands. The number of optics-tubes is planned to be expanded up to 13.

The SATs target large angular scales with FOV of 35°, aperture size of 42 cm, and angular resolution of 17′ at 145 GHz. The nominal observatory consists of three SATs and Each SAT has two frequency bands with bandwidths ranging from 20% to 45% of the central frequency. The radiation of ground or the stray light is to be diffracted at least twice by the ground shield, co-moving shield and the forebaffle. Figure 2.7 shows the cross-section view of the SAT receiver. Each SAT employs cryogenic continuously rotating half-wave plate [202] at PTC1 stage (=50 K) in front of the aperture stop, between the alumina IR blocking filters with multi-layer AR coatings [160]. The cryogenic optics tube [88] contains the 42 cm

[2]Cryomech PT-415 https://www.cryomech.com/products/pt415/

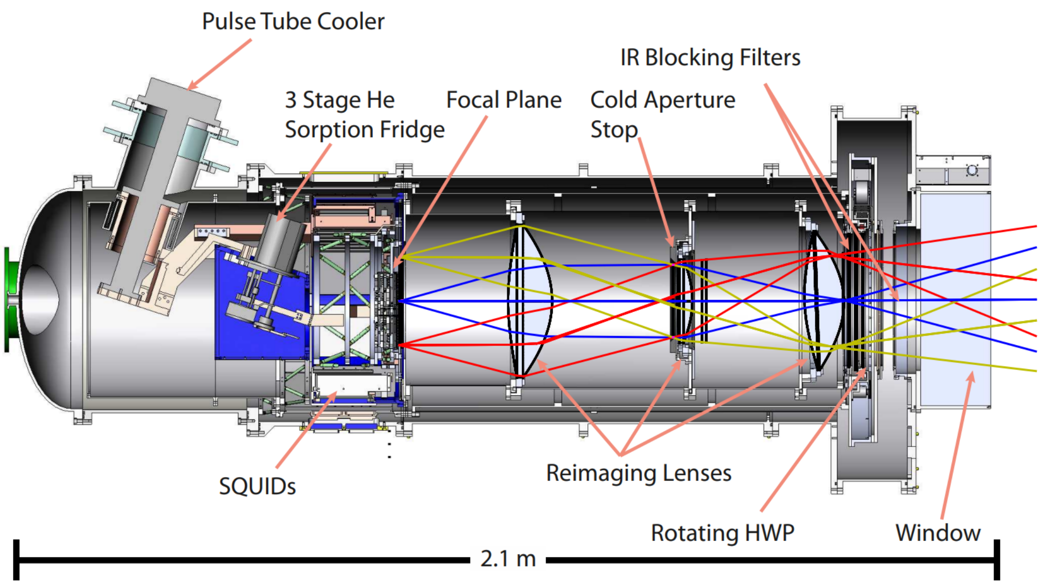

Fig. 2.4 A cross-section drawing of the POLARBEAR receiver. Figure is taken from Kermish et al. [85]

aperture stop, three silicon lenses with meta-material AR coatings [59], low pass filters and optical baffles. The entire optics tube is cooled to 1 K.

2.4 Focal plane and detector readout

The sensitivity of modern CMB experiment is reaching photon-noise limited regime, meaning that their sensitivity is limited by the statistical fluctuation of photon numbers not by the detector noise. In this regime, the most effective way to improve the sensitivity of experiment is to increase the number of detectors. Therefore, the sensitivity of modern CMB experiments have been driven by the increase of the number of detectors. The increase of the number of detectors is achieved by the development of arrays of superconducting transition-edge sensor (TES) connected to the multiplexed readout electronics. To reduce the thermal noise of the detectors, the detectors of the modern CMB experiments are cooled to sub-Kelvin.

The POLARBEAR telescope employs 637 dual-polarization pixels on the focal plane [11, 131] (Fig. 2.8). Each pixel has a dual-polarization antennas. The anti-reflection coated silicon lenslet above the antennas focuses the incoming light onto the antennas. The power from the antennas is routed through the band pass filters defining our observation band at 148 GHz and deposited on a thermally isolated island containing a transition edge sensor (TES) bolometer. The power changes the current through the TES bolometer. The current is measured after the amplification using a superconducting quantum interference device (SQUID). The signals from the SQUID are read out by the digital frequency domain multiplexer (DfMux) system and digitized at a sample rate of 190 Hz.

The SAT of SO employs about 10,000 TESs each, and LAT of SO employs about 30,000 TESs. Each pixel has dual-band and dual-polarization sinuous antennas. The TESs are read out with microwave SQUID multiplexing (μmux) [117].

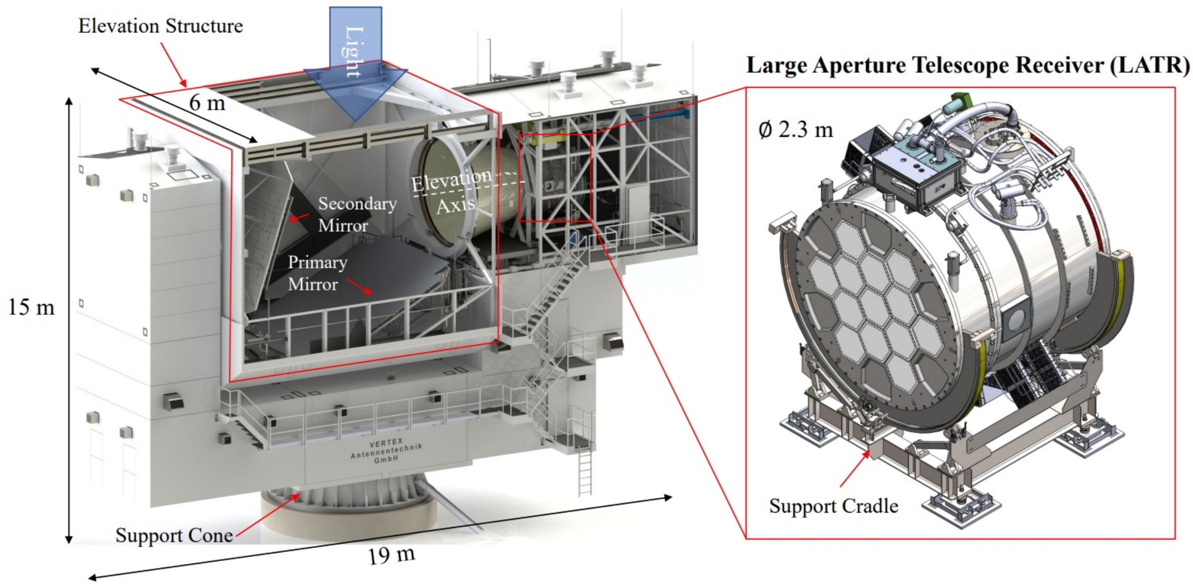

Fig. 2.5 Large aperture telescope and large aperture telescope receiver. Figure is taken from Xu et al. [201].

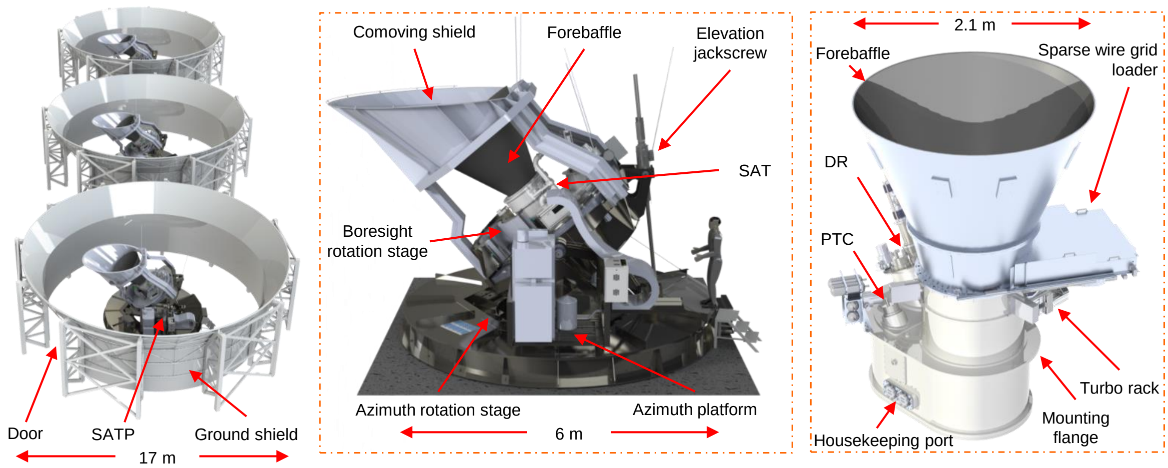

Fig. 2.6 Left: A schematic of the array of three SATs. Each SAT receiver is mounted to a SATP and surrounded by a ground shield. Center: Detailed view of the SATP with the receiver mounted as reference. Right: SAT receiver with the forebaffle and an automated sparse wire grid calibrator [127]. The sparse wire grid is inserted in front of the window to perform a number of calibrations including relative and absolute polarization angle, responsivity, and polarization efficiency, in between routines of CMB observations. Figure is taken from Galitzki et al. [58]

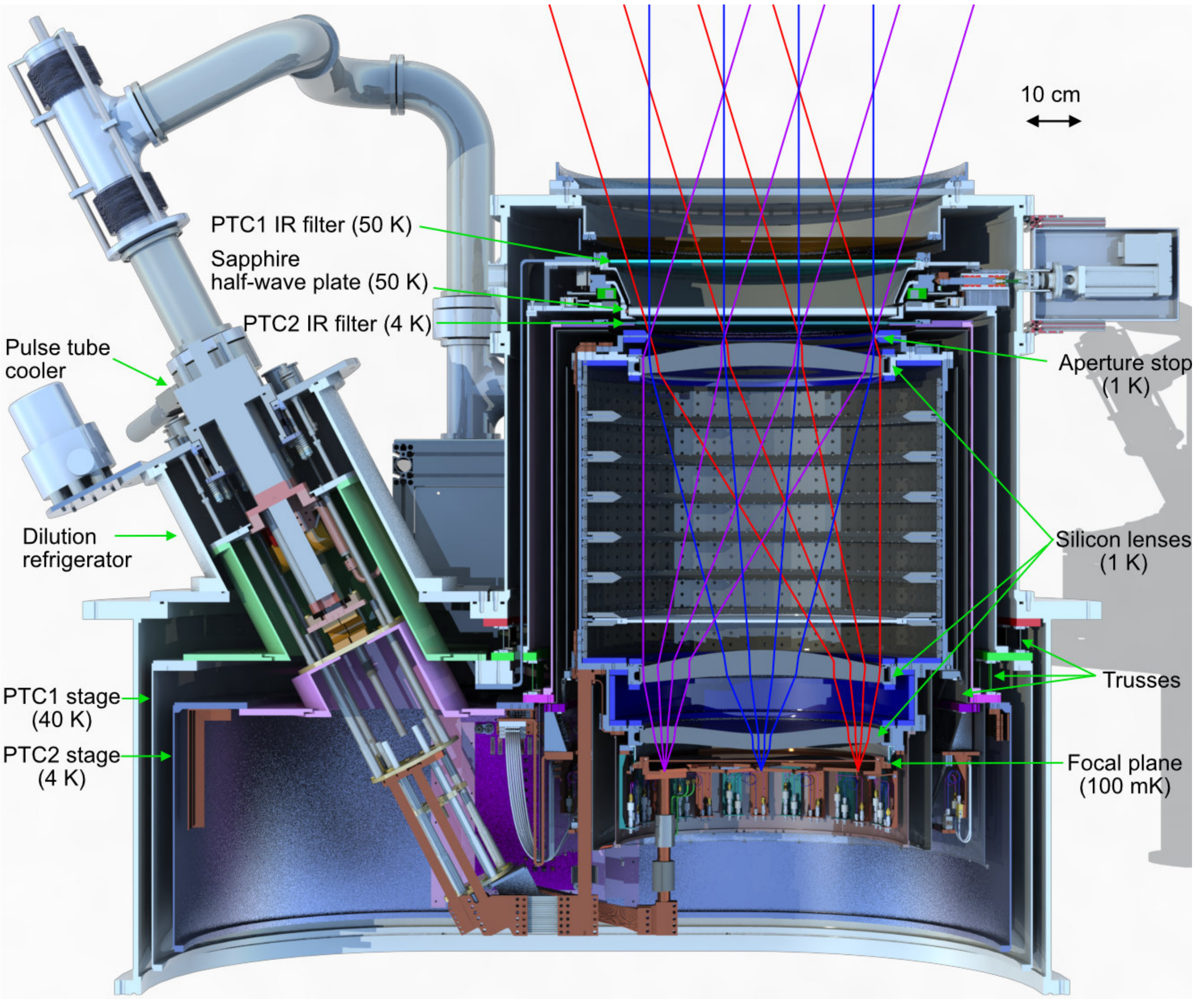

Fig. 2.7 The computer-aided design (CAD) cross-section of the small-aperture telescope's receiver. The superposed optical ray traces [114] are approximations and for illustrative purposes only. The SAT receiver employs an outer vacuum shell and the two thermal shells cooled by the pulse tube cooler (PTC). We refer to the two thermal shells as the PTC1 stage and the PTC2 stage. The nominal temperature of each stage is 45 K and 4 K, respectively. The CHWP rotation mechanism and PTC1 IR blocking alumina filter are located on the PTC1 stage and the PTC2 IR blocking alumina filter is located on the PTC2 stage. Figure is taken from Yamada et al. [202]

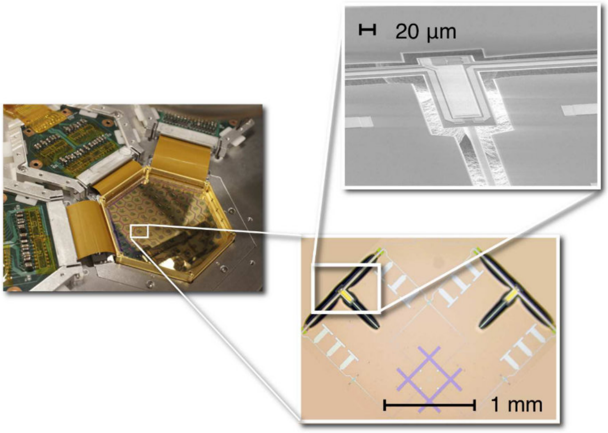

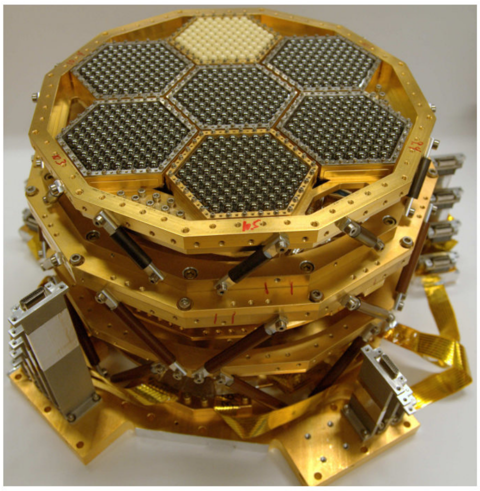

Fig. 2.8 A photograph of the fully assembled focal plane of POLARBEAR telescope. Figure is taken from Kermish et al. [85]

	EBEX[90] (2012, 2013)	ABS[99] (2012-2013)	POLARBEAR [186] (2014-2017)	SA[69, 68] (2020-)	SO [202] (2023-)
Diameter	240 mm	324 mm	280 mm	440 mm	505 mm
Temperature	4 K	300 K	300 K	300 K & 50 K	50 K
Band	130-170 GHz 220-290 GHz 360-450 GHz	140-170 GHz	150 GHz	90-150 GHz	20-30 GHz 90-150 GHz 200-300 GHz

Table 2.1 Comparison of continuously rotating half-wave plate based polarization modulators for CMB observation. The observation period with the polarization modulator is shown.

2.5 Polarization modulator

In addition to increasing sensitivity, CMB experiments need to minimize its systematic effects. Two of the most important systematic effects are the 1/f noise, which degrades the sensitivity to the large scale structure of CMB, and the instrumental polarization. One of the techniques widely used in modern CMB polarization experiments to control these systematics is the polarization modulation. Various modulation techniques have been used for mitigating these effects in CMB experiments [78, 132, 102, 19, 34, 23, 156, 126, 28, 119, 101, 65], we highlight the method of polarization modulation, especially those based on the rapidly rotating half wave plate (HWP) [79, 115, 90, 99, 69, 80, 68]. The rapid modulation of incident polarization by a HWP is one of the most promising techniques to separate the large scale CMB B-mode polarization signal from large unpolarized atmospheric $1/f$ noise, while using an instrument with large optical throughput and a large number of multi-chroic pixels. The selected list of demonstrated HWP polarization modulation are listed in Table 2.1.

POLARBEAR started the observation with the rapid polarization modulator from the 3rd season (2015), the warm continuously rotating half-wave plate (HWP) polarization modulator is installed at the prime focus of the HTT (Fig. 2.9). Ideally, the modulator should be the first optical element on the most sky side to mitigate the intensity to polarization leakage. The position of the prime focus was chosen due to the availability of the sapphire plate at the time and the optical conditions. The HWP is 28 cm in diameter,

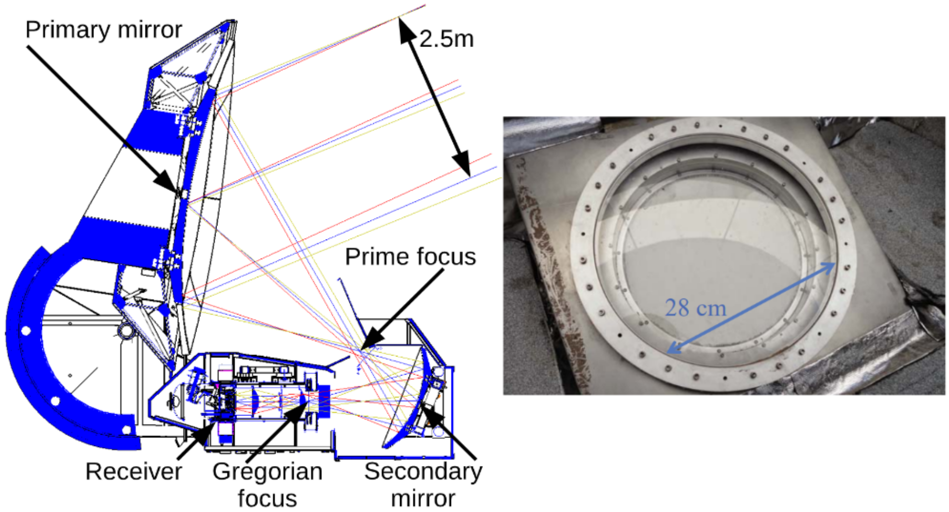

Fig. 2.9 Reft: CAD cross-section and ray-trace of the POLARBEAR telescope. The POLARBEAR WHWP is located at prime focus. Ritht: Photograph of the POLARBEAR WHWP at prime focus. Figures are taken from Takakura et al. [186] and Hill et al. [69], respectively.

single sapphire plate with single layer anti-reflection coating. The detailed optical performance can be found in [185, 55]. The detailed requirements, design, laboratory-performance of the cryogenic HWP modulators for SATs are described in Chapter 3.

2.6 Experimental sensitivity

Experimental sensitivity can be described by the statistical uncertainty of the CMB power spectrum C_ℓ per single angular mode, derived by Knox formula [92]

$$\Delta C_\ell = \left(C_\ell + \frac{N_\ell}{B_\ell^2} \right) \sqrt{\frac{2}{(2\ell+1) f_{\rm sky}}}, \tag{2.2}$$

where $f_{\rm sky}$ is the ratio of the observed sky patch to the entire sky, therefore $(2\ell+1)f_{\rm sky}$ is the effective number of modes for ℓ.

$$N_\ell = N_{\rm white} \left[1 + \left(\frac{\ell_{\rm knee}}{\ell} \right)^\alpha \right] \tag{2.3}$$

The white noise level is given by the square of map depth $N_{\rm white} = \sigma_{\rm map}^2$. The map depth $\sigma_{\rm map}$ is a noise in sky-map domain in unit μK·arcmin. In reality, the noise is not completely white, it increases at low frequency. This is called $1/f$ noise and the fluctuation of atmospheric radiation or the instruments are the origin. The low frequency noise translates into the noise in large angular scale through the scan strategy of the experiment, and is characterized by the knee scale $\ell_{\rm knee}$, and the scaling factor α.

$$B_\ell = \exp\left(\frac{\ell(\ell+1)\sigma_b^2}{2} \right) \tag{2.4}$$

is the beam transfer function and σ_b is the angular resolution of the experiment. The sensitivity exponentially degrades at angular scales smaller than the angular resolution. Therefore, the key parameters that differentiates the sensitivity of experiments are the map depth σ_{map}, knee scale ℓ_{knee}, scaling factor α, and beam size σ_b.

Figure 2.10 shows the angular spectrum of the CMB polarization and the projected noise spectrum of the Simons observatory experiment [190] and the achieved noise spectrum of POLARBEAR experiment [151]. The B-mode power spectrum from the primordial B-mode is larger at large angular scale. The estimated noise spectrum is at 145 GHz and beam size of 17 arcmin FWHM [8] for SAT, 1.2 arcmin FWHM [206] for LAT are assumed. As can be seen from Fig. 2.10, lowering the white noise level is certainly important, but it is also crucial to control of the noise in large angular scale to search for the primordial B-modes of CMB, and the polarization modulator plays important role there.

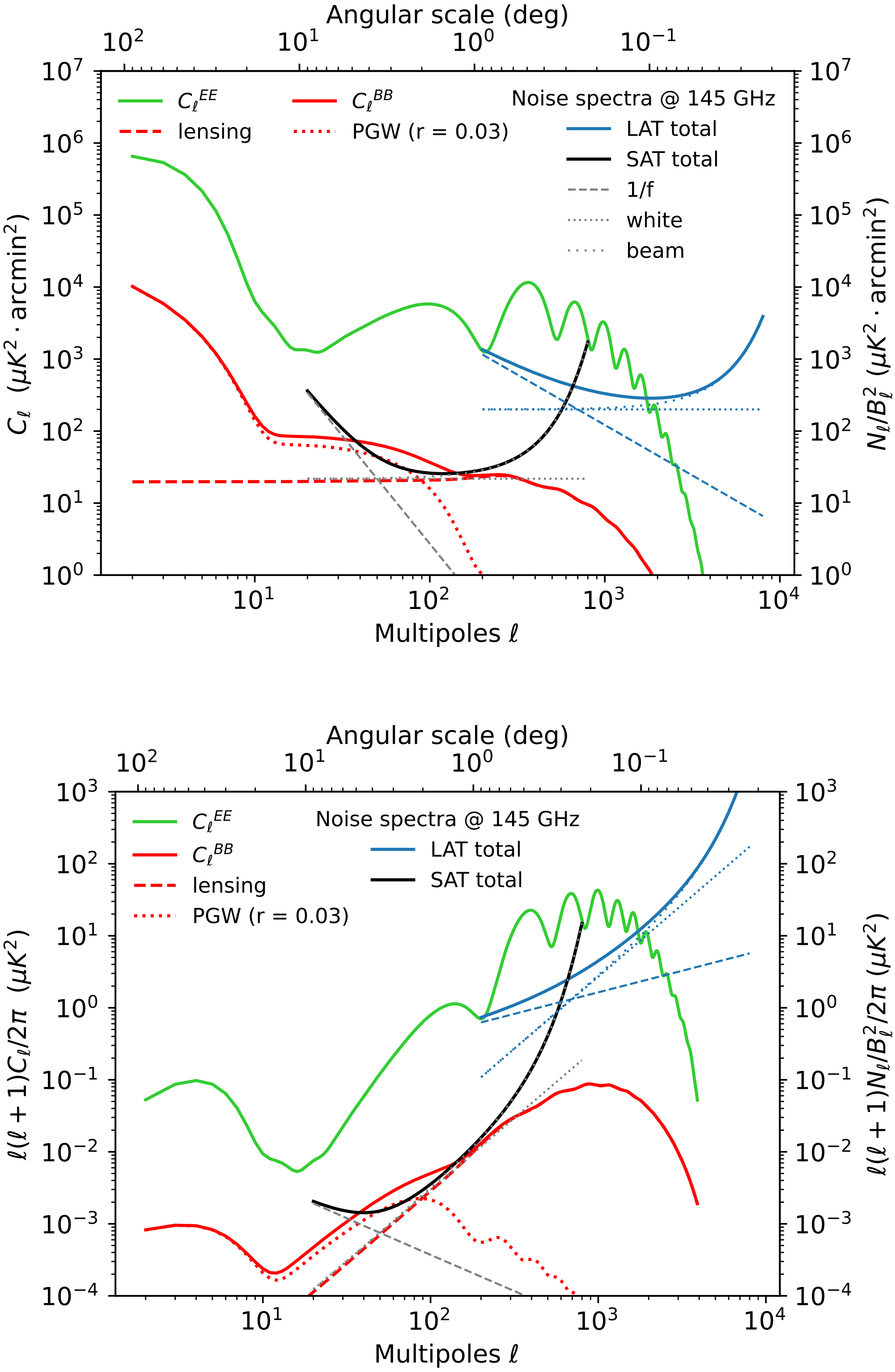

Fig. 2.10 CMB B-mode auto spectrum compared with the noise spectrum of the small aperture telescopes (SAT) and the large aperture telescope (LAT) of the Simons Observatory experiment. The green and red CMB spectra are generated by CAMB [9] with tensor to scalar ratio $r = 0.03$. The black and blue noise spectra are the baseline values at 145 GHz [190].

Chapter 3

Cryogenic half-wave plate based polarization modulator for Simons Observatory

This chapter describes the requirements, hardware design, and laboratory performance of the SO SAT CHWP rotation mechanism for the MF and UHF frequency bands. This chapter overlaps substantially with K. Yamada, B. Bixler and Y. Sakurai et al [202].

3.1 Half-wave plate polarimetry

Observing primordial B-modes requires nK sensitivity, especially at degree angular scales. The challenge for ground-based polarization experiments is to characterize faint signals in the presence of comparably large-amplitude unpolarized atmospheric fluctuations, in addition to polarized emission from the atmosphere [184, 146], the ground, and the instruments itself. While the atmospheric noise is mitigated by the high altitude and low water vapor of the SO site, it is nevertheless difficult to control this contamination due to the spatial and temporal fluctuations in the atmosphere caused by local weather conditions. The atmospheric noise enters the detector time ordered data (TOD) as $1/f$ noise, reducing sensitivity at large angular scales [36, 44, 47, 125].

Experiments without rapid polarization usually mitigate the atmospheric $1/f$ noise and reconstruct the linear polarization by differencing detectors with orthogonal antennas [183, 182, 17]. However, any mismatched response between orthogonal detectors leads to intensity to polarization (I2P) leakage, which contaminates the cosmological polarization signal [172]. In addition, the statistical uncertainty is expected to improve as the number of detectors increases. Thus, the control of systematic uncertainties and $1/f$ noise increases in importance.

In order to mitigate both $1/f$ noise and I2P, the SATs employ a CHWP-based polarization modulation system, which is a commonly used technique among millimeter and sub-millimeter polarimeters. The HWP consists of a birefringent material that introduces a phase difference of 180° between the ordinary and extraordinary axes. Therefore, after passing through the HWP, the linear polarization angle changes according to the angle between the incident polarization angle and the HWP extraordinary axis. If the

HWP is continuously rotating, the measured linear polarization signal rotates synchronously with the rotation of HWP. Thus, the incident light can be modulated above $1/f$ noise fluctuations by setting the appropriate rotation frequency. The HWP modulated signal incident on a polarimeter sensitive to a single linear polarization is expressed as

$$d_m(t) = I(t) + \epsilon \mathrm{Re}[(Q(t) + iU(t))\, m(\chi)], \tag{3.1}$$

where t is time, I, Q, and U are Stokes vectors of the incident light, assuming $V = 0$. ϵ is the HWP polarization modulation efficiency, χ is the rotation angle of the HWP, and

$$m(\chi) = \exp(-i4\chi) \tag{3.2}$$

is the modulation function. To extract the intensity signal, we low-pass filter the modulated data. To extract the linear polarization signals, Q and U, we band-pass filter the modulated data around the modulation frequency and multiply by the complex conjugate of $m(\chi)$ and low-pass filter it. We call this procedure demodulation [99]. There is no need for differencing pairs of orthogonal detectors in demodulation. The CHWP employs a Pancharatnam-style [137] achromatic HWP (AHWP) composed of three single-crystal sapphire plates. Sapphire was chosen because it has high thermal conductivity and low millimeter-wave absorption. The AHWP is a common solution to cover wide frequency bands, and it has been employed in several CMB experiments [188, 79, 122, 28, 68] and will be employed in planned experiments [164]. The design of the AHWP is similar to that used in the Simons Array experiment, including the 3 slabs of sapphire with anti-reflection (AR) coating [69]. The control of systematic effects from the AHWP is a crucial aspect of the HWP polarimetry [122, 48, 123]. The study of detailed performance and systematics of SO AHWP will be reported elsewhere. The design of the rotation mechanism inherits many aspects of the analogous system in the Simons Array experiment [68]. However the details of the implementation have been modified to adapt to the unique requirements of the SO SAT receiver as shown in Fig. 3.1.

The driving philosophy behind the CHWP system design is ensuring stability, both mechanically and thermally. Since the CHWP is located in the SAT's main beam [114] (Fig. 3.1), any unpredictable behavior carries a risk of contaminating the polarization signal from the sky. As such, we require any variation in the CHWP system other than its fast modulation to be small, slowly varying, and measurable where possible. Furthermore, we look for robust design solutions that will withstand years of continuous operation at the Simons Observatory site while minimizing maintenance and telescope downtime. Finally, we develop the CHWP rotation mechanism as a modular system that can be tested with more frequent iterations before being integrated with the complete SAT cryostat.

Sec. 3.2 presents the CHWP requirements for SO SAT, Sec. 3.3 presents the design of subsystems, Sec. 3.4 presents the results of laboratory performance, and Sec. 3.5 summarizes the development and describes future prospects.

3.2 Requirement

Table 3.1 summarizes the requirements of the CHWP and their achieved values. Our CHWP system for SO SATs relies on the heritage of the CHWP for the Simons Array telescopes [68], and the requirements qualitatively remain the same. Notable differences include a) a larger optical throughput requiring

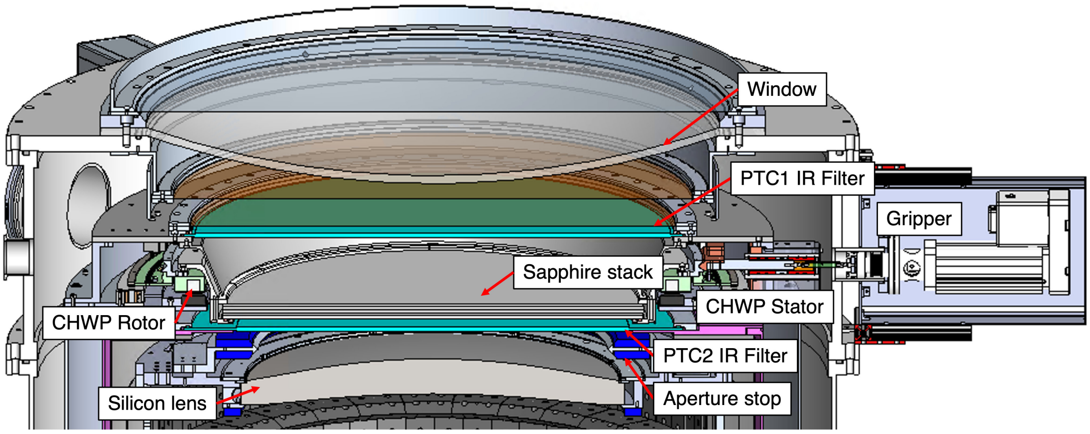

Fig. 3.1 The computer-aided design (CAD) cross-section of the small-aperture telescope's receiver.

Table 3.1 The CHWP's numerical requirements and achieved values.

Parameter	Requirement	Achieved
Assembly outer diameter	$\leq$ 950 mm	931 mm
Assembly height	$\leq$ 246 mm	124.5 mm
Cryogenic stage mass	$\leq$ 70 kg	66 kg
Clear aperture diameter	$\geq$ 478 mm	478 mm
Rotor radial alignment	$\leq$ 5 mm	$\leq$ 4.5 mm
Rotor temperature T_{rotor}	$\leq$ 85 K	$\leq$ 70 K
Stator temperature T_{stator}	$\leq$ 70 K	$\leq$ 60 K
Rotor thermalization time[1]	$\leq$ 36 hr	10 hr
Rotation frequency f_{HWP}	$\geq$ 2 Hz	$\leq$ 0.5 Hz-3 Hz
Rotation stability Δf_{HWP}[2]	$\leq$ 10 mHz	$\leq$ 5 mHz
Angle encoder noise σ_χ	$\ll 3\ \mu\mathrm{rad}/\sqrt{\mathrm{Hz}}$	$0.07\ \mu\mathrm{rad}/\sqrt{\mathrm{Hz}}$

[1] lag time of rotor vs stator on initial cooldown.
[2] The requirement is over the observation period of several years. The achieved stability is over 4 days (Fig. 3.10).

optical diameter of 490 mm and the placement of the HWP optics close to the telescope's aperture stop; b) relaxed requirements on the physical volume available to the system; and c) a larger variation of the gravity vector due to the addition of bore sight rotation about the SAT's optical axis to the scan strategy resulting in the rotor alignment requirement.

3.2.1 Operational

During normal operation we require steady rotation frequency of CHWP (f_{HWP}) faster than 2 Hz in order for the polarization signal from the sky to be modulated faster than the $1/f$ knee of temperature fluctuations in the atmosphere [99, 186]. In order to make efficient use of observing time, we require spin-up (down) to (from) this rotation frequency to be achieved in less than 5 minutes. We also require the peak-to-peak stability of f_{HWP} to be smaller than 10 mHz during observations over a observation period of several years.

3.2.2 Mechanical

For ease of installation, the CHWP rotation mechanism is designed to easily accommodate the front end, window-side, of the cryostat. This constrains the total envelope of the cryogenic components to be < 950 mm in diameter and < 246 mm in height along the optical axis. The total mass requirement of the CHWP, ≤ 70 kg, is not tightly constrained, as it is subdominant to the total suspended mass of the cryogenic stages supported by the primary cryo-mechanical truss [39]. CHWP rotation can generate vibrations in the cryostat, and heat up the focal plane's temperature, degrading detector gain stability and introducing $1/f$ noise. We require no measurable CHWP-induced resonant heating in the focal plane temperature.

3.2.3 Optical and Spatial

A clear aperture is among the central requirements to the CHWP system. We are especially careful to prevent against any optical interference from moving parts of the rotation mechanism, as any signal modulated at $4f_{\mathrm{HWP}}$ mimics incident polarization. To this end, we require that all rotating parts other than the optical stack outside the -20 dB margin of the 90 GHz beam. To this end, we require all rotating parts other than the sapphire stack to be outside of the -20 dB margin of the 90 GHz beam, and to be circularly symmetric. The 90 GHz band is chosen because it gives the most stringent optical requirements between the MF and UHF bands.

Given the SAT's 35° field of view and the diffraction limited beam, these requirements impose a keepout zone with an opening angle of 45° extending skyward from the 420-mm diameter aperture stop. The sapphire stack must be at least 490 mm in diameter at a distance of 40 mm away from the aperture stop; as close to the stop as possible while maintaining sufficient mechanical margin for the PTC2 alumina filter in between. Static (non-rotating) components are designed to be smaller than the smallest rotating dimension with the margin of -15 dB maximum. We also require that the innermost static components be circularly symmetric.

Finally, the misalignment of the rotor with the optical center must not exceed 5 mm during operation, because any large misalignment would lead to physical interference or contamination of the beam.

3.2.4 Thermal

The rotor temperature is required to be below 85 K to reduce thermal emission, requiring the thermal loading by the CHWP induced IR radiation incident on the PTC2 alumina filter to be subdominant to the total thermal loading on the PTC2 stage [58]. The sensitivity loss due to mm-wave emission from CHWP is expected to be small when the rotor temperature is below 100 K [68]. The stator temperature is required to be well below the critical temperature of the superconducting bearing (Secs. 3.3.2 and 3.4.5). The power dissipation on PTC1 stage is required to be subdominant to the total thermal loading on the PTC1 stage, and also care is taken to effectively heat sink the CHWP stator to the PTC1 stage to reduce temperature gradients generated by the loading from the CHWP system during operation, and also to improve efficiency of the motor drive system by reducing the resistance of the motor drive coils. A lower temperature of the HWP optics reduces the fluctuation and non-uniformity of its emissivity and also helps to reduce the potential systematics in the observed polarization signal. The lower power dissipation is an advantage not only for the cryogenic components, but also for the room-temperature components, especially for the experiments conducted at the altitude of 5,200 m, where convective air cooling is poor.

3.2.5 Data Acquisition

Precise measurement of the rotation angle of HWP is crucial for demodulation in the data analysis. We require that the propagated noise equivalent temperature (NET) of the angular encoder be an order of magnitude smaller than the MF SAT NET goal: 1.4 μK $\sqrt{\text{s}}$ [6], where we combine the sensitivity at 93 and 145 GHz to be conservative. Assuming a ~ 100 mK constant polarization induced by the vacuum window and the PTC1 alumina filter [166], and following a similar calculation to that described in Hill et al. [68], this imposes a limit of 3 μrad $\sqrt{\text{s}}$ for the encoder white noise level. In addition to the low encoding noise, robustness in encoding, such as a low rate of data packet loss and of glitches, is crucial [153].

Due to the remote nature of the SO site, we also require that the CHWP system be capable of autonomous operation, including the capability of its diagnostic monitoring system to detect a power interruption to the cryostat and trigger an automatic shutdown procedure, braking and re-gripping of the rotor.

3.3 Design

In this section we describe the mechanical design of the rotation mechanism and highlight the novel aspects.The overall mechanism can be divided into five major components: the HWP, the superconducting magnetic bearing (SMB), the grippers, the motor, and the angle encoder.

As shown in Figs. 3.1 and 3.2, the non-rotating cryogenic components of the CHWP mechanism are built onto a 884 mm diameter baseplate which mounts to the sky-facing flange of the PTC1 stage (nominally held at 45 K) [1]. The main components mounted onto the baseplate are the superconductor ring, the motor system, and the encoder readheads. Additionally an aluminum shell on the outer diameter of the CHWP assembly both provides a mounting flange for skyward optical components (i.e. the PTC1 stage IR blocking filters and related heat strapping) and also creates a cold, well-regulated radiative cavity to help control the rotor temperature.

3.3.1 Sapphire Stack Mounting

The CHWP system employs an AHWP with a three-layer-sapphire stack sandwitched AR layers. Hereafter, we call this optical element as the sapphire stack. It has a ~505 mm diameter, and the total thickness of all five layers is ~20 mm for the MF band. As shown in Fig. 3.3, the sapphire stack is held in an aluminum cradle. In the vertical direction, the sapphire stack is held along its circumference between a Spira[2] gasket (LS-08) and a series of nylon pads. Nylon is chosen for its low wear and friction at cryogenic temperatures [199]. In the radial direction, the sapphire stack is pressed by a 20° arc-shaped Spira gasket (SS-16). On the opposite side, it is held by two nylon stops, each placed at 120° from the gasket. The radial position is designed to be centered after cooldown, taking into account the contractions and the gasket spring constant.

[1] Cryomech PT-420s , https://www.cryomech.com/products/pt420/
[2] Spira Manufacturing Corp., https://www.spira-emi.com/

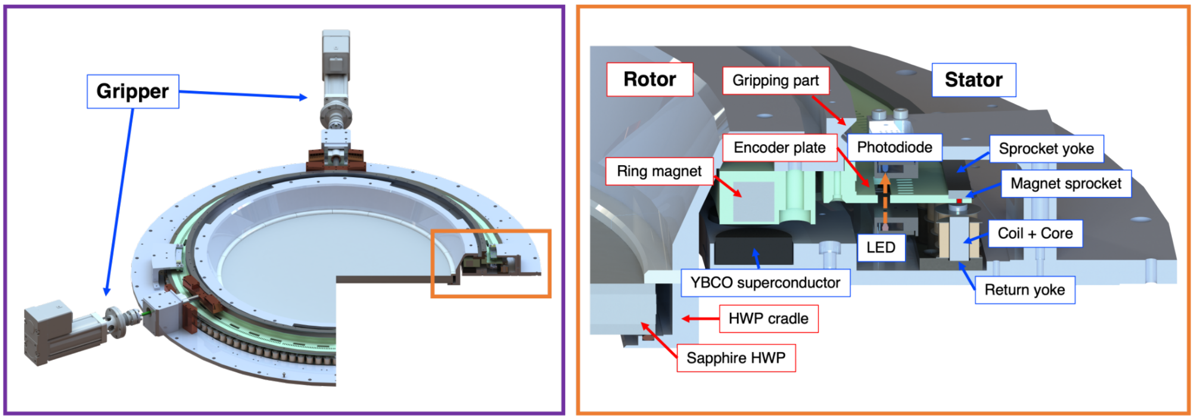

Fig. 3.2 Left panel: the CAD views of SO CHWP system. Right panel: the magnified cross-sectional view of the rotation mechanism. Rotating components are labeled in red, and stationary components are labeled in blue.

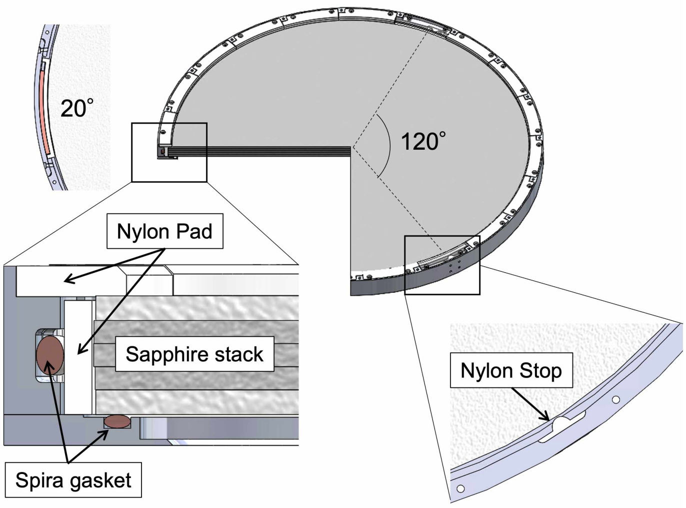

Fig. 3.3 The CAD image of the sapphire stack held in an aluminum cradle. The sapphire stack is held in place vertically by Spira gaskets and nylon pads, and radially by Spira gaskets and nylon stops.

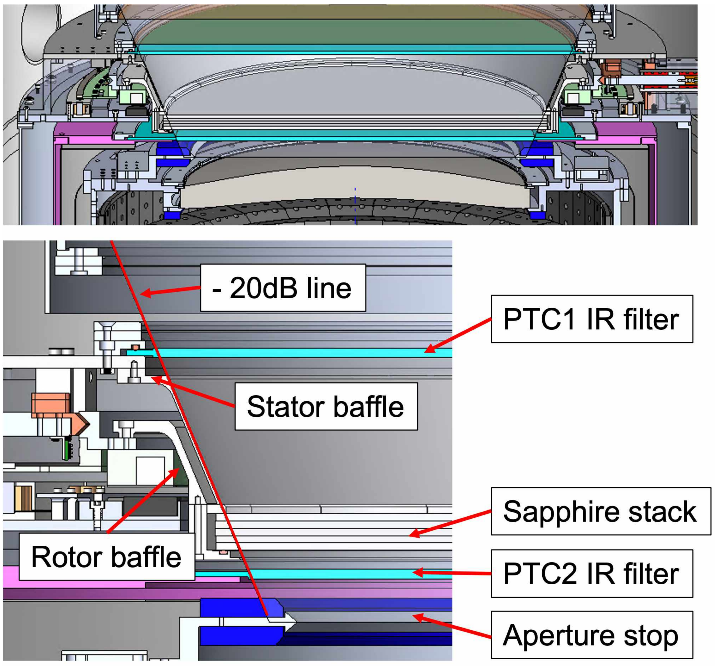

Fig. 3.4 The cross-sectional view of the sapphire stack design with the −20 dB line of the 90 GHz beam.

The cradle is mounted on the rotor baffle, which is shielded from the beam by the stator baffle (Fig. 3.4). As discussed in Sec. 3.2.3, any moving parts, e.g. the cradle aperture and rotor baffle, are designed to intercept the diffracted beam at the −20 dB level or below for 90 GHz when the rotor is at its nominal position. The stator baffle intercepts the diffracted beam at the −18.5 dB level at 90 GHz.

3.3.2 Superconducting Magnetic Bearing

The CHWP employs a 550 mm diameter superconducting magnetic bearing [163]. While SMBs have been demonstrated in other CHWP systems for CMB observations [115, 90, 80, 165, 162, 68], the SO SMB is the largest of its kind developed to date. The SMB is composed of a permanent ring magnet on the rotor and a ring of 61 or 53 disks of yttrium barium copper oxide[3] (YBCO) epoxied into an aluminum holder on the stator. YBCO is a type II superconductor with transition temperature of ~ 90 K, below which the magnetic flux of the rotor is pinned in flux vortices in the disks, resulting in the loss of all but the rotational degree of freedom. The ring magnet of 550 mm inner diameter was manufactured by Shin-Etsu Chemical[4] and consists of 32 segments of neodymium (NdFeB; N52) fixed in a G10 enclosure. Care was taken in assembly to minimize gaps between the segments in order to maintain an azimuthally symmetric field. The friction and stability of this bearing was previously characterized in Sakurai et al. [163] The optimization of the SMB design and its vibration performance are discussed in Sec. 3.4.4.

[3]Can Superconductors, CSYL-28 https://www.can-superconductors.com/
[4]Shin-Etsu Chemical Co., Ltd., https://www.shinetsu.co.jp/en/

3.3.3 Grippers

While the YBCO disks are above their transition temperature (~ 90 K), the rotor is not suspended by the flux-pinning effect and it is necessary to firmly grip it. This is accomplished by a grip-and-release mechanism, referred to hereafter as grippers. The grippers are a set of three linear actuators [5] with vacuum adapters manufactured by Huntington.[6] The actuator shafts mate to wedged tips mounted on the stator which engage with a matching groove on the rotor when extended. This system allows for the precise and repeatable positioning of the rotor with respect to the rigid body of the SAT. The gripper design closely follows the design described in Hill et al. [68], with minor modifications. A single gripper can provide a pushing force that is more than twice the weight of the rotor; this is necessary to enable re-gripping and centering at any telescope elevation, as required in Sec. 3.2.3.

3.3.4 Motor cryogenic assembly

The motor system that provides torque to the rotor is similar to that described in Hill et al. [68], with an increased number of coils due to the larger diameter of the SAT. The magnetic field from the motor coils couples to the magnet sprockets on the edge of the encoder plate (Fig. 3.2), driving rotation. We employ optical encoders, a set of five IR light emitting diodes[7] (LEDs) mounted on an arm that hangs over a G10 encoder plate mounted to the rotor (Fig. 3.2). The LEDs are aligned with a matching set of photo-diodes[8] located below the plate. The encoder plate is slotted at two different radii in order to chop the light emitted by the LEDs. The photo current signal chopped by the wider slots drive the motor coils by providing feedback through the motor drive electronics (Sec. 3.3.5), while the signal chopped by the finer slots is fed to the encoder electronics for calculation of the rotation angle of the CHWP (Sec. 3.3.6). Two encoder heads are installed at 180° from one another for redundant angle encoding. Data from both encoder heads can be combined to estimate the rotor's off-center displacement, as described in Appendix. A.2.

3.3.5 Motor Driver

The details the motor drive electronics, driver board, closely follow the method used in Hill et al. [68] Here we highlight the two design improvements. First, a Proportional-Integral-Differential (PID) feedback system is used further regulate the rotation frequency. For this system, a frequency-to-voltage circuit serves as an input to a PID controller[9] which adjusts the drive voltage and modulates the motor torque. With the PID enabled the frequency control system becomes closed loop and is able to account for unexpected changes to motor efficiency. PID parameters are chosen to minimize long-timescale variations.

Second, a phase compensation circuit is used to further improve rotation stability. While the CHWP rotates, the inductance of the motor coils distorts the motor drive feedback signal. This distortion increases with the rotation frequency and acts as an effective phase delay to the motor drive signal. The phase compensation circuit accounts for this effective phase delay and improves overall motor efficiency. We implement a discrete phase compensation in 60° increments through the sign reversal

[5] SMC Corporation. LEY32C-30B-S11P1
[6] Huntington Vacuum Products. https://huntvac.com/
[7] Vishay, VSMB294008G, https://www.vishay.com/docs/84228/vsmb294008rg.pdf
[8] Vishay, TEMD1020, https://www.vishay.com/docs/81564/temd1000.pdf
[9] Omega, CNI16D54-EIT, https://www.jp.omega.com/pptst/CNI_SERIES.html

and the phase swapping of the three-phase motor using relay modules. The use of the relay modules eliminates single-point failures and minimizes noise added to the motor coil drive feedback. Phase compensation with 60° increments is not always optimal, but is easily achieved and provides sufficient control and efficiency. The performance of the rotation drive control electronics and the evaluation of rotation efficiency are summarized in Secs. 3.4.2 and 3.4.3, respectively.

3.3.6 Data acquisition

Data generated by the CHWP's cryogenic system is routed from the cryostat via four cables to a warm electronics box for processing. Acquisition of the rotor angular time stream requires cleaning and digitizing the raw encoder signals sent from the CHWP. This processing follows the method described in Hill et al. [68].

The CHWP system also continuously records information from the motor driver, a Hall probe, and four silicon diode cryogenic thermometers. The diodes are placed on the YBCO superconductor ring, sapphire stack mount on rotor, PTC1 filter plate and PTC2 filter plate, and are continuously monitored by a Lake Shore Model 240.[10] Rotor temperature measurement is achieved through electrical contacts attached to the end of each gripper. Therefore, measurement is only possible while the rotor is held by the grippers, but can be used to determine when it is safe to release the grippers and begin CHWP operation. A Hall probe[11] attached to the YBCO assembly continuously measures the magnetic field intensity around the superconductor (Fig. A.2). The neodymium magnet in the rotor assembly is the primary magnetic source, and its field varies with changes in rotor temperature and displacement, enabling the Hall probe to monitor both of these properties [165]. The monitoring and control of the CHWP system are managed by the Observatory Control System [95].

3.4 Performance

We discuss the thermal and mechanical performance of three CHWPs evaluated in the CHWP test cryostat at the University of Tokyo or in the SAT cryostats at the University of California San Diego (UCSD), Princeton University, and the Lawrence Berkeley National Laboratory (LBNL) (Fig. 3.5).

3.4.1 Thermal

Figure 3.6 shows the rotor and stator temperatures during a cooldown. Initially, the rotor is held by the grippers and is primarily cooled by conduction through the grippers' copper fingers. The rotor temperature lags behind the stator by 10 hours, well within the 36 hour requirement.

Once the YBCO disks become superconducting and the rotor temperature stabilizes, the rotor is ungripped and begins to levitate. Figure 3.7 shows the rotor temperature as a function of time, while it is floating (blue points) and when it spins at 2 Hz (red points) after temperature stabilization. In order to collect temperature data with the rotor spinning, its rotation is intermittently stopped and its temperature is measured using the gripper touch probes (Sec. 3.3.6). This process is performed once every few hours with the duration of each touch not exceeding 60 seconds, leading to little disturbance

[10] Lake Shore, Model 240, https://www.lakeshore.com/products/categories/overview/temperature-products/cryogenic-temperature-modules/240-series-input-modules

[11] Lake Shore, HGT-3010 https://shop.lakeshore.com/default/transverse-hall-sensor-3010hgt-3010.html

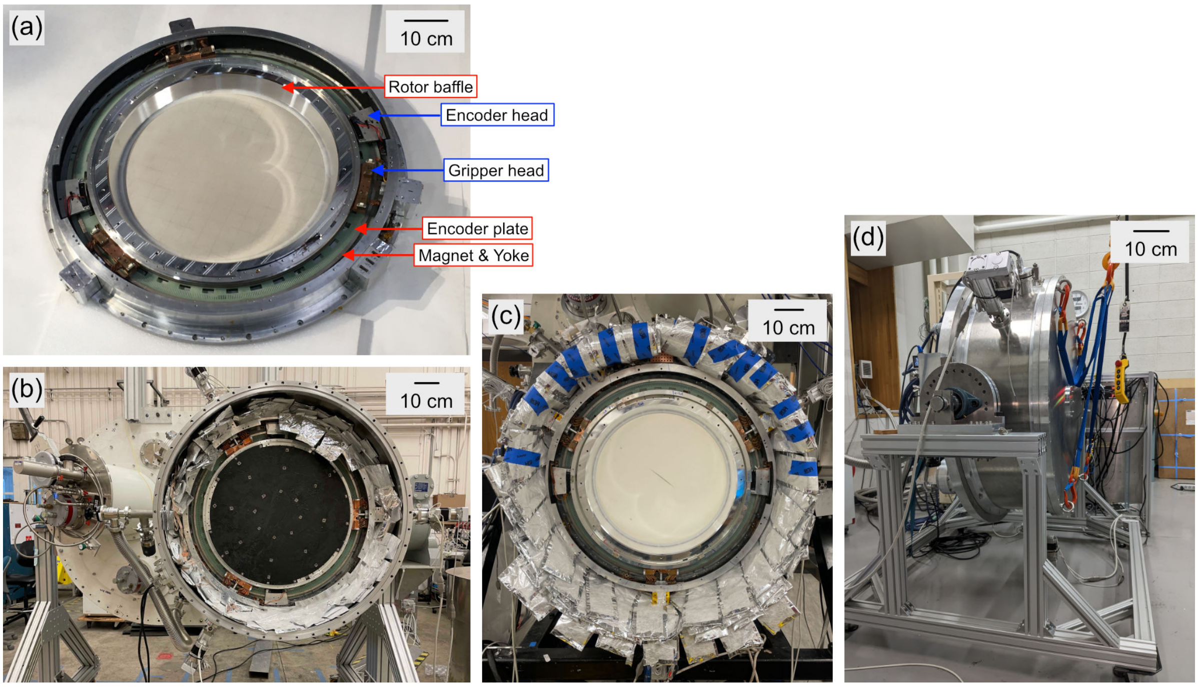

Fig. 3.5 The CHWP rotation mechanisms during testing. Panel (a) shows the rotation mechanism with the sapphire stack for the SAT cryostat at UCSD. Panels (b) and (c) show the rotation mechanisms installed in SAT cryostat at LBNL and Princeton University respectively. In panel (b), the black object mounted in the rotor is a dummy mass, used to realistically validate the mechanical and thermal performance. Panel (d) shows the CWHP test cryostat at the University of Tokyo.

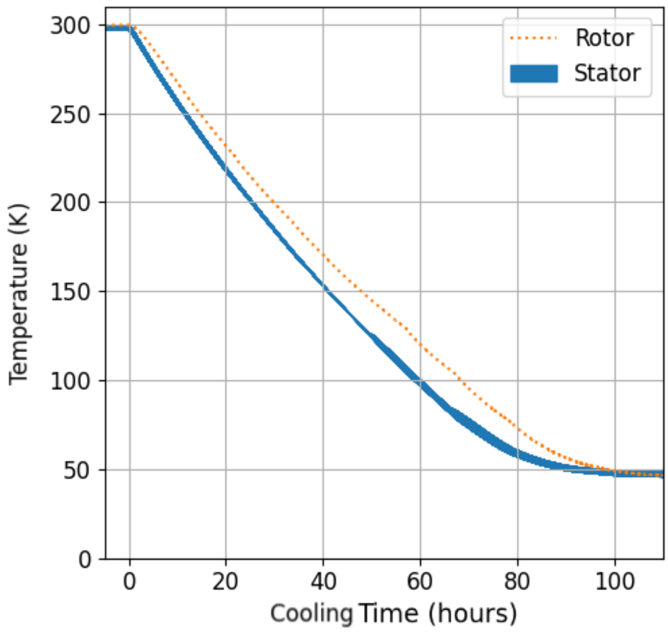

Fig. 3.6 Rotor and stator temperatures during the cooldown. The rotor thermalizes within 10 hours of the stator.

in the rotor's temperature trend. The blue points inform us of optical loading where the IR loading is dominant, while the red points provide estimates of the excess loading generated by rotation. Each set of points are fit by

$$T(t) = T_e + \Delta T \exp(-t/\tau), \tag{3.3}$$

where T_e represents the estimated rotor temperature at steady state, τ is the time constant, and ΔT is the difference between the initial and steady state temperature. The steady state temperature of the CHWP rotating at 2 Hz is 70 K, which satisfies the requirement of ≤ 85 K. The time constants of the blue and red curves are 31 hours and 46 hours, respectively. As shown in the bottom panel of Fig. 3.7, there is no significant change in the temperature of the PTC2 IR filter indicating that the PTC2 stage has sufficient cooling capacity over the estimated thermal loading by the IR radiation from CHWP of 120 mW.

Figure 3.8 shows the model for an ANSYS thermal simulation, which is used to further characterize the CHWP thermal cavity as well as the heat input to the rotor. For the simulation we simply model the floating rotor surrounded by the PTC1 aluminum shell and the PTC1 and PTC2 alumina IR filters. Based on our measurements, we set the temperatures of aluminum shell and alumina filters in the simulation to 55 K, 60 K and 4 K, respectively. The infrared emissivity of the alumina IR filter is set to 0.8 [76], while that of the aluminum shell is set to 0.96. Here the inside of the aluminum shell is covered with an infrared black body [145]. Since there is no physical contact, the rotor exchanges heat with other components only by thermal radiation. Figure 3.7 shows the simulated time series of the rotor temperature with a constant heat input to the floating rotor. By comparing the data with the simulation result, the heat input to the rotor is estimated to be 220 mW when the rotor is floating, and 390 mW when the rotor is rotating at 2 Hz.

3.4.2 Rotation control

Figure 3.9 shows the performance of the PID control and the phase compensation described in Sec. 3.3.4. When the rotation PID feedback is on, the rotor accelerates to a steady rotation at 2 Hz within 7 minutes, and decelerates down to 0 Hz within 3 minutes. When phase compensation is used in conjunction with the PID, the spin-up time to steady rotation at 2 Hz is reduced to less than 4 minutes. Figure 3.10 demonstrates the stable rotation of CHWP at 2 Hz over 4 days using PID control. The achieved stability of rotation frequency ± 3 mHz is well within the requirement, ± 10 mHz. Although not tested in-lab, the stability of the PID control loop over even longer timescales is expected to remain below the requirement. We additionally performed an in-lab azimuth scan to demonstrate stable operation of the CHWP in observation-like conditions. The receiver was held at a constant elevation angle of 50° and subject to an angular throw of 12°, constant scan velocity of 1°/sec, and turnaround acceleration of 1°/sec^2. While the nominal SAT angular throw will be wider, more frequent turnarounds during this test enabled an evaluation of scanning effects on PID performance under more strenuous operating conditions.

Figure 3.11 shows a time stream of the measured rotation frequency during scanning where we observe a scan-synchronous modulation of the measured frequency (±2 mHz). This is because the encoders and SAT detectors are fixed in the telescope reference frame, but the magnetically levitated CHWP is not. Thus the measured modulation arises from conservation of angular momentum of the CHWP about its rotation axis. The angular velocity of the CHWP during scanning is given by the following, the detailed derivation of which is described in Appendix A.1:

$$\dot{\chi}(t) = \bar{\dot{\chi}} - \dot{\phi}(t)\sin(\theta_{\mathrm{el}}), \tag{3.4}$$

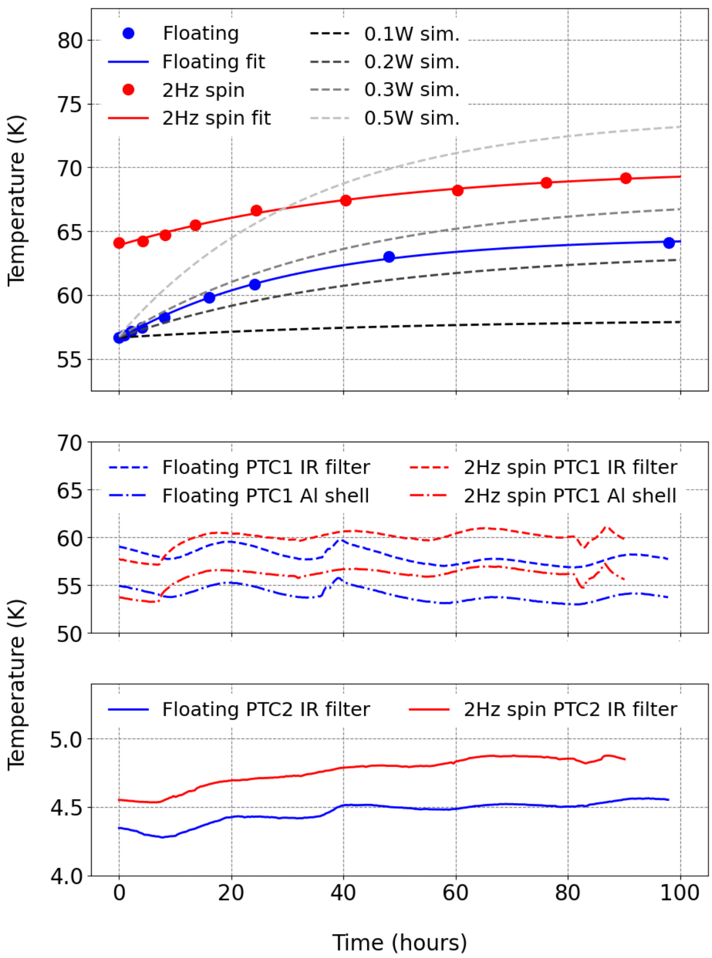

Fig. 3.7 Top panel: The rotor temperature profile while it is floating (blue points) and spinning at 2 Hz (red points), which are fit by Eq. 3.3 (solid lines). Black dashed lines show the ANSYS thermal simulation results with heat inputs of 0.1, 0.2, 0.3 and 0.5 W, respectively. The initial temperature of the simulation was set to the initial temperature of rotor when released from the grippers. The heat dissipation to the rotor is estimated by comparing the thermal equilibrium temperature between the fit result and the simulation. Middle panel: Colored dashed lines represent temperatures of the alumina IR filter and aluminum shell. Bottom panel: PTC2 IR filter temperature profile while the rotor is floating (blue) and spinning at 2 Hz (red).

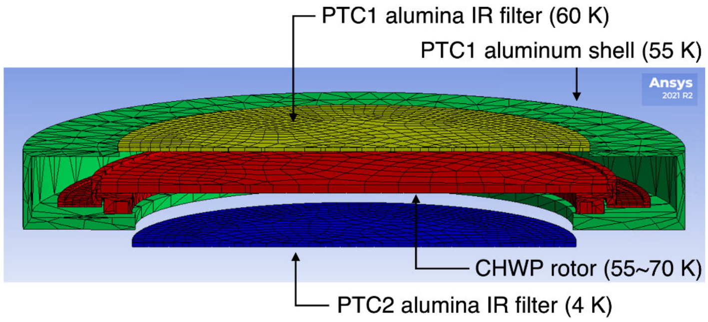

Fig. 3.8 The ANSYS thermal model used to simulate the amount of thermal loading from the CHWP rotor to the PTC2 stage. Temperatures of the PTC1 aluminum shell, the PTC1 and PTC2 alumina IR filters are set at 55 K, 60 K and 4 K respectively. The rotor temperature is varied from 55 K to 70 K to estimate the thermal loading on the PTC2 alumina IR filter. Image used courtesy of ANSYS, Inc.

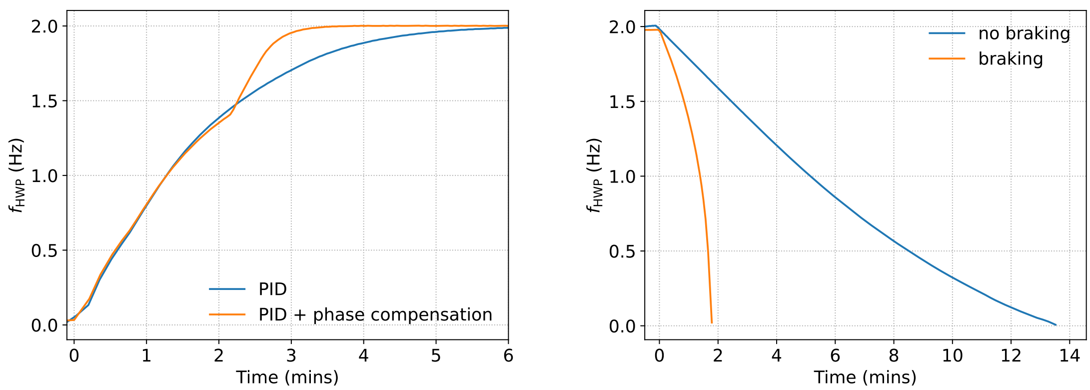

Fig. 3.9 Left: The spin up curves. The blue curve shows the spin up curve with PID control. The rotation speed stabilizes in ~ 7 minutes. The orange curve shows the spin up curve with phase compensation activated at 2.2 minutes. With the phase compensation, the rotation speed stabilizes in ~ 4 minutes. Right: The spin down curves. The blue curve shows the spin-down curve of HWP without braking. Braking can stop HWP in less than 3 minutes (orage curve).

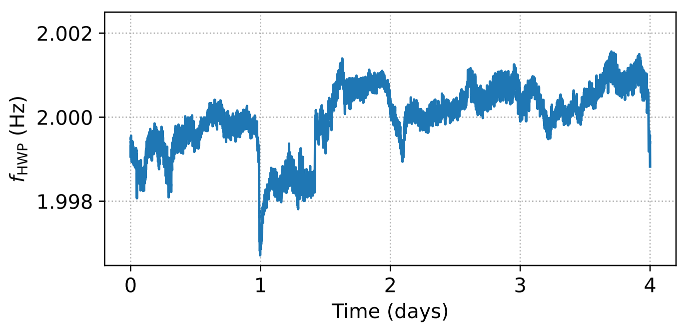

Fig. 3.10 Demonstration of stable rotation of CHWP at 2 Hz over 4 days using PID control

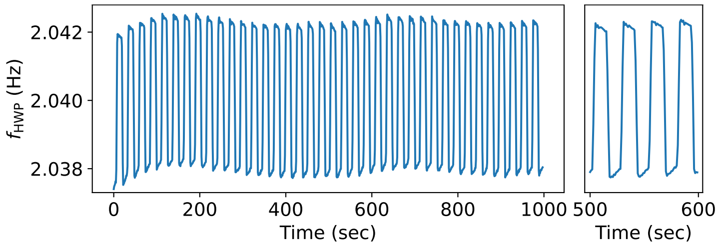

Fig. 3.11 Time stream of the measured HWP rotation frequency during the constant elevation scan of the SAT receiver at an elevation of 50°. The long timescale PID rotation control is enabled.

where ϕ is the azimuth angle of the telescope, θ_{el} is the elevation angle of the telescope and $\bar{\chi}$ is the average angular velocity of the CHWP. The PID is tuned for longer-timescale stability and reacts little to the azimuthal scan modulation. This demonstrates that the accuracy of the encoding system and the stability of rotation frequency are well within the requirement including the effect of scan modulation.

3.4.3 Rotation efficiency

Table 3.2 summarizes the thermal dissipation of the rotation mechanism to the stator and PTC1 stage. There are four primary sources of thermal dissipation from the CHWP: a) Joule heating of the driving coils, where the phase compensation of the motor driver (Sec. 3.3.4) plays an important role, b) hysteresis loss in the SMB, c) eddy current loss in the SMB, and d) dissipation from the optical encoders. a) is characterized by the impedance and the bias voltage of the motor coils, while b) and c) are characterized by fitting the spin-down curve, using the method described in Sakurai et al. [163] As noted in Table 3.2, b) and c) are dependent on the elevation angle, or the gravity vector direction. Lower elevation angles lead to a larger distance between the YBCO and the magnet ring of the rotor along the optical axis, resulting in a weaker and smoother magnetic field coupled to the YBCO, thus diminishing the loss from hysteresis and eddy currents. The total dissipation from the motor and SMB (a+b+c) is measured by comparing the loading on the PTC1 stage when the CHWP is operating and when it is not. The power dissipation of the optical encoders is mainly from the LEDs, which is estimated to be smaller than 1 W based on the bias current and voltage.

a) is reduced by optimizing the phase compensation angle of the drive motor (Sec. 3.3.4). The phase compensation angle was optimized using the power consumption of the motor driving current source,[12] which includes dissipation both inside and outside of the receiver. Figure 3.12 shows the power consumed by the current source as a function of the phase compensation angle of the drive motor. The power consumption with a 2-Hz rotation achieves minimum at 60°.

With a motor drive phase compensation of 60°, the power consumption is reduced from 3.6±1.0 W to 0.8±0.1 W, and the dissipation of the motor on the stator is reduced from 3.1±1.0 W to 0.5±0.1 W. This results in a total power dissipation of ≤ 1.6 W summing motor dissipation with that of the LEDs.

As we discuss in Sec. 3.4.5, the off-center displacement of the rotor induces a phase shift between the two encoders. Because the motor drive current source uses feedback from the encoder to its output (Sec. 3.3.5), the rotation efficiency is also dependent on this phase shift and the rotation direction. As we see from Fig. 3.12, the rotation efficiency is sensitive to the phase shift of the motor when phase compensation is not activated, but is insensitive when 60° of phase compensation is activated. Therefore,

[12] Kikusui electronics corp. PMX35-3A

Table 3.2 Dissipation of rotation mechanism on stator, PTC1 stage.

Motor	Joule heat of driving coils	0.4±0.1 W (2.6±1.0 W)[1]
SMB	Hysteresis loss of SMB	0.083 W/ 0.084 W[2]
	Eddy current loss of SMB	0.058 W/ 0.099 W[2]
	Total	0.5±0.1 W (3.1±1.0 W)[1]
Encoder	Power dissipated by LEDs	≤ 1 W[3]

[1] Dissipation when phase compensation is activated (not activated).
[2] Dissipation at an elevation of 50° / 90°.
[3] 10 LEDs are biased with 50 mA and 2 V.

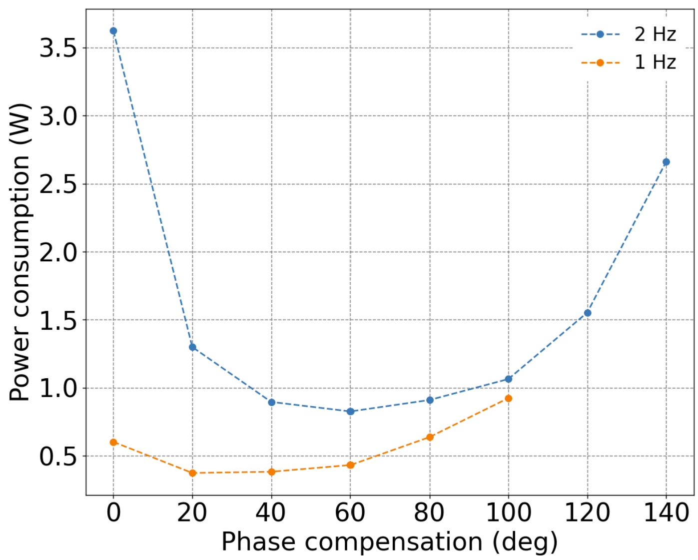

Fig. 3.12 The power consumption of the current source of three-phase motor as a function of phase compensation angle. A digital phase compensation circuit implemented by a microcontroller is used to apply an arbitrary amount of compensation and determine the optimal value.

the phase compensation enables to achieve robust rotational efficiency regardless of changes to the off-center displacement and rotation direction.

3.4.4 Vibration

The characteristic vibration frequencies of the SMB are key parameters for the vibrational performance of the CHWP. From the mass of the rotor and the displacement we evaluate in Sec. 3.4.5, the spring constants of the SMB parallel and perpendicular to the optical axis are estimated to be 5.2(8.4)$\times 10^5$ N/m and 9.1(17)$\times 10^4$ N/m respectively for 48(61) YBCO tiles. From these values, we determine the corresponding characteristic vibrational frequencies to be 7(9) Hz and 9(13) Hz respectively, which are in agreement with the results of Sakurai et al. [163]

The primary instrumental parameter that impacts the vibrational performance is the number of YBCO disks of the SMB. Throughout our evaluation of the SAT's susceptibility to CHWP induced vibrations, our design of the SMB evolved from 48 disks to 53 or 61. This section presents their comparison. We employ two methods to characterize vibration, one by using a three-axis accelerometer[13] mounted on the cryostat near the rotation mechanism, and the other by measuring the temperature increase of the 100-mK focal plane stage while sweeping through CHWP rotation frequencies.

Figure 3.13 shows the spectrogram of the vibration parallel to the optical axis. We do not observe significant vibration perpendicular to the optical axis. Vibrations were measured at frequencies equal to f_{HWP} multiplied by the number of coils (= 120), or the number of YBCO disks (= 48, 53) multiplied by an integer. In the 48-disk setup, the 96th harmonic of f_{HWP} was the largest vibrational mode. 96 is the least common multiple of the number of YBCO disks (= 48) and the number of NdFeB magnet segments (= 32), and this relationship yielded vibrational coupling that produced higher amplitude vibration. In the 53-disk setup, the number of YBCO disks and NdFeB magnets are relatively prime (do not have common divisors larger than 1) and we did not observe vibrational mode associated with their coupling. The influence of vibration on the focal plane temperature in two representative SMBs with different numbers of YBCO disks is shown in Fig. 3.14. The rotation of CHWP was monotonically swept in frequency from 0.5 to 2.3 Hz over a 12 hour duration while measuring the temperature of the cryogenic stages. Since these two SMBs are tested in SATs with different instrumentation, a direct comparison of the thermal sensor noise is not possible, however the resonant heating response observed in a 48-disk setup is not seen in a 53-disk setup.

3.4.5 Rotor alignment and displacement

There are two degrees of freedom that we consider important for the alignment of the CHWP rotation mechanism: alignment along the optical axis, involving displacement perpendicular to the plane of the SMB, and center alignment, involving displacement along the SMB plane. In this section we discuss alignment performance along these degrees of freedom, in addition to the effect of temperature on alignment. The quality of the rotor alignment is determined both by the initial centering established by the grippers and by the stiffness of the SMB.

Because the magnetic flux-pinning acts as a restoring force with a finite spring constant, when the rotor is released from the grippers it displaces due to gravity, finding a new equilibrium position that depends on the elevation angle. Due to its azimuthal symmetry, the SMB is most stiff along the optical

[13] Analog Devices, adxl345 https://www.analog.com/en/products/adxl345.html

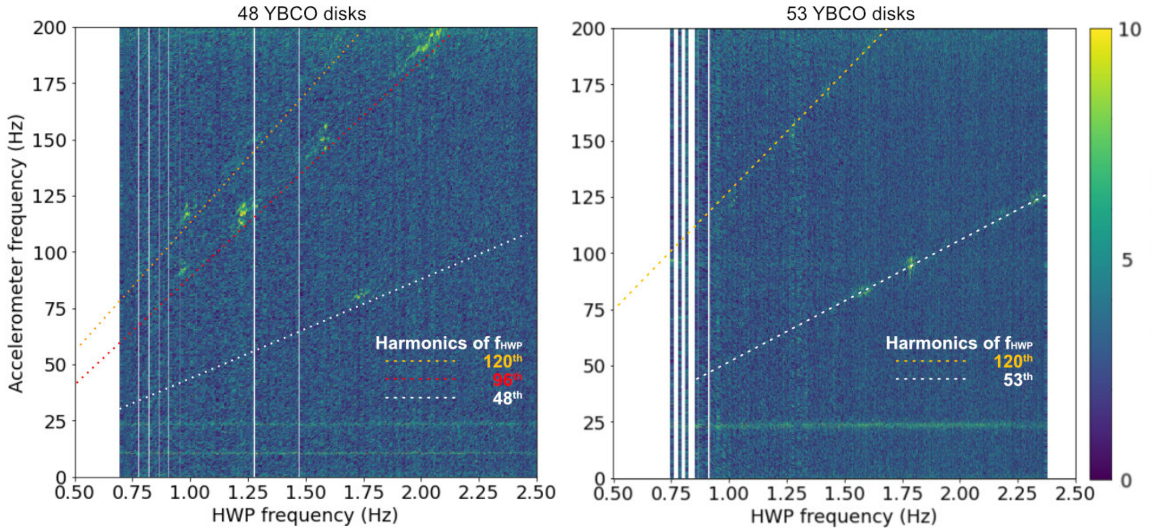

Fig. 3.13 Comparison of the vibration of the SMB with different numbers of YBCO disks. Vibration is observed at f_{HWP} multiplied by an integer times a common multiple of the characteristic numbers of the SMB: the number of ring magnet segments (=32), the number of YBCO disks (=48, 53), or the number of coils (=120). The vibration observed on the 48-disk SMB at f_{HWP} multiplied by the least common multiple of the number of YBCO disks and ring magnets segments (=96) is not observed on the 53-disk SMB.

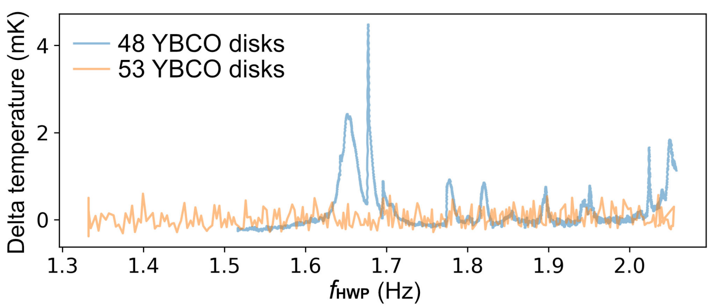

Fig. 3.14 Comparison of the effect of vibration on the focal plane temperature in two SMBs with different number of YBCO disks.

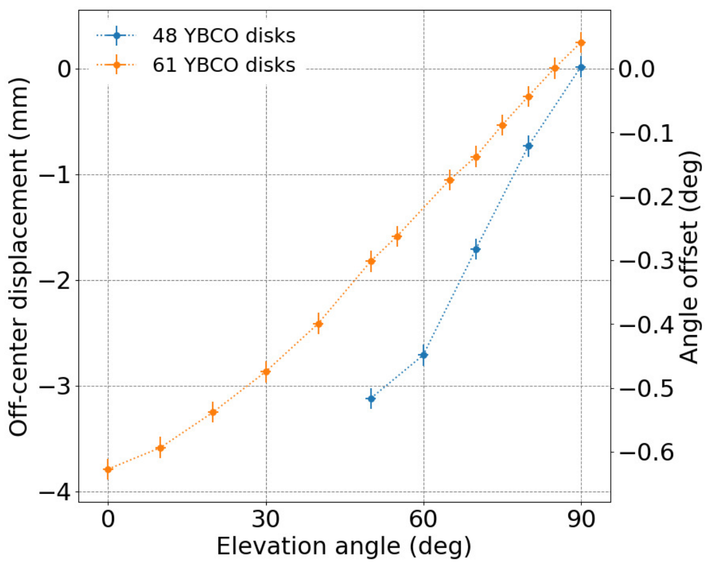

Fig. 3.15 The off-center displacement of the rotor at different elevation angles and different number of YBCO disks. The elevation angle of 90° refers to pointing at zenith (Fig. A.1). The angle offset is an additional measured angle difference between the two encoders due to the off center displacement of the rotor (Eq. A.5).

axis [90]. The off-center displacement produces a phase shift between the two angle encoders, resulting in a difference between the calculated and actual rotational angle and the encoded angle. Therefore, the evaluation of off-center displacement is particularly important.

The stiffness of the SMB is the product of the critical density current of the YBCO, the magnetization of the NdFeB permanent magnet ring, and a constant determined by the geometry of the SMB. A temperature increase from 50 K to 85 K results in ~90% reduction in the critical density current [191] and ~10% reduction in the magnetization [161]. Thus, by measuring the temperature dependence of the rotor displacement we can determine the temperature dependence of the stiffness and obtain the maximum operating temperature of the SMB.

Each of the three primary CHWP alignment considerations can be evaluated independently. Alignment along the optical axis is characterized at 50 K with the methods described in Appendix A.2. The largest displacement occurs at an elevation angle of 90°, resulting in a displacement of 2.0 ± 0.3 mm, which is well within the designed clearance of 5 mm.

Center alignment is evaluated using the method described in Appendix A.2. Figure 3.15 shows the measured off-center displacement at different elevation angles and for SMBs with different numbers of YBCO disks. The off-center displacement was measured seven times at an elevation of 90°, and the initial alignment accuracy was found to be ≤ 1 mm. Inaccurate initial centering by the grippers while cooling through the YBCO transition produces a non-zero displacement at an elevation of 90°. As Fig. 3.15 shows, the off-center displacement decreases as the number of YBCO disks is increased, and is smaller than 3.5 mm with 61 YBCO disks at elevation angles larger than 20°.[14] This satisfies the requirement for optical and mechanical clearance of ≤ 5 mm even when combined with the initial alignment accuracy ≤ 1 mm.

[14]The minimum elevation angle of the SAT platform is 20°.

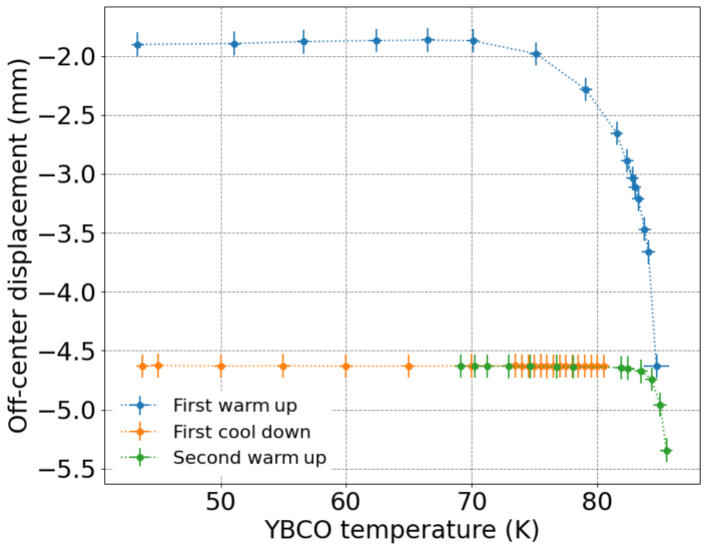

Fig. 3.16 The off-center displacement when the YBCO temperature is increased and decreased to evaluate the maximum operating temperature of the SMB. During the measurements, the rotor is continuously rotating at 2 Hz and the elevation angle is 50 degrees.

Finally, the temperature dependence of the displacement (Fig. 3.16) is evaluated to determine the maximum operating temperature through the following three steps:

1. The temperature of the YBCO is gradually increased to 85 K. The off-center displacement is constant up to 70 K, but rapidly increases after reaching 70 K.
2. The YBCO temperature is gradually lowered from 85 K. The off-center displacement does not change throughout this process.
3. The YBCO temperature is gradually increased to observe where the off-center displacement starts to increase again. The off-center displacement remains the same up to ∼ 85 K, but begins to rapidly increase when the temperature rises above 85 K.

With this test, we find that the maximum operating temperature of the SMB is not the transition temperature of the YBCO (~95 K) but 70 K. This temperature requirement is satisfied with sufficient margin under the normal operating conditions of our system. We additionally find that, if the off-center displacement occurs due to the temperature increase, it cannot be restored by simply lowering the temperature of the YBCO. Once the displacement has occurred, it is retained unless the SMB is brought to a higher temperature. In order to re-center the rotor, it is necessary to grip it at the center and warm up the YBCO disks above their transition temperature, followed by a re-cooling to flux-pin the rotor in the correct position.

3.4.6 Angle encoding accuracy

There are two primary sources of angle encoding inaccuracy: the timing jitter of the data acquisition system and noise in the encoder readout. The total noise should correspond to less than the 3 μrad $\sqrt{\text{s}}$ (Sec. 3.2.5).

We first discuss timing jitter, and more specifically the uncertainty of CHWP angle timestamp assignment. A BeagleBone Black microcontroller[15] acquires the encoder data, and assigns their timestamps based on its internal 200 MHz free-running clock (Sec. 3.3.6). Since the internal clock has long-timescale frequency drifts, the timestamps must be corrected by referencing the microcontroller to the SAT's master clock, which also synchronizes with detector timestreams. The microcontroller receives the master clock signal as IRIG-B [157] frame and position identifiers at a rate of 10 times per second. There are uncertainties, including jitter and data loss, in the measurement of the encoder and IRIG-B pulses, therefore we determine the CHWP angle after data acquisition by analyzing the full history of the internal timestamps for the two signals. The corrected timestamp is expressed as

$$\hat{t} = t_{\rm true} + \Delta t_{\rm clk}. \tag{3.5}$$

where $\Delta t_{\rm clk}$ is the uncertainty in the correction after synchronizing the encoded angle timestamps to IRIG-B time. The effect of timing jitter on angle encoding accuracy is evaluated by the power spectral density (PSD) of $\Delta t_{\rm clk}$, which is determined by the relative time difference between the internal clock and IRIG-B time:

$$\Delta t_{\rm diff} = t_{\rm bbb}|_{t=t_{\rm true}-\Delta t_{\rm IRIG}} - t_{\rm true} \simeq \Delta t_{\rm bbb} - \Delta t_{\rm IRIG}, \tag{3.6}$$

where $t_{\rm bbb}$ is the internal clock time, $\Delta t_{\rm bbb}$ is the drift of internal clock relative to IRIG-B, and $\Delta t_{\rm IRIG}$ is the timing jitter resulting from the detection of IRIG-B pulses. Since $\Delta t_{\rm bbb}$ and $\Delta t_{\rm IRIG}$ are independent, the PSD is

$$\begin{aligned} {\rm PSD}(\Delta t_{\rm diff}) &= {\rm PSD}(\Delta t_{\rm bbb}) + {\rm PSD}(\Delta t_{\rm IRIG}) \\ &= A f^{-\alpha} + \sigma^2_{\rm IRIG}/10 \quad ({\rm sec}^2 \cdot {\rm sec}), \end{aligned} \tag{3.7}$$

where A and α are the $1/f$ noise parameters of $\Delta t_{\rm bbb}$ and $\sigma^2_{\rm IRIG}$ is the noise variance in terms of the 10 Hz IRIG-pulse detection. The blue dashed curve in Fig. 3.17 shows the corresponding angle jitter due to the timing jitter constructed from Eq. 3.7 multiplied by the angular velocity. The $1/f$ noise is given by $\Delta t_{\rm bbb}$ and the white noise level is determined by $\Delta t_{\rm IRIG}$. The corrected time, $\hat{t}$ (Eq. 3.5), is constructed by synchronizing the internal clock to the IRIG-B signal at a frequency of $f_{\rm sync}$ by linear interpolation. Therefore, the PSD of the uncertainty in the corrected time $\Delta t_{\rm clk}$ is approximately expressed as

$$ {\rm PSD}(\Delta t_{\rm clk}) \simeq \begin{cases} \sigma^2_{\rm IRIG}/10 & f \leq f_{\rm sync}/2, \\ A f^{-\alpha} & f \geq f_{\rm sync}/2 \end{cases} \tag{3.8}$$

At frequencies below the synchronization Nyquist frequency ($f_{\rm sync}/2$), timestamp correction eliminates $1/f$ noise and the white noise of the IRIG detection jitter limits the timing accuracy. At frequencies above $f_{\rm sync}/2$ the timing accuracy still relies on the microcontroller's internal clock, resulting in the small amount of time drift. As can be seen from Fig. 3.17, the angle jitter due to the timing jitter of the corrected time satisfies the requirement at all frequencies.

[15] BeagleBone Black, Beagle Board: https://beagleboard.org/black

Next, we evaluate the encoder readout noise. We place an upper limit on encoder readout noise using the encoder data and the CHWP's smooth rotation. The encoded CHWP angle is

$$\hat{\chi}(t_{\mathrm{true}}) = \chi_{\mathrm{true}}(\hat{t} + \Delta t_{\mathrm{enc}}) + \eta(\chi_{\mathrm{true}}), \tag{3.9}$$

where $\hat{\chi}$ is the encoded rotation angle of the CWHP, χ_{true} is the true rotation angle of the CHWP, and Δt_{enc} is the timing jitter that arises from the detection of photo-encoder pulses. $\eta(\chi_{\mathrm{true}})$ is the non-uniformity of the encoder slot pattern. The CHWP angle jitter is defined by subtracting the smooth rotation:

$$\begin{aligned}\Delta\hat{\chi} &= \hat{\chi}(t_{\mathrm{true}}) - \overline{d\hat{\chi}/dt_{\mathrm{true}}} \cdot t_{\mathrm{true}} \\ &\simeq \Delta\chi_{\mathrm{true}} + \dot{\chi}\Delta t_{\mathrm{clk}} + \dot{\chi}\Delta t_{\mathrm{enc}} + \eta(\chi_{\mathrm{true}}),\end{aligned} \tag{3.10}$$

where $\Delta\chi_{\mathrm{true}}$ is the true drift of the CHWP angle that we would like to measure. Since $\Delta\chi_{\mathrm{true}}$, Δt_{clk}, Δt_{enc} and $\eta(\chi_{\mathrm{true}})$ are independent, the PSD of the CHWP angle jitter is

$$\mathrm{PSD}(\Delta\hat{\chi}) \simeq \mathrm{PSD}(\Delta\chi_{\mathrm{true}}) + \dot{\chi}^2\mathrm{PSD}(\Delta t_{\mathrm{clk}}) + \dot{\chi}^2\mathrm{PSD}(\Delta t_{\mathrm{enc}}) + \mathrm{PSD}(\eta(\chi_{\mathrm{true}})), \tag{3.11}$$

where

$$\dot{\chi}^2\mathrm{PSD}(\Delta t_{\mathrm{enc}}) \simeq \frac{\dot{\chi}^2\sigma_{\mathrm{enc}}^2}{f_{\mathrm{HWP}} \times 1140}\ (\mathrm{rad}^2 \cdot \mathrm{sec}) \tag{3.12}$$

and σ_{enc}^2 is the noise variance in terms of the encoder-pulse detection timing. There are 1140 pulses per revolution. The green solid curve in Fig. 3.17 shows Eq. 3.11 when the CHWP rotates at 2 Hz. The $1/f$ component is the true drift of the CHWP angle, $\Delta\chi_{\mathrm{true}}$. The white noise level is determined by Δt_{enc} and is well below the requirement. The peaks at the harmonics of f_{HWP} arise from $\eta(\chi_{\mathrm{true}})$. f_{sync} is chosen to be 1 Hz to ensure that the timing jitter becomes subdominant to the drift of the CHWP angle at all frequencies.

To demodulate the TES detector timestream sampled at 200 Hz, the raw CHWP angles sampled at $1140 \times f_{\mathrm{HWP}}$ Hz need to be down sampled. In this procedure, the peaks at the higher harmonics of f_{HWP} must be subtracted so as not to contaminate the down-sampled angular timestream. The non-uniformity of the encoder slot pattern, $\eta(\chi_{\mathrm{true}})$, is estimated by time averaging $\Delta\hat{\chi}$ for each angle step of the encoder signal as

$$\eta(\chi_{\mathrm{true}}) \simeq \overline{\Delta\hat{\chi}} \ \text{ for each } (\hat{\chi} \bmod 2\pi). \tag{3.13}$$

The red dotted curve in Fig. 3.17 shows the angle jitter after the slot pattern subtraction and down-sampling. The residual peaks at the harmonics of f_{HWP} are due to the slow modulation of the rotation-synchronous fluctuations of $\dot{\chi}$. The achieved noise level is 0.07 μrad $\sqrt{\mathrm{s}}$, which is more than one order of magnitude lower than the requirement.

3.5 Conclusion

We have presented the requirements, design and performance of the CHWP rotation mechanism for the Simons Observatory Small Aperture Telescopes. This work advances the field of cryogenic polarization

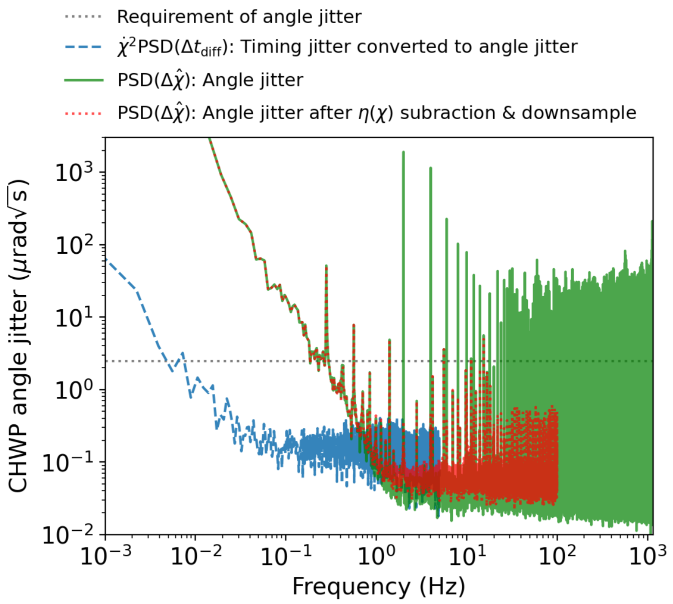

Fig. 3.17 A measurement of the angle encoder performance over 1 hour. The CHWP is constantly rotating at 2 Hz. The high frequency peaks in the raw PSD($\Delta\hat{\chi}$) are due to the non-uniformity of the encoder slot pattern, $\eta(\chi)$. The residual peaks after the $\eta(\chi)$ subtraction and down-sampling correspond to true fluctuation in the rotation angle, which are caused by vibrations of the PTC and the effects of the PID rotation control. The requirement applies only to the white noise level of the angle jitter.

modulators for mm-wave and sub-mm astronomical observations by introducing the largest diameter CHWP constructed to date. The aperture size of the CHWP system was previously constrained by the size of the rotor's magnet ring. By overcoming the manufacturing limitations of the SMB and optimizing the optical design, the size of the system is now limited by the largest available size of sapphire plate.[16] This work has also advanced the CHWP rotation drive techniques to improve operational efficiency, and introduced new methodologies for characterizing CHWP systems, which enabled improvement of the SMB to reduce vibration and evaluate the rotor displacement.

The CHWP for LF frequency is currently under development and will have different design parameters. The center alignment of the rotor will be more challenging since the LF HWP sapphire stack is a factor of 3 ∼ 4 thicker, and thus ∼ 15 kg heavier than the MF HWP. On the other hand, the LF band enjoys significantly less atmospheric fluctuations than the higher frequency bands, and thus the requirements on the CHWP rotation frequency can be relaxed.

Three CHWPs have been built and evaluated for three SATs, and three additional CHWPs are planned to be built. CHWP performance satisfies all requirements, including a 478 mm clear aperture, a rotor temperature of < 70 K, a stator temperature of < 60 K, < 1.6 W of dissipation during continuous operation, rotation frequencies up to 3 Hz, rotation stability within 5 mHz, rotor alignment within 5 mm, and 0.07 μrad $\sqrt{\mathrm{s}}$ of the encoded angle noise. The presented CHWPs are expected to be deployed to the Chilean observation site and to see first light in 2023. This development contributes not only to the SO project but also to the design and trade study for future experiments such as CMB-S4. [1, 4]

[16]Guizhou Haotian Optoelectronics Co., Ltd.

Chapter 4

Ultralight Dark Matter

This chapter serves as an introduction for one of the dark matter (DM) candidates, the axion-like particles (ALPs). In particular, we consider the ultra-light ALPs with the mass around 10^{-22} eV, and discuss their phenomenology through the weak interaction with the photon.

4.1 Cosmological and astrophysical motivation

The astronomical evidence of the DM existence is rich. The first claim of the existence of the DM is from the observation of Coma Cluster [207]. The existence of DM is also supported by the observations of rotation curves of galaxy [159], gravitational lensing [111], and Bullet Cluster [38]. The dynamical measurements tell us the DM mass density in the solar neighborhood is about 0.3-0.5 GeV cm^{-3} [27, 178, 118]. The cosmological evidence of DM is provided by the success of ΛCDM model. ΛCDM describes a universe with an energy budget of dark energy (Λ) and cold DM (CDM) in addition to the baryonic matter. The remarkable success of ΛCDM is the description of the angular power spectrum of the Cosmic Microwave Background (CMB) and the large scale structure (LSS). All these observations support an interpretation that DM is abundant in Milky Way galaxy (MW) and throughout the universe.

4.2 Particle physics motivation

From observations, it is known that DM is made up of stable and electrically neutral particles, and that it interacts through gravity but only weakly with ordinary matters.

Widely accepted approach to construct a particle physics model for the DM candidate is to consider particles which also resolves the shortcoming of the standard model. Weakly interacting massive particles (WIMPs) and axions are the major examples. WIMP is a particle with masses in the GeV to TeV range that weakly interacts with the standard model particles [10]. WIMPs are motivated by a number of beyond standard models and can be produced by a simple production mechanism of thermal freezeout, and have been searched for decades by direct, indirect, and collider methods. The axions are motivated to be DM candidates which solve strong CP problem in quantum chromodynamics (QCD) [143, 197]. Axion is a pseudo-Nambu-Goldstone boson resulting from the spontaneous symmetry breaking of a global chiral U(1) symmetry [54], described by complex scalar field of

$$\varphi = \chi e^{i\phi/f_a}, \tag{4.1}$$

where ϕ is the axion field, f_a is a symmetry breaking scale, and $\theta_a = f_a\phi$ is a misalignment angle. A non-perturbative effects such as string theory or instantons breaks the shift symmetry of $\phi \to \phi + \mathrm{const}$ and gives small mass to the axion with a potential of the following general form

$$V(\phi) = \Lambda^4[1 - \cos(\phi/f_a)], \tag{4.2}$$

where Λ^4 is the scale of the scale of spontaneous symmetry breaking, For small field values, the potential can be expanded into following.

$$V(\phi) = \frac{1}{2}m_a^2\phi^2 + \frac{1}{4!}\lambda\phi^4 + \ldots\ , \tag{4.3}$$

where $m_a = \Lambda^2/f_a$ is the axion mass. For the QCD axion, $\Lambda_{\mathrm{QCD}} \simeq 100$ MeV and the axion mass is

$$m_a \simeq 6 \times 10^{-6}\ \mathrm{eV}\left(\frac{10^{12}\ \mathrm{GeV}}{f_a}\right), \tag{4.4}$$

and predicted to be in the range of $10^{-10} \lesssim m_a \lesssim 10^{-2}$ eV. Also, the axion couples to photon through the coupling constant given as

$$g_{a\gamma\gamma} \simeq \frac{\alpha}{2\pi f_a}c_{a\gamma\gamma}, \tag{4.5}$$

where α is a fine-structure constant and $c_{a\gamma\gamma}$ is a model dependent parameter. There are two major QCD axions with different strength of coupling to photons, KSVZ axion ($c_{a\gamma\gamma} \sim -1.92$) [87, 171] and DFSZ axion ($c_{a\gamma\gamma} \sim 0.75$) [205, 42].

Another approach is to consider DM candidates that may not solve existing problems, but are qualitatively similar to the known particles such that their modification to existing theories may be considered minimal. For example, axion like particles, dark photons, and sterile neutrinos belong to this category. Axion-like particles (ALPs), the focus of this chapter, are pseudo-Nambu-Goldstone bosons with properties similar to the QCD axions, and are predicted by string theories [200, 13, 37]. The difference of ALP from QCD axion is that its coupling constant $g_{a\gamma\gamma}$ (Eq. 4.5) is no longer related with the its mass m_a in contrast to (Eq. 4.4). Threfore, the search for ALP should cover all the $g_{a\gamma\gamma} - m_a$ plane, and the mass of ALP can be ultralight. The ultralight DM, especially around 10^{-22} eV, is of special interest as a DM candidate, which could also address the small scale tensions in the standard cosmological model [71, 75].

The misalignment mechanism is one of the scenarios to produce non-thermal axions or ALPs in the early universe, which can make up all the DM. The simplest misalignment mechanism assumes that global U(1) symmetry that breaks during inflation and the uniform $\theta_a = \phi_i/f_a$ is produced, where ϕ_i is the uniform initial condition (Fig. 4.1). The cosmological evolution of ALPs can be considered from the

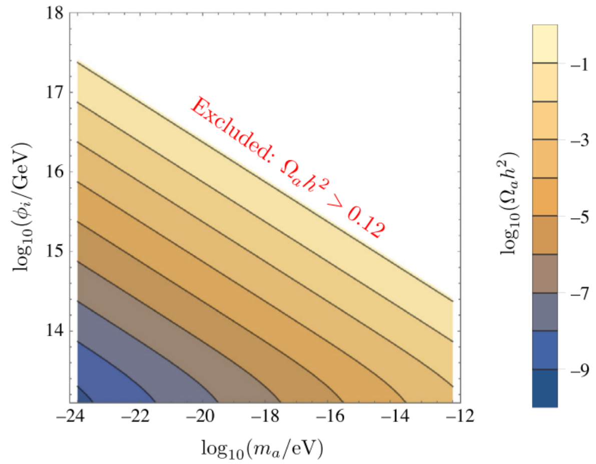

Fig. 4.1 Ultra light ALP density from the misalignment mechanism. Ω_a is the fraction of the axion density. For ALP to constitute all the DM, the universe has to go through the GUT scale energy density $\sim 10^{16}$ GeV. Figure is taken from Marsh [110].

following action [110, 51].

$$S_\phi = \int d^4x \sqrt{-g}\left(\frac{1}{2}g^{\mu\nu}\partial_\mu\phi\partial_\nu\phi - V(\phi)\right). \tag{4.6}$$

We consider the evolution of this field in a flat Friedmann–Robertson–Walker (FWR) metric, with the metric $ds^2 = dt^2 - a^2(t)dx^2$, where $a(t)$ is a scale factor. The equation of motion is

$$\Box\phi - \frac{\partial V(\phi)}{\partial\phi} = 0, \tag{4.7}$$

where d'Alembertian is

$$\Box = \frac{1}{\sqrt{-g}}\partial_\mu(\sqrt{-g}g^{\mu\nu}\partial_\nu). \tag{4.8}$$

Taking only the mass term from the potential, the equation of motion of ALP is

$$\ddot{\phi} + 3H\dot{\phi} + m_a^2\phi = 0, \tag{4.9}$$

where $H = \dot{a}/a$ is a Hubble parameter, and the space derivative is dropped in the FRW metric. This is a simple harmonic oscillator with time dependent Hubble friction term. Figure 4.2 shows the cosmological development of the ALP field. In early universe ($H \gg m_a$), the Hubble friction term dominates and the solution of field is constant at initial values. The ALP has an equation of state of $w = -1$ and behaves like a dark energy. As the universe expands, the Hubble constant gets smaller and smaller, and when H gets smaller than m_a, the ALP starts to oscillate. As the ALP field oscillates, the equation of state also oscillates around zero, resulting in the averaged equation of state to be $w = 0$ and the ALP behaves like DM. For ALP to constitutes all the DM, it has to start oscillating before matter-radiation equality, resulting in $m_a > 10^{-28}$ eV [110].

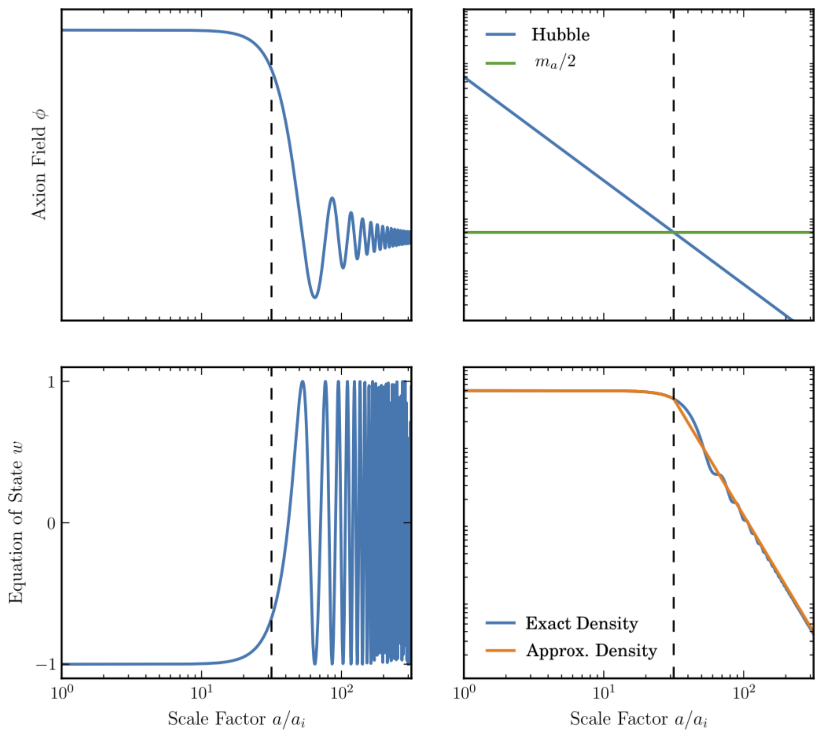

Fig. 4.2 Evolution of the ALP for a radiation dominated universe. ϕ_i and a_i are the initial ALP field and initial scale factor, respectively. Figure is taken from Marsh [110].

From the CMB data and galaxy clustering data, $m_a > 10^{-24}$ eV is required for the ALPs to be CDM, and ALPs with $m_a < 10^{-32}$ eV can take up significant fraction of the Dark energy [70]. The ALPs as dark matter are of particular interest as the candidates to produce "cosmic birefringence" [94, 120, 129].

Finally we consider the limit when the ALP is in sub-Hubble term and oscillates fast, and behaves as DM. This non-relativistic limit describes the ALP DM in MW. Neglecting the Hubble scale and the expansion of the universe, the equation of motion (EOM) is

$$\partial_\nu \partial^\nu \phi + m_a^2 \phi = 0. \tag{4.10}$$

In non-relativistic limit, the plane wave solution of the EOM is expressed as follows.

$$\phi(t) = \phi_0 \exp\left(i\omega_c t + i\vec{k}_c \cdot \vec{x}\right), \tag{4.11}$$

where, $f_c = \omega_c/2\pi = m_a c^2/\hbar$ is the Compton frequency, $\lambda_c = 2\pi/|\vec{k}_c| = \hbar m_a^{-1} c^{-1}$ is the Compton wavelength.

4.3 Classical field approximation of ultralight DM

The ultralight ALP behaves as classical waves. Since we know the local density of DM, the average distance between DM particles can be obtained given a mass of the DM particle. Assuming the standard halo model (SHM), we can also obtain the de-Broglie wavelength, coherence length, of the particle as follows [74].

$$\lambda_{\rm coh} = \frac{\hbar}{m v_{\rm vir}} = 0.48\ {\rm kpc}\left(\frac{10^{-22}\ {\rm eV}}{m}\right)\left(\frac{250\ {\rm km/s}}{v_{\rm vir}}\right) \tag{4.12}$$

where $v_{\rm vir}$ is the velocity dispersion of the MW, virial velocity, and m is the mass of DM. The average number of particles per de-Broglie wavelength volume $\lambda_{\rm coh}^3$ is

$$N_{\rm coh} = \left(\frac{34\ {\rm eV}}{m}\right)^4\left(\frac{250\ {\rm km/s}}{v_{\rm vir}}\right)^3 \tag{4.13}$$

Therefore if the mass of particle is smaller than 30 eV, ultralight DM, the occupation number $N_{\rm coh}$ is larger than 1. Since the occupation number of ultralight DM is large, it naturally requires that ultralight DM to be a boson. In this regime, it is more natural to treat particles as classical waves [175, 63].

4.4 Local dark matter field

It is widely believed that the galactic DM distribution is described by SHM. SHM assumes that during the formation of MW, the DM are trapped within the gravitational potential of the MW and form virialized DM halo [18, 174]. The velocity distribution of the DM of the SHM follows Maxwellian distribution as

$$f_{\rm DM}(\mathbf{v}) = \left(\frac{1}{2\pi v_{\rm vir}^2}\right)^{3/2} \exp\left(-\frac{|\vec{v}-\vec{v}_g|^2}{2v_{\rm vir}^2}\right) \tag{4.14}$$

where $v_{\rm vir}$ = 230 km/s $\sim 10^{-3}c$ is the velocity dispersion in the galactic rest frame, and $v_g \sim$ 220 km/s $\sim 10^{-3}c$ is the speed of our solar system's motion with respect to the galactic rest frame. Using the SHM and the observation of the rotation curve in the MW, a number of groups have estimated the DM energy density to be $\rho_{\rm DM}$ = 0.3 - 0.4 GeV/cm^{-3} [27, 118, 178].

Under the SHM, this ultralight DM's classical waves are a superposition of random velocities and phases. Hereafter we call this classical wave as virialized ultralight field (VULF) [40, 33]. The typical de-Broglie wave length corresponds to the coherence length $\lambda_{\rm coh}$ ($= \hbar m^{-1} v_{\rm vir}^{-1}$) due to the velocity dispersion. In the rest frame of VULF, the oscillation frequency of VULF is given by the Compton frequency, $\omega_c = \frac{mc^2}{\hbar}$. Due to the velocity dispersion of SHM, the Compton frequency gets shifted as follows.

$$\omega_\phi = \omega_c + \frac{m v_{\rm vir}^2}{2\hbar} \tag{4.15}$$

The characteristic coherence time of VULF is

$$\tau_c = \frac{\hbar}{m v_{\rm vir}^2} \tag{4.16}$$

4.5 Light propagation through wave dark matter

The ALP-photon coupling induces the rotation of the polarization angle of light traveling through the ALP background [30, 175]. The complete electromagnetic and pseudo-scalar lagrangian reads [173, 64]

$$\mathcal{L} = \frac{1}{2}\partial_\nu\phi\partial^\nu\phi + V(\phi) - \frac{1}{4}F_{\mu\nu}F^{\mu\nu} + \frac{1}{4}g_{a\gamma\gamma}\phi F_{\mu\nu}\tilde{F}^{\mu\nu} \tag{4.17}$$

where $F_{\mu\nu} = \partial_\mu A_\nu - \partial_\nu A_\mu$ is the electromagnetic tensor and $\tilde{F}^{\mu\nu}$ is its Hodge dual. $g_{a\gamma\gamma}$ is the coupling to the photon, the Chern Simons term. We assume $V(\phi) = \Lambda^4(1-\cos(\phi/f_a)) \simeq \frac{1}{2}m_a^2\phi^2 + O(\phi^4)$. The EOM of scalar field is obtained as

$$(\Box + m_a^2)\phi + \frac{1}{4}g_{a\gamma\gamma}F_{\mu\nu}\tilde{F}^{\mu\nu} = 0 \tag{4.18}$$

The last term, so ca-called the back reaction term, can be ignored in the leading order of $g_{a\gamma\gamma}$. Therefore, in the leading order the scalar field is free particle (Eq. 4.10). Under the condition that the wavelength of the background ALP field is much longer than that of the photons, the EOM of the photon in the leading order of $g_{a\gamma\gamma}$ is

$$\Box\mathbf{A} = g_{a\gamma\gamma}\left(\dot{\phi}\nabla\times\mathbf{A} + \dot{\mathbf{A}}\times\nabla\phi\right). \tag{4.19}$$

Here we assumed temporal gauge, $A_0 = 0$ and Coulomb gauge $\nabla\cdot\mathbf{A} = 0$. We consider the plane wave with circular polarization mode with angular frequency of $\omega_\pm$ and the wave number of k as a solution.

$$\mathbf{A}_\pm = A(\hat{x} \pm i\hat{y})\exp\left(i(kz - \omega_\pm t)\right), \tag{4.20}$$

Then, to a lowest order of $g_{a\gamma\gamma}$, the dispersion relation is given by

$$\omega_\pm \simeq k \pm \frac{1}{2}g_{a\gamma\gamma}\left(\frac{\partial\phi}{\partial t} + \nabla\phi\right) = k \pm \frac{1}{2}g_{a\gamma\gamma}\frac{d\phi}{dt}. \tag{4.21}$$

Therefore, under the ALP background, the phase velocities for the left and right-handed polarization modes are different. The direction of the linear polarization rotates when the speed of right-handed and the left-handed circular polarization are different. The amount of rotation angle of linear polarization is obtained by integrating the difference of the angular frequency over the path of light

$$\Delta\psi = \int dt\,(\omega_+ - \omega_-) = \frac{g_{a\gamma\gamma}}{2}(\phi_{\mathrm{detected}} - \phi_{\mathrm{emitted}}). \tag{4.22}$$

which leads to the difference of the scalar field at the both ends of the light path. ϕ_{detected} and ϕ_{emitted} represents the field value where the light was observed and emitted, respectively. Note that this rotation effect is independent of the details of the scalar field along the photon path.

4.6 Random Gaussian model

The goal of this section is to discuss the wave dynamics of VULF and derive the two-point correlation function from the equations of motion. One of the plane wave (Eq. 4.11) which comprises the VULF is expressed as

$$\phi_{\vec{k}}(\vec{x},t) = c_k \cos\left(\omega_c(1+k^2/2k_0^2)t + \vec{k}\cdot\vec{x}\right) + s_k \sin\left(\omega_c(1+k^2/2k_0^2)t + \vec{k}\cdot\vec{x}\right), \tag{4.23}$$

where $\vec{k} = m\vec{v}/\hbar$ is the wave vector, $k_0 = mc/\hbar$, c_k and s_k are random variables that follow a standard normal distribution. Eq. 4.23 oscillates at the Doppler shifted Compton frequency (Eq. 4.15). This can be re-written as

$$\phi_{\vec{k}}(\vec{x},t) = \alpha_k \cos\left(\omega_c(1+k^2/2k_0^2)t + \vec{k}\cdot\vec{x} + \theta_k\right), \tag{4.24}$$

where, $\alpha_{k,i} = \sqrt{c_k^2 + s_k^2}$ follows the Rayleigh distribution with scale parameter of 1, and $\theta_{k,i} = \arctan(s_k/c_k)$ follows the uniform distribution from 0 to 2π.

The VULF is expressed as the superposition of random Gaussian waves as

$$\phi(\vec{x},t) = \frac{\sqrt{\rho_{\rm DM}(\vec{x})}}{m_a} \int d\vec{k} \sqrt{f_{\rm DM}\left(\vec{k}\right)} \left\{c_k \cos\left(\omega_c(1+k^2/2k_0^2)t + \vec{k}\cdot\vec{x}\right) + s_k \sin\left(\omega_c(1+k^2/2k_0^2)t + \vec{k}\cdot\vec{x}\right)\right\}, \tag{4.25}$$

where $f_{\rm DM}$ is a Maxwellian distribution of SHM (Eq. 4.14) [40, 53, 74]. The normalization factor is determined by requiring the ensemble average of the time averaged energy density, $\langle\phi(\vec{x},t)^2\rangle_t = \phi_0(x)^2/2$, to be equal to the DM density. The ensemble average is determined by $\phi_{\rm DM}^2 \equiv \langle\phi_0(\vec{x})^2\rangle$, therefore

$$\frac{\phi_{\rm DM}^2}{2} = \frac{\rho_{\rm DM}}{m^2} \iint d\vec{k}d\vec{k'}\ \sqrt{f_{\rm DM}\left(\vec{k}\right) f_{\rm DM}\left(\vec{k'}\right)}\delta^3(\vec{k}-\vec{k'}) = \frac{\rho_{\rm DM}}{m^2} \tag{4.26}$$

Since $\phi(\vec{x},t)$ is a superposition of many Gaussian random variables, each point of $\phi(\vec{x},t)$ is also a Gaussian random variable with a mean of zero and a standard deviation of $\sqrt{\rho(\vec{x})}/m$.

In our mass scale of interest ($m \sim 10^{-22}$ eV), the total observation time (~years) is much shorter than the coherence time of VULF ($\sim 10^6$ years), which is determined by the velocity dispersion of the local DM. Therefore, for the ultralight DM, the time development of the VULF at each point can be approximately expressed as follows.

$$\phi(\vec{x},t) = \frac{\sqrt{\rho_{\rm DM}(\vec{x})}}{m} \left\{\phi_c \cos(\omega_c t) + \phi_s \sin(\omega_c t)\right\} = \frac{\sqrt{\rho_{\rm DM}(\vec{x})}}{m} \alpha \cos(\omega_c t + \theta), \tag{4.27}$$

where, the net amplitude ϕ_c and ϕ_s are random variables that follow a standard normal distribution. The α is a random variable that follows the Rayleigh distribution with scale factor 1, and θ is a random variable that follows uniform distribution from 0 to 2π.

Figure 4.3 shows the simulated time evolution of the VULF [33]. If the observation time is much shorter than the coherence time of VULF (τ_c), the time evolution of VULF is single mode sine curve (Eq. 4.27) as shown in magnified view of Fig. 4.3. In the longer time scale, the net amplitude in each short time scales is randomly fluctuating with Rayleigh distribution [33].

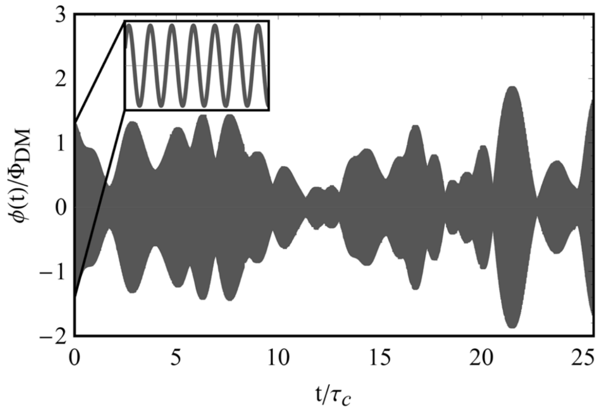

Fig. 4.3 Simulated VULF in time-domain. Figure is taken from Centers et al. [33].

4.6.1 Polarization oscillation

As we discussed in Sec. 4.5, the amount of polarization angle rotation is given by the difference of VULF field where the photon was emitted and detected.

$$\Delta\psi = \frac{g_{a\gamma\gamma}}{2}\Delta\phi \tag{4.28}$$

$$\Delta\phi = \phi_{\text{detected}}(\vec{x}, t) - \phi_{\text{emitted}}(\vec{y}, s) \tag{4.29}$$

The key parameter which determines the sensitivity to the stochastic VULF is the variance of the difference between two points of VULF $\Delta\phi$, but it is important to note that the correlation between the two points exists. We define the correlation (γ) between two points of VULF as follows. As we see later, the correlation only depends on the distance between two points.

$$\gamma(\vec{x} - \vec{y}, t - s) = \frac{\text{Cov}\left[\phi(\vec{x}, t), \phi(\vec{y}, s)\right]}{\sqrt{\text{Cov}\left[\phi(\vec{x}, t), \phi(\vec{x}, t)\right] \cdot \text{Cov}\left[\phi(\vec{y}, s), \phi(\vec{y}, s)\right]}} \tag{4.30}$$

$$= \frac{m^2}{\sqrt{\rho(\vec{x})\rho(\vec{y})}} \left\langle \phi(\vec{x}, t)\phi(\vec{y}, s) \right\rangle \tag{4.31}$$

The last equality holds because $\phi(\vec{x}, t)$ is a Gaussian random variable with a mean of zero and a standard deviation of $\sqrt{\rho(\vec{x})}/m$. The 2-point function of VULF characterizes the correlation. The variance of $\Delta\phi$ is expressed as follows

$$\left\langle (\Delta\phi)^2 \right\rangle = \left\langle \phi(\vec{x}, t)^2 \right\rangle + \left\langle \phi(\vec{y}, s)^2 \right\rangle - 2\gamma \sqrt{\left\langle \phi(\vec{x}, t)^2 \right\rangle \left\langle \phi(\vec{y}, s)^2 \right\rangle} \tag{4.32}$$

$$= \frac{1}{m^2} \left(\rho(\vec{x}) + \rho(\vec{y}) - 2\gamma \sqrt{\rho(\vec{x})\rho(\vec{y})} \right) \tag{4.33}$$

Therefore, the time evolution of the difference of two points can be expressed as follows

$$\Delta\phi(t, \vec{d}, \tau) = \frac{1}{m} \sqrt{\rho(\vec{x}) + \rho(\vec{y}) - 2\gamma(\vec{d}, \tau) \sqrt{\rho(\vec{x})\rho(\vec{y})}}\, \alpha \cos(\omega_c t + \theta), \tag{4.34}$$

where $\vec{d} \equiv \vec{x} - \vec{y}$ and $\tau = t - s$.

As we derive in Appendix. B, in the mass scale of interst, the correlation between the two points of VULF is given as

$$\gamma(\vec{d}, \tau) = \exp\left(-\frac{|\vec{d} - \vec{v}_g \tau|^2}{2\lambda_{\mathrm{coh}}^2}\right) \cos\left(\omega_c(1 + v_g^2/2c^2)\tau + \frac{m}{\hbar}\vec{v}_g \cdot \vec{d}\right). \tag{4.35}$$

This correlation function was first derived by Derevianko [40].

4.6.2 Size of light source

In the previous section, we implicitly assumed that the size of observer (the region where the light is detected) and the light source (the region where the light is emitted) are negligibly small compared with the Compton wavelength of VULF. Usually the size of observer is negligible but the size of light source can be non-negligible for some astrophysical DM search. Without loss of generality, we set $\vec{x} = \vec{0}, t = 0$. In this case, the effective field difference is expressed as

$$\Delta\phi = \frac{1}{V_{\mathrm{src}}} \int_{\mathrm{src}} d\delta\vec{y} \, \left(\phi_{\mathrm{obs}}(\vec{0}, 0) - \phi_{\mathrm{src}}(\vec{y} + \delta\vec{y}, s + \delta s)\right) \tag{4.36}$$

$$= \phi_{\mathrm{obs}}(\vec{0}, 0) - \frac{1}{V_{\mathrm{src}}} \int d\delta\vec{y} \, \phi_{\mathrm{src}}(\vec{y} + \delta\vec{y}, s + \delta s) \tag{4.37}$$

$$\equiv \phi_{\mathrm{obs}} - \overline{\phi_{\mathrm{src}}}, \tag{4.38}$$

where V_{src} is the volume of the light source region, $\int_{\mathrm{src}} d\delta\vec{y}$ indicates integration over the region of light source. $s = |\vec{y}|/c, \delta s = (|\vec{y} + \delta\vec{y}| - |\vec{y}|)/c$, and $\overline{\phi_{\mathrm{src}}}$ is the mean VULF at the regions of the light source. The variance of the mean VULF at the source region is determined by the correlation function as

$$\left\langle \left(\overline{\phi_{\mathrm{src}}}\right)^2 \right\rangle = \frac{1}{V_{\mathrm{src}}^2} \iint_{\mathrm{src}} d\delta\vec{y} \, d\delta\vec{y}' \, \left\langle \phi(\vec{y} + \delta\vec{y}, s + \delta s)\phi(\vec{y} + \delta\vec{y}', s + \delta s') \right\rangle \tag{4.39}$$

$$= \frac{1}{V_{\mathrm{src}}^2} \iint_{\mathrm{src}} d\delta\vec{y} \, d\delta\vec{y}' \, \frac{\sqrt{\rho(\vec{y} + \delta\vec{y})\rho(\vec{y} + \delta\vec{y}')}}{m_a^2} \gamma(\delta\vec{y} - \delta\vec{y}', \delta s - \delta s') \tag{4.40}$$

Substituting Eq. 4.35 and neglecting v_g for simplicity, the variance of the mean VULF at the source leads to

$$\left\langle \left(\overline{\phi_{\mathrm{src}}}\right)^2 \right\rangle \simeq \frac{1}{V_{\mathrm{src}}^2} \iint_{\mathrm{src}} d\delta\vec{y} \, d\delta\vec{y}' \, \frac{\sqrt{\rho(\vec{y} + \delta\vec{y})\rho(\vec{y} + \delta\vec{y}')}}{m_a^2} \exp\left(-\frac{|\delta\vec{y} - \delta\vec{y}'|}{2\lambda_{\mathrm{coh}}^2}\right) \cos\left(\omega_c(\delta s - \delta s')\right) \tag{4.41}$$

$$\simeq \frac{1}{V_{\mathrm{src}}^2} \iint_{\mathrm{src}} d\delta\vec{y} \, d\delta\vec{y}' \, \frac{\sqrt{\rho(\vec{y} + \delta\vec{y})\rho(\vec{y} + \delta\vec{y}')}}{m^2} \exp\left(-\frac{|\delta\vec{y} - \delta\vec{y}'|}{2\lambda_{\mathrm{coh}}^2}\right) \cos\left(\frac{|\vec{y} + \delta\vec{y}| - |\vec{y} + \delta\vec{y}'|}{\lambda_c}\right) \tag{4.42}$$

If the region of the light source is larger than the Compton wavelength ($\lambda_c \sim 10^{-3}\lambda_{\mathrm{coh}}$) of the VULF, the $\left\langle \left(\overline{\phi_{\mathrm{src}}}\right)^2 \right\rangle$ averages out to zero due to the oscillation of the correlation within the region [35].

If the region of the light source is smaller than the Compton wavelength, the VULF is coherent inside the region and the variance of the mean VULF can be simplified as

$$\left\langle \left(\overline{\phi_{\rm src}}\right)^2 \right\rangle \simeq \frac{\rho(\vec{y})}{m^2} \frac{1}{V_{\rm src}^2} \iint_{\rm src} d\delta\vec{y}\, d\delta\vec{y}'\ \gamma(\delta\vec{y} - \delta\vec{y}', \delta s - \delta s') \equiv \frac{\rho_{\rm src}}{m^2}\gamma_{\rm src}, \tag{4.43}$$

where $\gamma_{\rm src}$ is the mean internal correlation with in the light source. If we simply assume that the source region is cube-shaped area with one side $\lambda_{\rm src}$ ($V_{\rm src} = \lambda_{\rm src}^3$), the $\gamma_{\rm src}$ leads to

$$\gamma_{\rm src} \simeq \frac{1}{V_{\rm src}^2} \iint_{\rm src} d\delta\vec{y}\, d\delta\vec{y}'\ \cos\left(\frac{|\vec{y} + \delta\vec{y}| - |\vec{y} + \delta\vec{y}'|}{\lambda_c}\right) \tag{4.44}$$

$$\simeq \frac{1}{V_{\rm src}^2} \lambda_{\rm src}^4 \lambda_c^2\, 2\left(1 - \cos\left(\frac{\lambda_{\rm src}}{\lambda_c}\right)\right) \tag{4.45}$$

$$\simeq \mathrm{sinc}^2\left(\frac{\lambda_{\rm src}}{2\lambda_c}\right), \tag{4.46}$$

where sinc is unnormalized sinc function, and assumed $\lambda_{\rm src} \ll |\vec{y}|$.

The variance of the effective field difference leads to

$$\left\langle (\Delta\phi)^2 \right\rangle = \left\langle \phi_{\rm obs}^2 \right\rangle + \left\langle \left(\overline{\phi_{\rm src}}\right)^2 \right\rangle - 2\gamma_{\rm obs,src} \sqrt{\left\langle \phi_{\rm obs}^2 \right\rangle \left\langle \left(\overline{\phi_{\rm src}}\right)^2 \right\rangle} \tag{4.47}$$

$$= \frac{1}{m^2}\left(\rho_{\rm obs} + \gamma_{\rm src}\rho_{\rm src} - 2\gamma_{\rm obs,src}\sqrt{\rho_{\rm obs}\gamma_{\rm src}\rho_{\rm src}}\right), \tag{4.48}$$

where $\gamma_{\rm obs,src}$ is the correlation between the observer and the light source

$$\gamma_{\rm obs,src} \equiv \frac{\mathrm{Cov}\left[\phi_{\rm obs}, \overline{\phi_{\rm src}}\right]}{\sqrt{\mathrm{Cov}\left[\phi_{\rm obs}, \phi_{\rm obs}\right] \mathrm{Cov}\left[\overline{\phi_{\rm src}}, \overline{\phi_{\rm src}}\right]}} \tag{4.49}$$

In conclusion, the sensitivity to the polarization oscillation depends crucially on the correlation between the observer and the light source ($\gamma_{\rm obs,src}$), as well as on the mean internal correlation within the light source ($\gamma_{\rm src}$), both of which are described by the two-point function of VULF.

4.7 Stochastic effect on polarization oscillation

A number of experiments are searching ALP using the polarization rotation effect. We discuss the stochastic effect of polarization oscillation for typical extreme cases, and classify the experiments. From the result of Sec. 4.6.1 and Sec. 4.6.2, we obtained the stochastic effect of VULF on the polarization rotation as follows

$$\Delta\psi(t, \vec{d}, \tau) = \frac{g_{a\gamma\gamma}}{2}\Phi\, \alpha \cos(\omega_c(1 + v_g^2/2)t + \theta), \tag{4.50}$$

where α is a random variable that follows the Rayleigh distribution with scale factor 1. θ is a random variable that follows uniform distribution from 0 to 2π,

$$\Phi = \frac{1}{m_a}\sqrt{\rho_{\rm obs} + \gamma_{\rm src}\rho_{\rm src} - 2\gamma_{\rm obs,src}\sqrt{\rho_{\rm obs}\gamma_{\rm src}\rho_{\rm src}}} \tag{4.51}$$

is the effective amplitude of the field,

$$\gamma_{\mathrm{obs,src}} = \exp\left(-\frac{|\vec{d} - \vec{v}_g\tau|^2}{2\lambda_c^2}\right)\cos\left(\omega_c(1 + v_g^2/2c^2)\tau + \frac{m_a}{\hbar}\vec{v}_g \cdot \vec{d}\right) \tag{4.52}$$

is the correlation of VULF between the light source and the observer. Therefore, from the measurement of the oscillation of the polarization angle of the light, the ALP-photon coupling constant $g_{a\gamma\gamma}$ can be obtained from its amplitude, and the ALP mass can be obtained from its frequency.

Case1: Distance is shorter than coherence length

When the distance between the two point is smaller than the coherence length, $\gamma_{\mathrm{obs,src}}$ and γ_{src} are close to 1. Also the density at the observer and the light source should be close. the polarization oscillation is largest when the distance corresponds to the odd multiple of the half of the Compton wavelength.

$$\Delta\psi(t, \vec{d}, \tau) \simeq \frac{g_{a\gamma\gamma}\sqrt{\rho_{\mathrm{DM}}}}{m_a}\left|\sin\left(\frac{\omega_c(1 + v_g^2/2c^2)\tau + \frac{m_a}{\hbar}\vec{v}_g \cdot \vec{d}}{2}\right)\right|\alpha\cos\left(\omega_c(1 + v_g^2/2c^2)t + \theta\right) \tag{4.53}$$

The interferometric laboratory searches utilizing polarization rotation effect [134, 107, 128] belong to this case.

Case2: Distance is longer than coherence length

In this regime, $\gamma_{\mathrm{obs,src}}$ is zero. Therefore, the polarization oscillation is expressed as follows.

$$\Delta\psi(t, \vec{d}, \tau) \simeq \frac{g_{a\gamma\gamma}\sqrt{\rho_{\mathrm{obs}} + \gamma_{\mathrm{src}}\rho_{\mathrm{src}}}}{2m_a}\alpha\cos\left(\omega_c(1 + v_g^2/2c^2)t + \theta\right) \tag{4.54}$$

The ALP search based on the polarimetry of astronomical objects, such pulsars or the proto-planetary disk, belong to this case [141, 56, 35, 109, 20, 32, 108].

If the size of light source is much larger than the Compton wavelength of VULF, then $\gamma_{\mathrm{src}} \to 0$ and the polarization oscillation is expressed as follows.

$$\Delta\psi(t, \vec{d}, \tau) \simeq \frac{g_{a\gamma\gamma}\sqrt{\rho_{\mathrm{obs}}}}{2m_a}\alpha\cos\left(\omega_c(1 + v_g^2/2c^2)t + \theta\right) \tag{4.55}$$

The ALP search based on the cosmic microwave background belongs to this case [49, 25, 24, 179, 152].

4.8 Current state of the field

The search for axion and ALP are performed wide range of mass scale, using wide variety of methods including haloscopes and high energy astrophysics. Figure 4.4 shows the current constraints on the axion-photon coupling constant [133]. The colored regions are excluded. Figure 4.5 shows the current constraints for the ultralight ALP [133]. The dashed curves are the projected limits. The search for the ultralight ALP from the axion-like polarization oscillation by the light from astrophysical objects

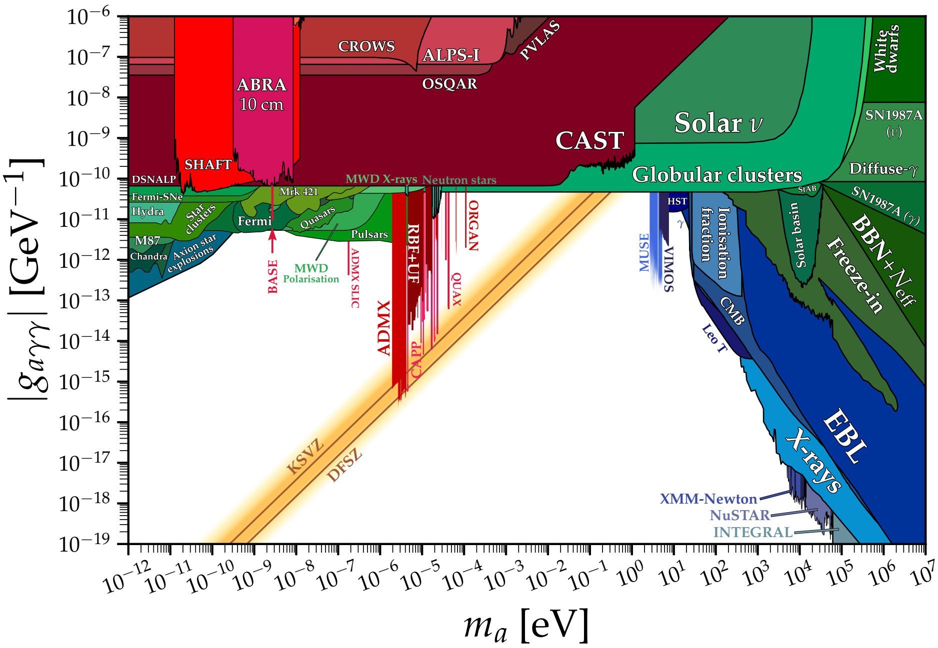

Fig. 4.4 Current limits on axion-photon coupling $g_{a\gamma\gamma}$. The figure is taken from cajohare/AxionLimits [133].

has been conducted, using radio galaxies [169], jets in active galaxies [141], protoplanetary disks [56], pulsars [109, 20, 32], and the cosmic microwave background (CMB) [49, 25, 24, 179, 152].

One of the tightest upper bounds is placed by the absence of the suppression of CMB E-mode power spectrum due to the axion-like oscillation in the recombination era [49]. The tightest possible constraint in this method is limited by the cosmic variance of the CMB power spectrum, and is shown by the dotted line in the Fig. 4.5. The 95.5% upper bound of 5.0×10^{-13} GeV^{-1} at $m_a < 10^{-12}$ eV is also placed from the absence of the distortions of the X-ray spectrum of the quasar H1821+643 due to the ALP-photon coupling [177]. The lower bound of ALP mass of 2.0×10^{-21} eV (2σ C.L.) is obtained from Lyman-α forest data [77], and 2.9×10^{-21} eV with 95% confidence from the absence of suppression of the low-mass DM halo formation [41].

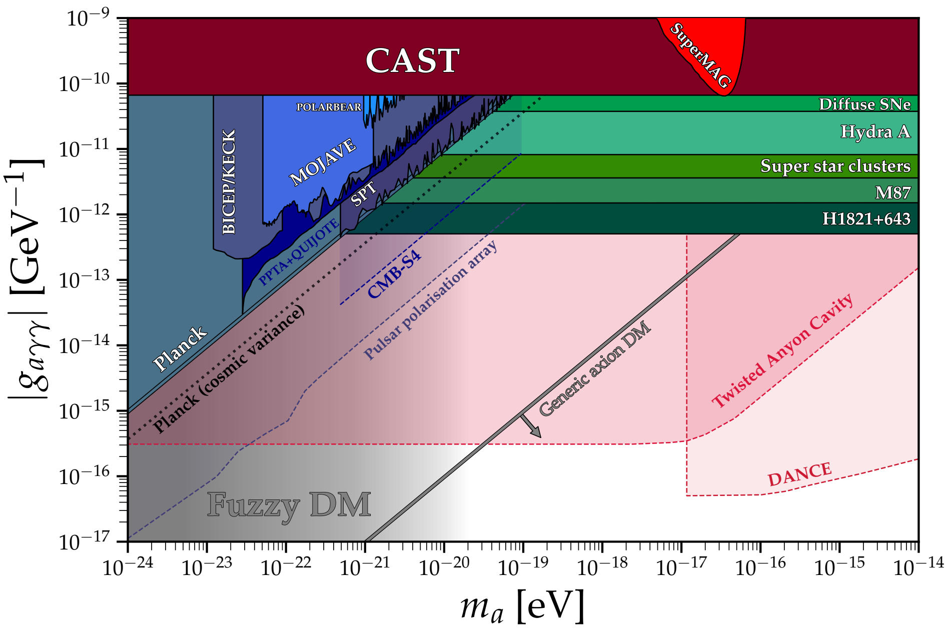

Fig. 4.5 Current limits on ultralight axion-photon coupling $g_{a\gamma\gamma}$. The dashed curves and dotted curves are the projected limits. The figure is taken from cajohare/AxionLimits [133].

Chapter 5

Search for axion-like polarization oscillation in Crab nebula with POLARBEAR

This chapter describes the ALP search from the polarization oscillation measurements of the Crab Nebula at millimeter waves. This chapter is organized as follows. Section 5.1 gives the brief introduction of the ALP search from the ALP induced polarization oscillation. Section 5.2 gives the brief review of the phenomenology of ALP and how the signal appears for the case of Tau A. Sections 5.3 and 5.4 describe the data set and its selection. Sections 5.5 through 5.8 describe the detailed analysis procedure from the time domain to the polarization oscillation spectra. Section 5.9 describes the data validation methods. Section 5.10 describes the results. Section 5.11 describes dedicated studies for the evaluation of systematics. Discussion and conclusion are described in Sec. 5.12 and Sec. 5.13, respectively. This chapter overlaps substantially with POLARBEAR Collaboration [154].

5.1 Introduction

The pseudo scalar field which couples to photon through Chern-Simons term, axion or axion-like particle (ALP), is one of the candidates for the dark matter (DM). The axion was first proposed to solve the stong CP problem [143, 197], while similar particles called ALPs are predicted by string theories [200, 13, 37]. One important property of ALP is that it can be very light ($\sim 10^{-22}$ eV), becoming bosonic ultralight DM, fuzzy DM, or wave DM [51, 74].

The net rotation of polarization angle is given by the difference of ALP field where the light was emitted and detected.

$$\psi(t) = \frac{g_{a\gamma\gamma}}{2}\left(\phi_{\mathrm{detection}} - \phi_{\mathrm{emission}}\right) \tag{5.1}$$

where the $g_{a\gamma\gamma}$ is the ALP-photon coupling constant, ϕ is the ALP field.

The search for axion-like polarization oscillation has been conducted by the light from astrophysical objects, using radio galaxies [169], jets in active galaxies [141], protoplanetary disks [56], pulsars [109, 20, 32], and the cosmic microwave background (CMB) [49, 25, 24, 179, 152]. In this study, we use Crab

Nebula (hereafter referred to as Tau A), the brightest astronomical sources for the millimeter wave telescope which has widely been used for the polarization angle calibration [15, 16, 81], to search for the axion-like polarization oscillation [35]. We use the observations by the Polarbear experiment, a ground-based experiment observing the polarization of the CMB from the Atacama Desert in Chile [12, 85], at 150 GHz from 2015 to 2016.

The precise time-resolved polarimetry of Tau A is an active research topic in astrophysics, and also important for understanding the dynamics of Tau A [124, 50, 29]. If significant polarization oscillation of Tau A is discovered, further study is necessary to distinguish ALP induced oscillation from intrinsic variability of Tau A.

5.2 Polarization oscillation of Crab Nebula

During the formation of the Milky Way galaxy, the DM relax into a gravitational potential and form DM halo with a Maxwellian velocity distribution with a characteristic dispersion velocity of $v_{\mathrm{vir}} \sim 10^{-3}c$, described by standard halo model (SHM) [174, 18]. We consider the statistical properties of such an ultralight ALP field, called the virialized ultralight field (VULF) [40, 53, 33]. Neglecting the velocity of DM field, the ultralight field oscillates at their Compton frequency ($= m_a c^2 \hbar^{-1}$), where m_a is the mass of ALP. This velocity distribution leads to the spectral broadening of the oscillation frequency characterized by the coherence time τ_{coh} ($= m_a v_{\mathrm{vir}}^2 \hbar^{-1}$), and also leads to the spatial dispersion characterized by the coherence length λ_{coh} ($= \hbar m_a^{-1} v_{\mathrm{vir}}^{-1}$). In the limit that the observation time is much shorter than the coherence time of ALP, the time development of ALP field is described as a single mode sinusoid as follows.

$$\phi(t) = \phi_c \sin\left(\frac{m_a c^2}{\hbar} t\right) + \phi_s \cos\left(\frac{m_a c^2}{\hbar} t\right) \tag{5.2}$$

Since the field modes of different frequency and random phase governed by SHM interfere with each other, the net amplitude (ϕ_c, ϕ_s) exhibit stochastic behavior, and follow Gaussian distribution with the following variance $\langle|\phi_c|^2\rangle = \langle|\phi_s|^2\rangle = \phi_{\mathrm{DM}}^2/2$. The ϕ_{DM}^2 is determined by the average local DM density $\rho_{\mathrm{DM}} \sim 0.3\ \mathrm{GeV/cm^{-3}}$, and thus

$$\phi_{\mathrm{DM}} = \frac{\hbar}{m_a c}\sqrt{2\rho_{\mathrm{DM}}}. \tag{5.3}$$

Finally, we discuss the axion-like polarization oscillation signal for the case of Tau A. Tau A is 2000 ± 500 pc away from the earth [84], and its diameter is about 1.7 pc [67]. As shown in Fig. 5.1, in our mass scale of interst, the distance to Tau A is much longer than the coherence length of ALP, thus the oscillation amplitudes of local field and the field at Tau A are independent. Since the size of Tau A is much larger than the Compton wavelength ($= \hbar m_a^{-1} c^{-1}$) of ALP, the oscillation at Tau A averages out, because various phases of oscillation at Tau A contributes to the signal [See Eq. (2.18) of 35]. Therefore, the search of axion-like polarization oscillation by Tau A is only sensitive to the local ALP field, and the signal is modeled as follows.

$$\psi(t) = \psi_0 + \frac{g_{a\gamma\gamma}}{2}\phi_{\mathrm{local}}(t), \tag{5.4}$$

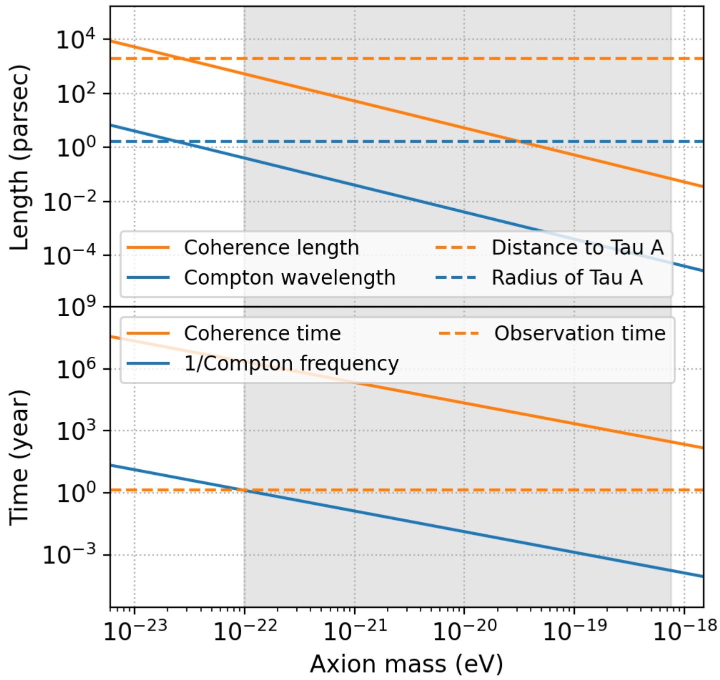

Fig. 5.1 Top: Comparison of typical scales of ALP field and the typical scales of Tau A. Bottom: Comparison of the typical time scales of ALP field and the observation time of this study. The gray shaded region represents the ALP mass scale of interest in this study.

where ψ_0 is the polarization angle of Tau A, and $\phi_{\mathrm{local}}(t)$ is the local stochastic ALP field, which oscillates according to Eq. 5.2.

5.3 Data set

This section describes the data set of POLARBEAR experiment used for axion-like polarization oscillation search in this study. From 4th to 5th season, POLARBEAR observed Tau A several times per week, 220 observations in total (Fig. 5.3). This data set was analyzed for the polarization calibration of POLARBEAR Collaboration [151]. In this study, we re-analyze the same data set adopting a blind-analysis framework [91]. The polarization angle of Tau A in each observation is not seen (blinded) until the validation of the data analysis is completed (Sec. 5.9), i.e. the criteria for the internal consistency test (Sec. 5.9.3) are met, and the possible systematic effects are evaluated (Secs. 5.9.4 and 5.11). The polarization maps and the average absolute angle of Tau A (ψ_0) are not blinded.

The POLARBEAR receiver employs a total of 1274 transition-edge sensor (TES) bolometers cooled to 0.3 K observing the sky through lenslet-coupled dipole antennas [11]. Tau A has an angular size of 7′×5′ [60], while POLARBEAR has a beam with a 3.6′ beam FWHM. Therefore, we do not examine the detailed structure of Tau A. The calibration is performed using the average polarization angle of Tau A (Fig. 5.2). Tau A is at declination of 22 degrees and POLARBEAR is at −23 degrees latitude. Therefore, the highest elevation of Tau A observed by POLARBEAR is 45 degrees (Fig. 5.4). The ideal time to observe Tau A is when it is at highest elevation to minimize the atmospheric loading. However, since observations of

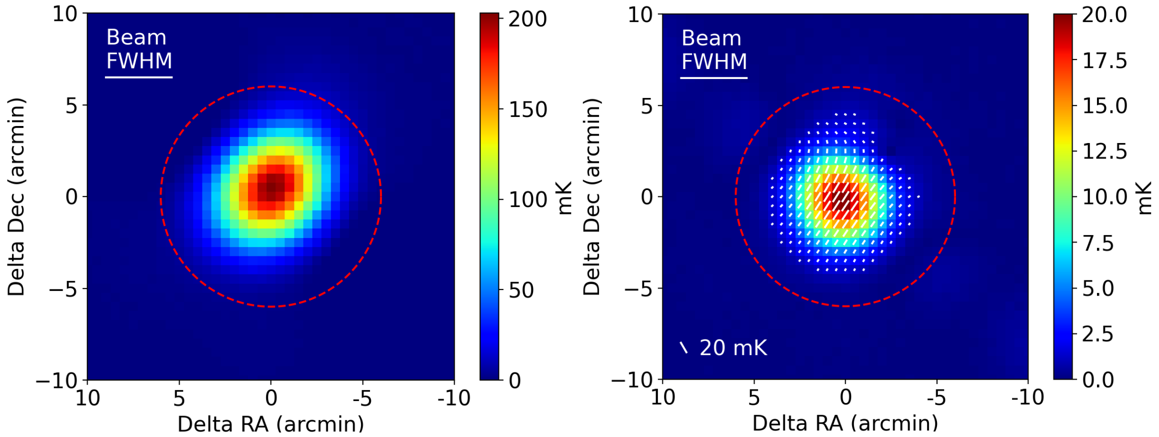

Fig. 5.2 4th and 5th season co-added polarization intensity map of Tau A observed by POLARBEAR. The orientations of bars in map pixels represent average polarization angles (ψ_0) at each map pixel. The red dashed circle represents the integration region to estimate average Tau A angle or evaluate systematic effects, which is consistently used in this study.

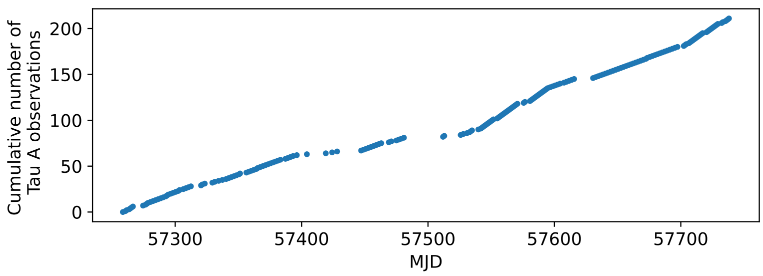

Fig. 5.3 All the Tau A observation from 3rd season to 5th season of POLARBEAR experiment. MJD stands for modified Julian date.

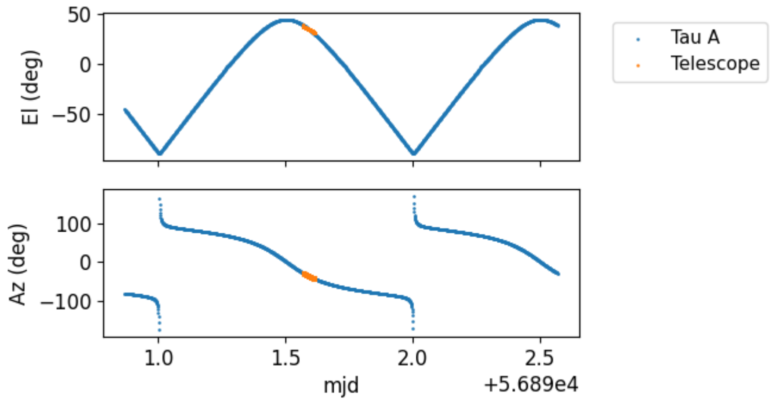

Fig. 5.4 Typical observation timing of Tau A. The blue curve is the ground coordinates of the Tau A as seen from the observing site, and the orange line is the telescope pointing during the observation.

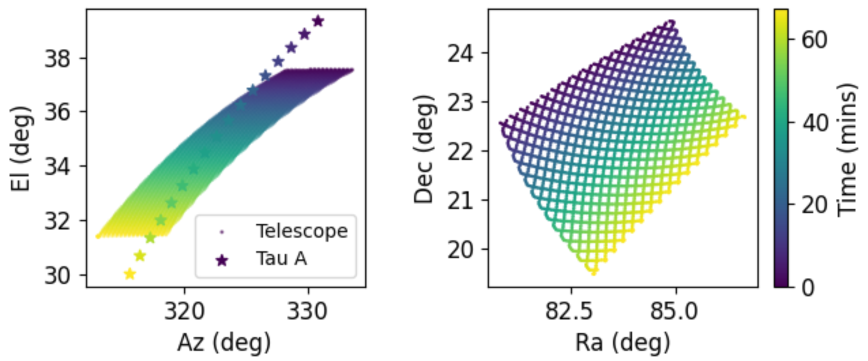

Fig. 5.5 Raster scan pattern of Tau A observation. Left: scan pattern in Horizontal coordinate Right: scan pattern in Equatorial coordinate.

the CMB have the highest priority, Tau A is observed when is sets from 39 degrees to 30 degrees in elevation. Figure 5.5 shows the scan pattern of Tau A observation. POLARBEAR observes Tau A using a raster scan pattern. The telescope scans 5.5 degrees back-and-forth in azimuth at 0.2 degree/s, while the elevation continuously tracks Tau A. Between each sweep in azimuth, called a subscan, the elevation changes by 2′, about half of the beam width.

Before and after every observation, a series of calibrations is carried out to characterize the relative detector gain, gain drift, detector time constant. These values can be different depending on how each TES was tuned which depends on optical conditions of the atmosphere. We use a chopped 700 °C black body source, stimulator, is used to calibrate detector gain and time constant. The stimulator is placed backside of the secondary mirror and injects the chopped optical signal from thermal source through the small hole on the secondary mirror. The illumination pattern of the stimulator on the focal plane is not uniform, but the relative brightness of stimulator on the focal plane is calibrated by the planet observation, which uniformly illuminate the focal plane. The stimulator calibrates the relative gain variations for each observation. The first order gain drift within one observation is determined by

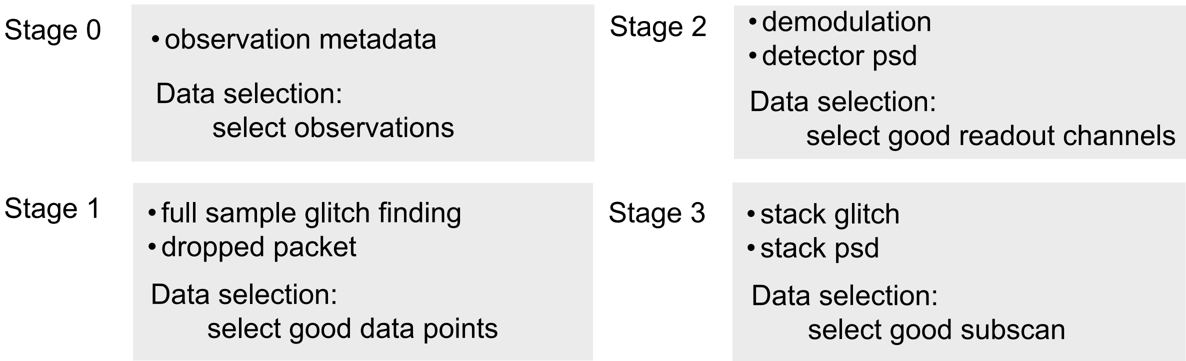

Fig. 5.6 Data selection and characterization procedure

comparing the stimulator measurement right before and after each observation. The stimulator signal is modulated by the chopper from 4 Hz to 44 by by 8 Hz step. From the frequency dependence of the amplitude of the stimulator, the gain and time constant of each detector is determined.

5.4 Data selection

This section describes the data selection and characterization procedures. The data characterization and selection can be divided into four stages (Fig. 5.6). The data selection criteria are similar to those used for CMB analysis [151, 153], except for the several optimizations of selection conditions. The data volume is summarized in Table 5.1. Observation efficiency is low because the primary science target of POLARBEAR is the CMB, not Tau A. Since POLARBEAR has a 2.4° field of view, the Tau A signal is contained in less than 1% of the entire data. The remaining data outside of 12′ diameter around Tau A are used for evaluating the data quality.

First, we select observations from observing conditions.

- average(PWV) < 4 mm: Drop the observation with bad weather conditions.
- PWV drift, max(PWV) - min(PWV) < 1 mm: Drop observations with drastic change of weather conditions (Fig. 5.7).
- Focal plane temperature in [260 mK, 279 mK]: Drop observation when focal plane temperature was not regulated in typical range (Fig. 5.7).
- Sun & Moon distance < 30 degrees: Drop observations which can have sidelobe contaminations from Sun & Moon (Fig. 5.8).
- Instrumental problems: Drop observations when there are known instrumental problems.

After the observation selection, the number of observations is reduced from 220 to 95.

Second, we cut the time domain glitches to the pre-demodulated full-sampled timestreams. We convolved the TOD with the kernel which are designed to pick up the sharp spikes in while nulling the HWP synchronous structures at multiples of 2Hz [151]. We dropped the subscans where the maximum deviation of convolved TOD is larger than 10σ. After dropping time domain glitches, we subtract the first to the seventh multiple of the HWP synchronous structure from the TOD. The gaps and glitches in time domain are masked. The HWP angle is reconstructed from the angle encoder using the method of POLARBEAR Collaboration [153]. After the subtraction of the HWP synchronous structure, the

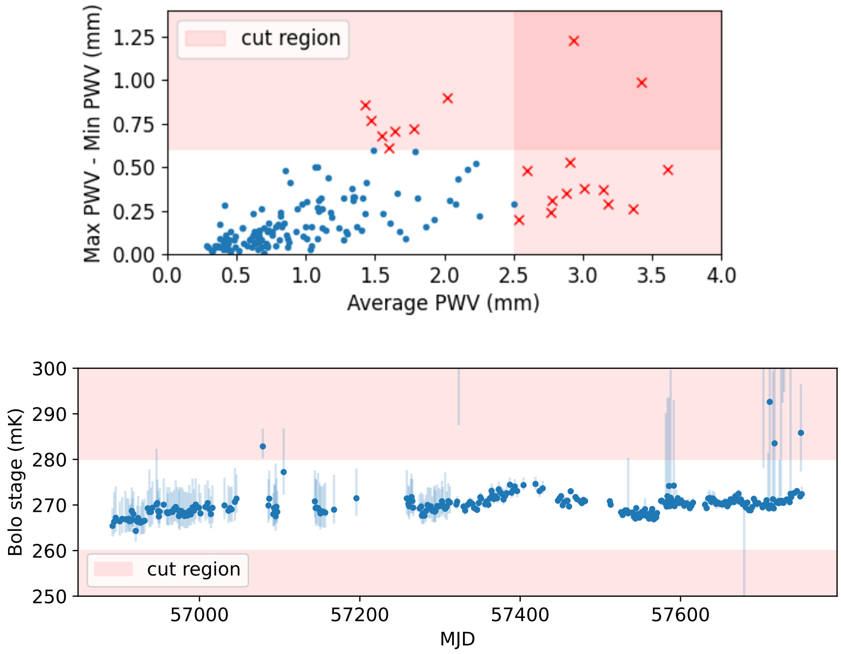

Fig. 5.7 Observation selection conditions. The red shaded regions are dropped from analysis. Top panel shows the PWV cut, and bottom shows the cut based on the focal plane temperature.

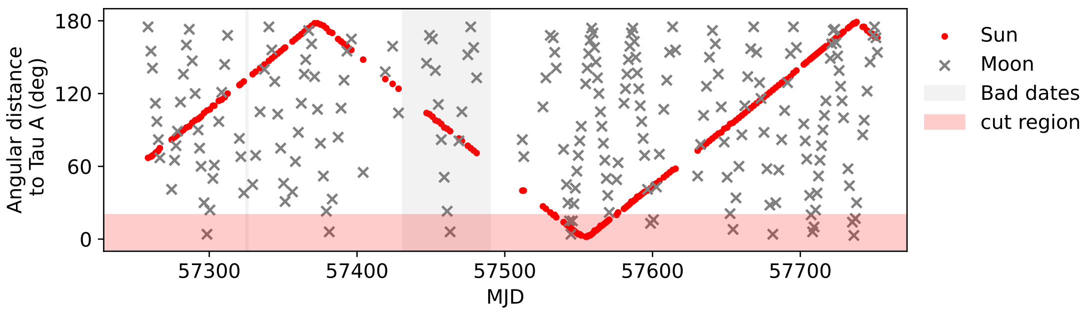

Fig. 5.8 Sun and Moon distance cut. Observations with an average distance of less than 30 degrees between Tau A and the Sun or Moon are dropped to mitigate sidelobe contamination.

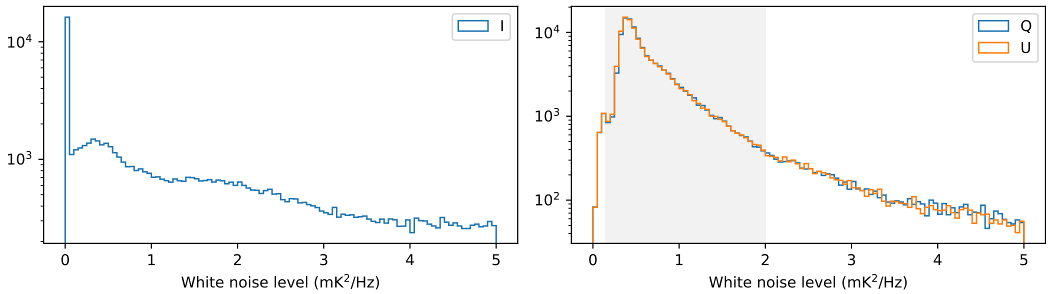

Fig. 5.9 Histogram of the white noise levels of individual detectors.

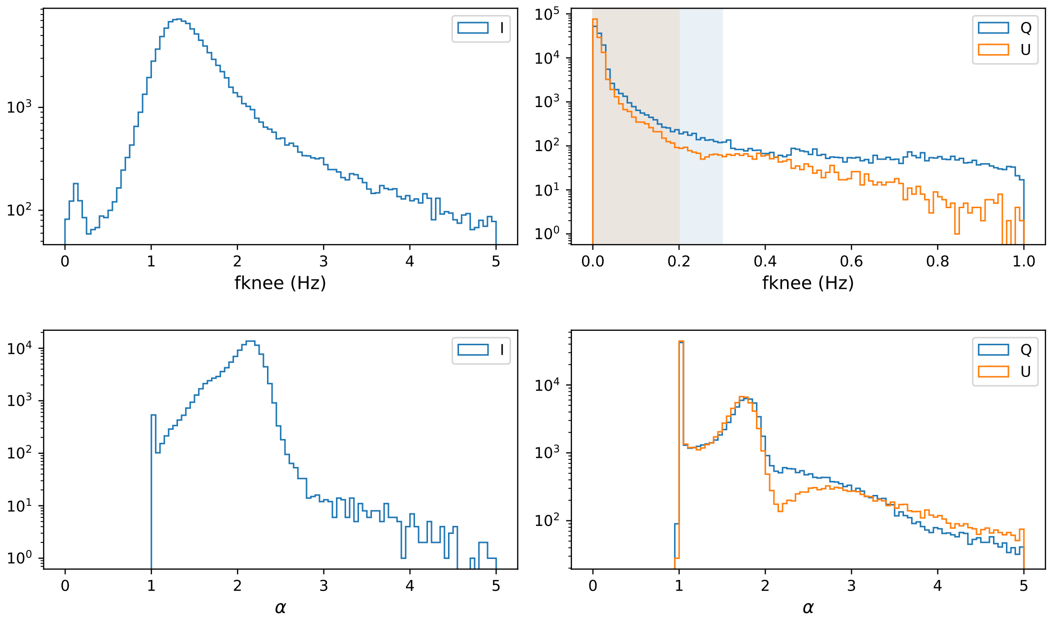

Fig. 5.10 Histogram of the knee frequencies and indexes of individual detectors.

polarization signal is reconstructed by demodulation [99, 184]. We multiply the TOD by the complex conjugate of the modulation function and apply low-pass filtering and down-sampled to 16 Hz.

Third, we perform the selection of detectors analysis according to the detector calibration and the individual noise characteristics. The detectors which do not have, relative pointing calibration, polarization calibration, gain calibration or time constant calibration are dropped. The individual noise characteristics of detectors in the frequency domain is simply modeled as the sum of $(f/f_{\text{knee}})^{-\alpha}$ component and white noise, separately for intensity (I) and polarizations (Q and U) as shown in Figs. 5.9 and 5.10. The detectors with white noise level larger than 2 mHz $\sqrt{s}$ or with anomolously small white noise (smaller than 150 μHz $\sqrt{s}$) are dropped. Also, the observations with less than 100 detectors after detector selection are dropped.

Table 5.1 Data volume

Observation	
from	2015 Aug 25
until	2016 Dec 20
Total calender time	11616 hr
Time observing patch	243 hr
Observation efficiency	2.1 %
Total detector	1274
With Calibration	647
Detector Yield	50.8%
Total volume of data	156,998 hr
Final volume of data	47,210 hr
Data selection efficiency	30.1%
Overall efficiency	0.63%

Table 5.2 Data selection efficiency

Stage of data selection	
Terminated/stuck observation	98.1%
Detector stage temperature	92.9%
Weather condition	84.5%
Sun Moon distance	78.7%
Instrumental problem	88.4%
Off detector	79.4%
Packet drop	98.3%
Individual detector glitch	99.6%
Common mode glitch	89.8%
Individual detector PSD	85.9%
Common mode PSD	94.5%
Cumulative data selection	30.1%

Finally, after selecting the good detectors, the selected TODs are coadded by inverse noise weight to construct common mode timestream.

$$\text{stacked I} = \frac{\sum_i I_i(t) \times w_{0,i} \times \text{mask}_i(t)}{\sum_i w_{0,i} \times \text{mask}_i(t)} \tag{5.5}$$

$$\text{stacked Q} = \frac{\sum_i Q_i(t) \times w_{4,i} \times \text{mask}_i(t)}{\sum_i w_{4,i} \times \text{mask}_i(t)} \tag{5.6}$$

$$\text{stacked U} = \frac{\sum_i U_i(t) \times w_{4,i} \times \text{mask}_i(t)}{\sum_i w_{4,i} \times \text{mask}_i(t)} \tag{5.7}$$

While the white noise of each detector are not correlated, the low frequency noise, $1/f^{\alpha}$ component, is correlated. Therefore, the low-frequency noise is better characterized by common mode timestream. The observation with common mode knee frequency in Q (U) in telescope frame larger then 300 mHz (200 mHz) or anomolously large white noise are dropped [1] (Fig. 5.11) Also, the subscans which have significant glitches in common mode timestreams are dropped to mitigate the contamination from cloud signal, which is correlated and localized in time domain [184].

Table 5.2 shows the efficiency of data selection in each selection criteria.

5.5 Time domain processing and demodulation

This section provides a brief review of the processing of the time-ordered data (TOD), measured by the transition-edge sensors (TESs) in the POLARBEAR receiver [11]. Each TES bolometer is coupled to a dipole-slot antenna and measures a single polarization of the incident light. The POLARBEAR employs HWP at the prime focus which continuously rotates at 2 Hz. Thus, the idealistic modulated timesteams of the detector is expressed as follows [186].

$$d_m(t) = I(t) + \text{Re}[(Q(t) + iU(t))m(\chi)], \tag{5.8}$$

[1] The selection condition of common mode noise is relaxed compared to the CMB analysis [151], 150 mHz (100 mHz). This is because of the results of the evaluation of systematic errors, which will be discussed later, and because the signal to ratio for Tau A is higher than that for CMB.

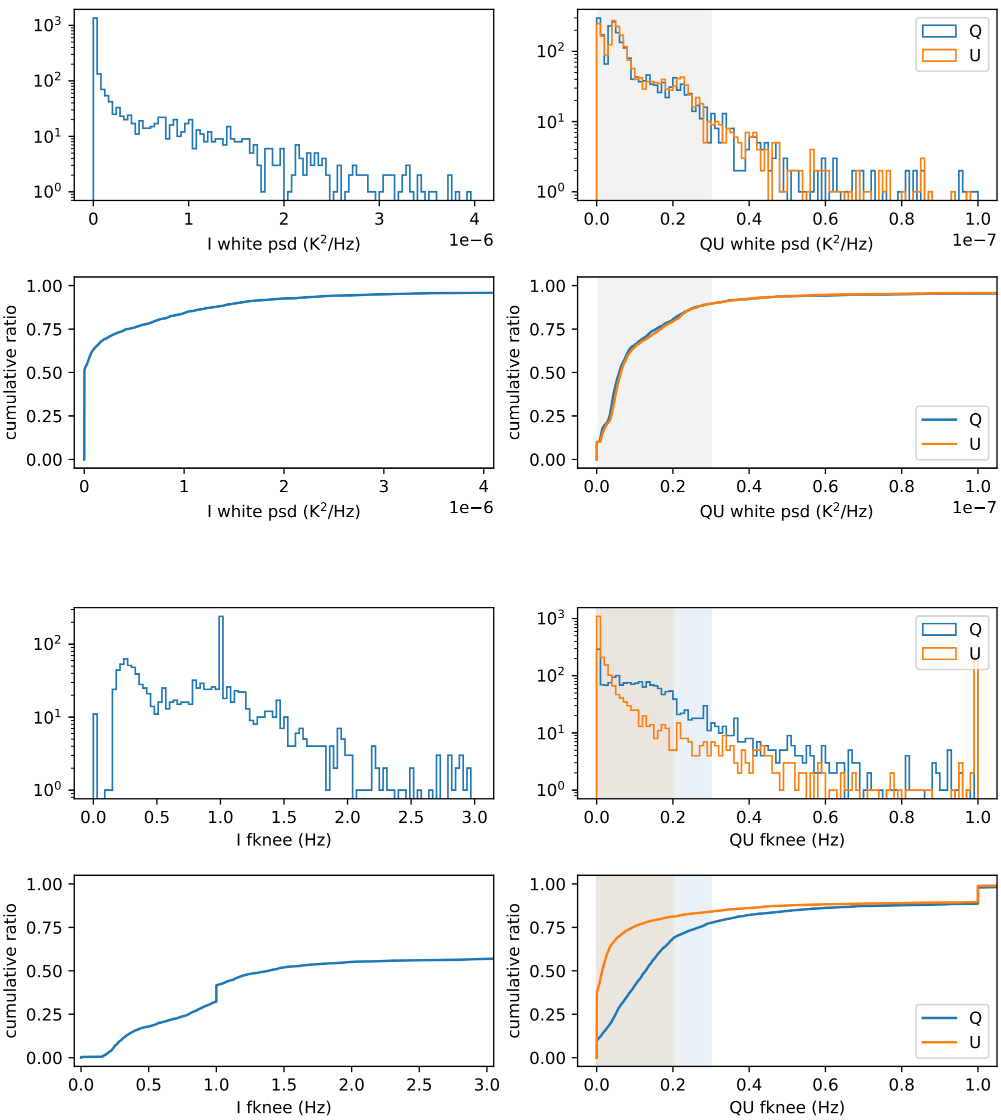

Fig. 5.11 Histogram of the white noise levels and knee frequencies of common mode timestreams.

where $I(t)$, $Q(t)$ and $U(t)$ are the incident stokes parameters defined in the telescope coordinate, $\chi(t)$ is the rotation angle of the HWP, and

$$m(\chi) = \exp(-i4\chi) \tag{5.9}$$

is the modulation function. We obtain the intensity signal $d_0(t) = I(t)$ by applying a low-pass filter, and also we demodulate the timestreams and extract the polarization signal as a demodulated timestreams $d_d(t) = Q(t) + iU(t)$. In the presence of the static instrumental polarization (A_4), the mis-estimation of the HWP angle ($\Delta\chi$), the detector angle ($\theta_{\rm det}$), the intensity to polarization (I2P) leakage coefficient (λ_4), the time constant of detector (τ), and the timing uncertainty (Δt) the modulated timestreams is modified as

$$d_m(t) = I(t) + \mathrm{Re}[(A_4 + \lambda_4 \Delta I(t) + d_d^{\rm ideal})m'(\chi)], \tag{5.10}$$

where $\Delta I(t)$ is the drift of the intensity signal, and the modified modulation function $m'(\chi)$ is

$$\begin{aligned} m'(\chi) &= \exp\left(-i4\chi(t-\tau-\Delta t) + i4\Delta\chi + i2\theta_{\rm det}\right) \\ &\simeq \exp\left(-i4\chi(t) + i4\dot{\chi}\tau + i4\dot{\chi}\Delta t + i4\Delta\chi + i2\theta_{\rm det}\right). \end{aligned} \tag{5.11}$$

Therefore, the demodulated timestreams are modifies as

$$d_d(t) \simeq (A_4 + \lambda_4 \Delta I(t) + d_d^{\rm ideal}) e^{i4\dot{\chi}\tau + i4\dot{\chi}\Delta t + i4\Delta\chi + i2\theta_{\rm det}}. \tag{5.12}$$

Note that A_4 and λ_4 are complex values, and others are real values. A_4, $\Delta\chi$ and Δt are common to all detectors, while $\theta_{\rm det}$, λ_4 and τ are different. Also, $\arg(A_4)$ and $\theta_{\rm det}$ are assumed to be stable throughout all the observations, while others are not. The effects of time constant τ and detector angle $\theta_{\rm det}$ are deconvolved, I2P leakage effect is subtracted, in time domain.

$$d_d(t) \simeq (A_4 + \Delta\lambda_4 \Delta I(t) + d_d^{\rm ideal}) e^{i4\dot{\chi}\Delta\tau + i4\dot{\chi}\Delta t + i4\Delta\chi + i2\Delta\theta_{\rm det}}, \tag{5.13}$$

where $\Delta\tau$, $\Delta\theta_{\rm det}$ and $\Delta\lambda_4$ are the mis-estimation of τ, $\theta_{\rm det}$ and λ_4, respectively. The argument of complex phase of Eq. 5.13 corresponds to mis-estimation of polarization angle in telescope coordinate, therefore the corresponding mis-estimation of the polarization angle of Tau A is expressed as

$$\Delta\psi = 2\left(\Delta\chi + \dot{\chi}\Delta t + \dot{\chi}\Delta\tau\right) + \Delta\theta_{\rm det}. \tag{5.14}$$

Also, the mis-estimation of the I2P leakage coefficient $\Delta\lambda_4$ biases the Tau A polarization angle as

$$\psi + \Delta\psi = \frac{1}{2}\tan^{-1}\left(\frac{U_{\rm Tau\ A} + \Delta\lambda_4^{\rm imag} I_{\rm Tau\ A}}{Q_{\rm Tau\ A} + \Delta\lambda_4^{\rm real} I_{\rm Tau\ A}}\right), \tag{5.15}$$

where $Q_{\rm Tau\ A}$, $U_{\rm Tau\ A}$ and $I_{\rm Tau\ A}$ are the Stokes parameters of the incident light from Tau A. This bias is approximately expressed as

$$\Delta\psi \lesssim \frac{1}{2}\frac{|\Delta\lambda_4|}{|p_{\rm frac}|}, \tag{5.16}$$

where p_{frac} is a complex polarization fraction of Tau A as $p_{\mathrm{frac}} I_{\mathrm{Tau\ A}} = Q_{\mathrm{Tau\ A}} + iU_{\mathrm{Tau\ A}}$. Each of these calibrations and imperfections are characterized as we describe in the following section.

5.6 Calibration

This section highlights the improved polarization angle calibration methods in this study. The calibration of the pointing model of the telescope, the pointing offsets of detectors, the effective beam function, relative gain variations, detector time constants, and polarization efficiencies are the same as those in [151].

5.6.1 Relative polarization of detector angle

The relative polarization detector angle is calibrated by average of Tau A polarization angle for each detector, in the same way as [151], with the above mentioned improvement of the I2P evaluation and the relative calibration using the instrumental polarization. The relative calibration of the detector angle is performed iteratively until it converges, typically two times, as the I2P subtraction and the instrumental polarization calibration are updated in each iteration. The uncertainty of the detector angle is estimated to be 0.1° by the variation of the Tau A angle measured by each detector averaged over all observations, which is negligibly small as we discuss in Sec 5.11.8.

5.6.2 Intensity to polarization leakage

The estimation of the intensity to polarization leakage (I2P) is updated from POLARBEAR Collaboration [151]. To validate the I2P estimates, two different I2P estimates were performed on Jupiter observations and the results were compared. There are two sources of I2P, one is a leakage due to the imperfection of optical components and the other is due to the nonlinearity of the detectors [186]. The I2P estimated by two different methods includes both effects.

The first method closely follows the method used in [151], originally developed by [186]. We take the correlation between the one-hour intensity timestream and one-hour polarization timestream and obtain the I2P leakage coefficient λ_4, assuming that the intensity timestream is dominated by the signal of unpolarized atmospheric fluctuation, and the fluctuation of the polarization timestream is dominated by the intensity timestream leaked into polarization by the I2P leakage effect. Tau A signal is masked out from the timesteam so that the Tau A signal does not bias the estimation of λ_4.

The second method uses Jupiter signal. The I2P can be decomposed into monopole, dipole quadruople terms [48]. We measure monopole term by integrating the map around Jupiter within 12′ diameter as

$$\lambda_4^{\mathrm{real}} = \frac{\sum_p^{\varnothing<12'} Q_p^{\mathrm{Jupiter}}}{\sum_p^{\varnothing<12'} I_p^{\mathrm{Jupiter}}} \tag{5.17}$$

$$\lambda_4^{\mathrm{imag}} = \frac{\sum_p^{\varnothing<12'} U_p^{\mathrm{Jupiter}}}{\sum_p^{\varnothing<12'} I_p^{\mathrm{Jupiter}}}, \tag{5.18}$$

where I_p, Q_p and U_p are the p-th I, Q and U map pixel. The contamination from higher order multipoles is found to be small [186]. Here we assumed that the polarization of Jupiter is purely from I2P from our

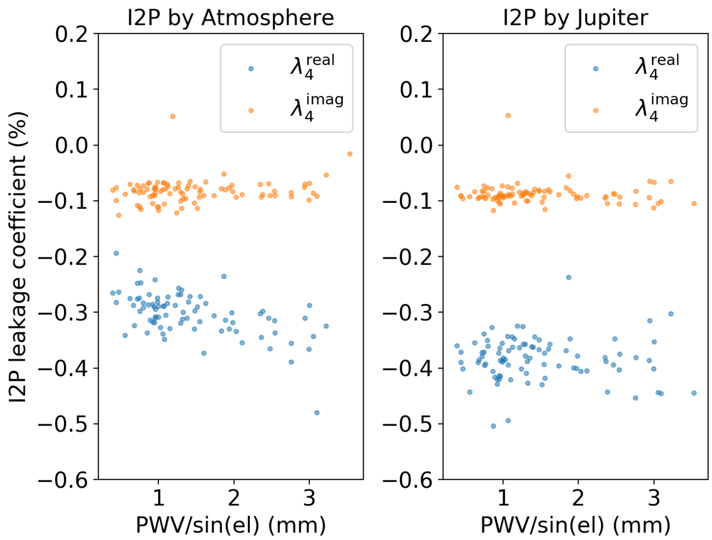

Fig. 5.12 Comparison of the PWV dependence of the two intensity to polarization coefficient. Each point is a median of all detectors for one observation. The PWV is scaled by sin(el) to compare the line of sight integrated value.

instruments. Jupiter is slightly polarized by synchrotron radiation [139, 140], and its polarization at 150 GHz is less than 0.1% [100].

Figure 5.12 shows the comparison of the observation-by-observation I2P by the two methods. The I2P of method 1 shows larger PWV dependence than the method 2, and the I2P values at larger PWV show closer values to that of method 2. We attribute the PWV dependence of method 1 to bias, based on the verification of the systematic errors discussed in Sec 5.9.4.

The I2P estimates by method 1 may be biased, because at lower PWV, the $1/f$ fluctuation from non-optical effects, such as the fluctuation of the focal plane temperature or the temperature of the primary or secondary mirror, the warm readout electronics may not be negligible [187][2]. On the other hand, method 2 is robust to any $1/f$ fluctuations because it is estimated by the point source, Jupiter. However, method 2 also has its drawbacks, such as the fact that they are observed under different observing conditions and that Jupiter is about 10 times brighter ($T_{\mathrm{Jupiter}} \sim$2 K) than Tau A, so it may be more affected by the detector non-linearities and have constant bias.[3]

Therefore, instead of adopting the value of method 2, we subtracted the PWV dependence from method 1 by modeling the PWV dependence as a linear function for each detector and substituting the median PWV to construct the estimate of I2P using Tau A observation timestreams, taking the advantage that the method 1 can be applied to Tau A observation data. We call this method as method 1′.

In this study, we construct the I2P leakage model by making a modification to method 1 and applying it to the Tau A observations. We model the PWV dependence of method 1 as a linear function for each detector and substitute the median PWV (=0.7 mm) of Tau A observations, to make representative λ_4 for each detector. We call this method 1′. Figure 5.13 shows the comparison of detector-by-detector I2P coefficient λ_4 by method 1′ and method 2. They show reasonable agreement. We discuss the uncertainty of I2P leakage estimates by the difference of method 1′ and 2 in Sec. 5.11.

[2]The non-optical $1/f$ fluctuation can be larger in the Tau A or Jupiter scans than in the CES scans [151], because it tracks the sources by changing elevation.

[3]Jupiter is also used for the beam characterization and is known to be not too bright to saturate the POLARBEAR detectors.

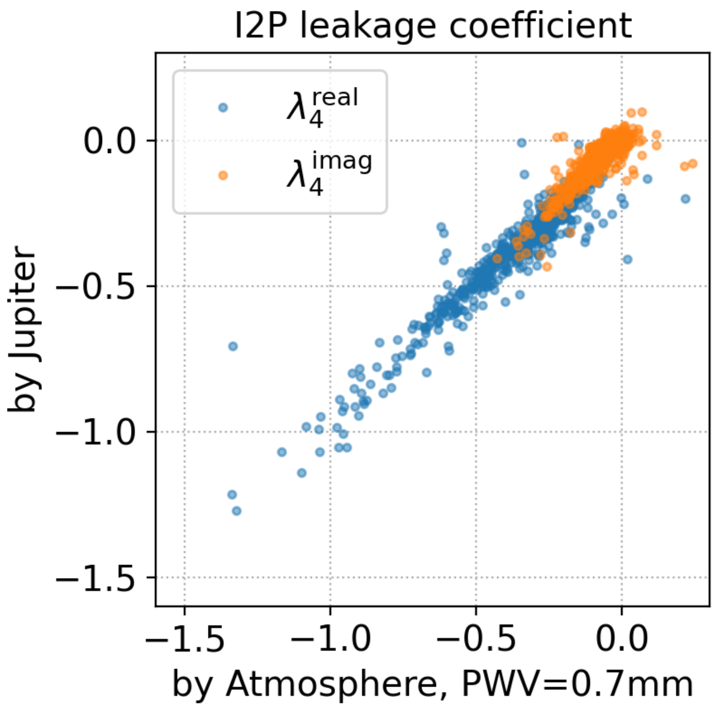

Fig. 5.13 Comparison of the each detector's intensity to polarization coefficient estimated by $1/f$ and Jupiter.

5.6.3 Relative polarization angle between observations

As we showed in Eq. 5.14, the observation-by-observation mis-calibration of the polarization angle is caused by the mis-estimation of HWP angle ($\Delta\chi$), the timing offset (Δt), and the mis-calibration of the detectors' time constant ($\Delta\tau$). In Polarbear Collaboration [151], we calibrated the time constant of each detector for each observation by the average of the thermal source calibration right before and after the Tau A observations, and the achieved accuracy of angle calibration was negligibly small.

In the search for polarization oscillation, the importance of observation-by-observation relative calibration increases compared to the analysis which takes an average of all observations, e.g. CMB power spectrum analysis. In this study, we further calibrate the relative polarization angle between observations assuming that the polarization angle of the instrumental polarization due to the primary mirror ($\frac{1}{2}\arg(A_4)$) is stable[4]. Since our telescope employs ambient temperature continuously rotating half-wave plate (HWP) polarization modulator at the prime focus between the primary mirror and secondary mirror [186], the instrumental polarization by the reflection at the primary mirror [19] produces the instrumental polarization. This instrumental polarization is a good calibrator for the relative angle between observations, because it illuminates all detectors stably and uniformly ($|A_4| \sim 0.1$ K) [186].

The instrumental polarization is estimated as a signal synchronous to the 4th harmonic of the rotation angle of the HWP, by averaging the modulated timestreams (Eq. 5.10) over the HWP angle for each observation [186], masking Tau A signal and glitches in the time domain. The variation of the instrumental polarization angle ($\frac{1}{2}\arg(A_4)$) between observations was found to be 0.16° root mean

[4]The instrumental polarization is not modulated by the ALP, because the distance between the primary mirror and the detectors (~1 m) is much shorter than the coherence length of local ALP field in the mass scale of our interests ($\sim 10^{15} - 10^{18}$ m)

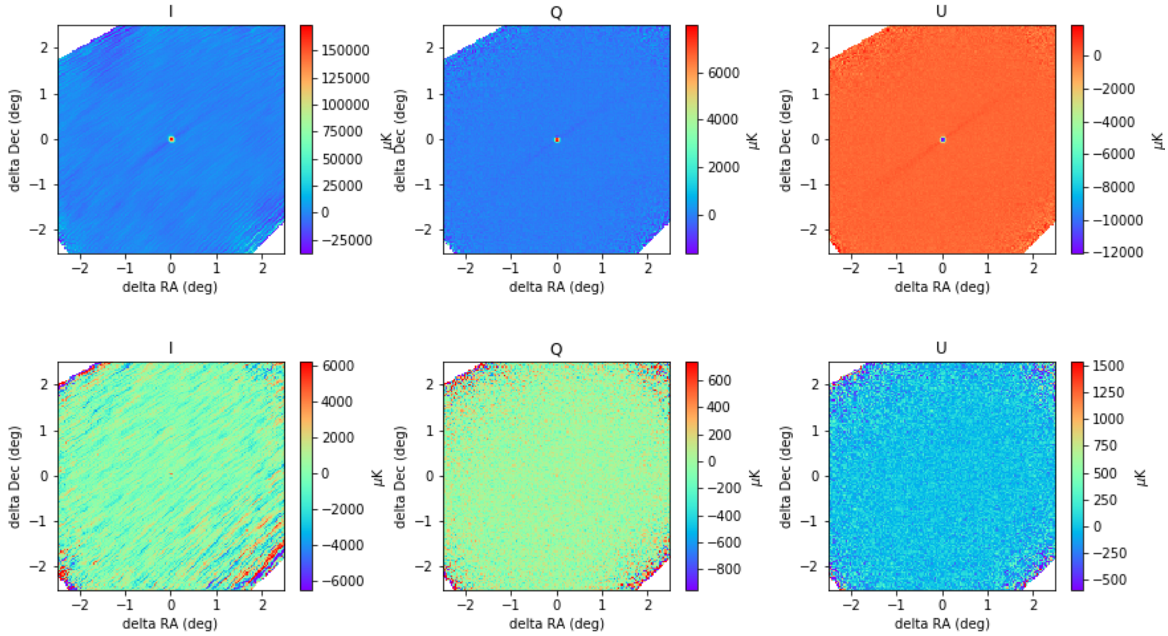

Fig. 5.14 Top: Example of Coadd map. Bottom: Example of signflip map.

square (RMS), while the median of statistical uncertainty per observations is 0.02° in standard deviation (STD).

5.7 Estimation of Tau A polarization angle and its statistical uncertainty

Polarization angle of Tau A (ψ) is estimated in map-domain, with the same filtered binned map-making as POLARBEAR Collaboration [151]. ψ is estimated by integrating over the map around Tau A within 12′ diameter as

$$d_t = \frac{1}{2}\tan^{-1}\left(\frac{\sum_p^{\varnothing<12'} U_p^{\text{Tau A}}}{\sum_p^{\varnothing<12'} Q_p^{\text{Tau A}}}\right), \tag{5.19}$$

where d_t is the measured ψ, and t is the average observation time over one hour. The diameter of the integration region is chosen so that the region covers the size of Tau A convolved by our beam size (FHWM 3.6′) including the measured boresight pointing drift of our telescope. This angle estimation method is not the most efficient method, but it is immune to the complexity of the structure of Tau A, and robust to systematic effects.

The statistical uncertainty in each observation σ_t was estimated by the bootstrap method, also called "signflip noise estimation", which is widely used for noise estimation in the CMB analysis. First, we simulate the noise only map for each observation by randomly assigning a +1 or -1 factor to each detector and coadding individual detector map (Fig. 5.14). The random sign is assigned so that the total data weight is even for both signs. The signflip map will cancel the Tau A signal as well as the $1/f$ noise

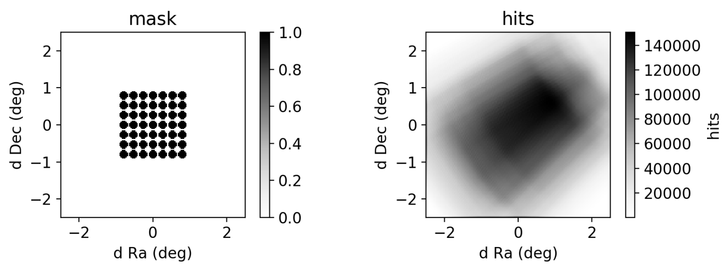

Fig. 5.15 The map regions used for signal extraction and noise sampling. The center region was used for signal extraction and all the other 48 regions are used for noise sampling.

which is common among all the detectors. Therefore, the signflip noise simulation by detectors is a data-driven estimation of statistical error[5].

Then, we sample the noise realizations of Stokes parameters of Q and U from signflip map over the 48 regions with the same size as the one used to estimate ψ as $\delta Q = \sum_p^{\text{noise region}} Q_p^{\text{Noise}}$, $\delta U = \sum_p^{\text{noise region}} U_p^{\text{Noise}}$. The statistical noise of polarization angle is sampled by integrating the signflip noise map over the same size of region used to extract the signal as follows. The 48 regions around Tau A were used for noise samples per noise simulation map as shown in Fig. 5.15. One of the statistical noise realizations of Tau A polarization angle $\delta\psi$ is obtained by adding δQ and δU to the Tau A signal as

$$\psi + \delta\psi = \frac{1}{2}\tan^{-1}\left(\frac{\sum_p^{\varnothing<12'} U_p^{\text{Tau A}} + \delta U}{\sum_p^{\varnothing<12'} Q_p^{\text{Tau A}} + \delta Q}\right). \tag{5.20}$$

We simulated 30 signflip noise maps and obtained 1440 angle noise samples for for each observation. Figure 5.16 shows the histogram of the obtained noise realizations.

5.8 Estimation of Tau A angle spectrum

As described in Sec. 5.3, the Tau A observations spans over 486 days, and performed very daily. Therefore, the Nyquist frequency ($f_{\text{NYQ}} = 1/(2\Delta T)$) is well-defined in our data set. Because of the aliasing, the frequency bins above f_{NYQ} is strongly correlated with the frequency bins below f_{NYQ}, and almost all degrees of freedom in our data are contained in the following set of 242 bins:

$$f_{\text{bins}} = \left\{\frac{1}{486\Delta T}, \frac{2}{486\Delta T}, ..., \frac{242}{486\Delta T}\right\} \tag{5.21}$$

where $\Delta T = 0.997$ day $\simeq$ (1-1/366). The harmonics of $f_{\text{NYQ}}(= 1/(2\Delta T))$ is not included, because the harmonics of f_{NYQ} correspond to the constant mode and we do not have sensitivity to them. Over the 486 days of observation period, we have 95 observation of Tau A. Therefore, the number of frequency bins (=242) is much larger than the effective number of freedom (=95). This induces a bin-by-bin correlation among the frequency bins. Accepting the bin-by-bin correlations, the scientific result will be extendend to

$$f_{\text{bins,result}} = \left\{\frac{N}{2\Delta T} + f_{\text{bins}}\middle| N = 0, 1, ..., 31\right\} \tag{5.22}$$

[5]The same signflip pattern is used for all the data-test splits to ensure the correlations between the splits are accounted correctly.

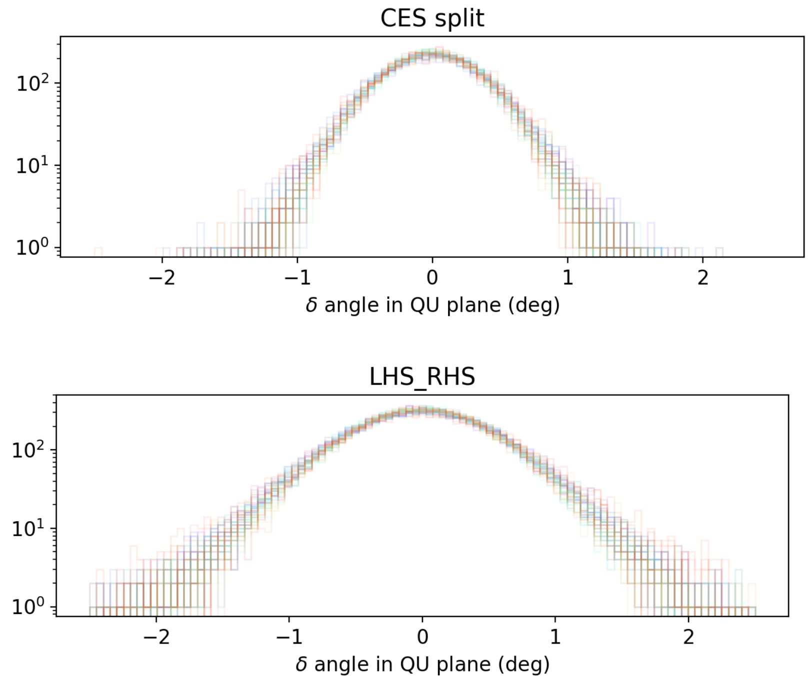

Fig. 5.16 Histogram of the simulated polarization angle noise of observation-splits and one of the bolo-splits. Noise sampled from different regions are superposed with different colors. Good agreement among different noise sample regions is seen.

The maximum frequency is determined by the averaging over the time period of single Tau A observation, 1 hour (Eq. C.4).

We estimate the frequency spectrum by least-square spectral analysis [195]. Hereafter we call the amplitude of least-square spectral analysis as LSSA. The LSSA of the measured Tau A angle d_t with the error bar σ_t is

$$\tilde{d}_f = \underset{A}{\operatorname{argmax}}\left[\exp\left\{-\frac{1}{2}\sum_t\left(\frac{d_t - \mathrm{Re}(Ae^{-i2\pi ft})}{\sigma_t}\right)^2\right\}\right] \tag{5.23}$$

The equivalent LSSA is obtained by a linear sum of d_t as

$$\begin{pmatrix}\tilde{d}_f^{\mathrm{real}}\\ \tilde{d}_f^{\mathrm{imag}}\end{pmatrix} = \begin{pmatrix}\sum_{t'} c_{t'}^2\sigma_{t'}^{-2} & \sum_{t'} c_{t'}s_{t'}\sigma_{t'}^{-2}\\ \sum_{t'} c_{t'}s_{t'}\sigma_{t'}^{-2} & \sum_{t'} s_{t'}^2\sigma_{t'}^{-2}\end{pmatrix}^{-1}\begin{pmatrix}\sum_t c_t d_t\sigma_t^{-2}\\ \sum_t s_t d_t\sigma_t^{-2}\end{pmatrix}, \tag{5.24}$$

where $c_t = \cos(2\pi ft), s_t = \sin(2\pi ft)$. Hereafter, we express the complex amplitude of the LSSA as

$$\tilde{d}_f \equiv \tilde{d}_f^{\mathrm{real}} + i\tilde{d}_f^{\mathrm{imag}} = \sum_t F_{ft}d_t, \tag{5.25}$$

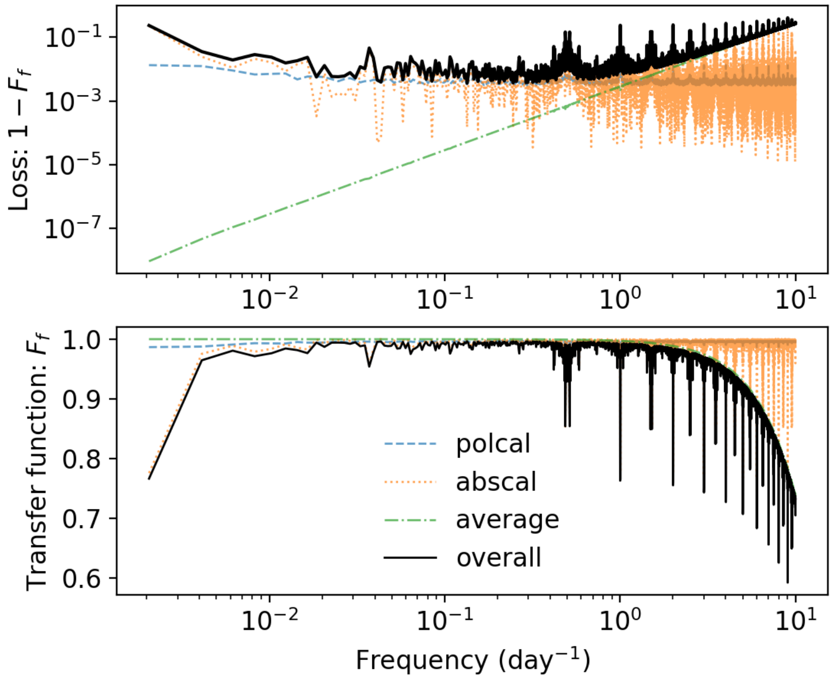

Fig. 5.17 Overall transfer function and individual transfer functions over the frequency bins (Eq. 5.22). The transfer function is averaged over all the phases of oscillations. Bottom panel shows the Transfer function F_f, the top panel shows $1 - F_f$. The calibration of relative polarization angle between detectors using Tau A has the effect of reducing the signal almost uniformly to 99.5% (polcal). The absolute polarization angle (ψ_0) calibration has the effect of reducing the signal at certain frequencies that our observing schedule does not favor (abscal). The averaging over one-hour observation time has the effet of reducing the signal at high frequencies (average).

where

$$F_{ft} = \begin{pmatrix} 1 \\ i \end{pmatrix}^{\mathrm{T}} \begin{pmatrix} \sum_{t'} c_{t'}^2 \sigma_{t'}^{-2} & \sum_{t'} c_{t'} s_{t'} \sigma_{t'}^{-2} \\ \sum_{t'} c_{t'} s_{t'} \sigma_{t'}^{-2} & \sum_{t'} s_{t'}^2 \sigma_{t'}^{-2} \end{pmatrix}^{-1} \begin{pmatrix} c_t \sigma_t^{-2} \\ s_t \sigma_t^{-2} \end{pmatrix}. \tag{5.26}$$

Similarly, in the following we express the LSSA of ALP oscillation and noise as $\tilde{s}_f = \sum_t F_{ft} s_t$ and $\tilde{n}_f = \sum_t F_{ft} n_t$, respectively. We note that $\tilde{s}_f$ and $\tilde{n}_f$ are defined using the same noise weight, F_{ft}.

LSSA is a biased estimator for signal amplitude for multiple reasons. We quantify the bias on the oscillation amplitude by the transfer function, F_f. Figure 5.17 represents the individual biases and the overall bias. The overall bias is evaluated by simulating the all the biases at once and averaging over the phase of the oscillation. As we discuss in Sec. 5.11, the bias due to the TOD filtering and mapmaking because it is found to be negligibly small.

5.8.1 Estimation of polarization oscillation amplitude

We search for a single mode polarization oscillation without knowing its frequency and phase. Therefore, we take the convolution for all possible phases, whose probability density function is flat, and estimate the amplitude A_f^{obs} assuming the presence of a signal at each frequency. We maximize the following likelihood function:

$$P(\tilde{d}_f|A_f) = \int_0^{2\pi} d\theta_f \, P(\tilde{d}_f|A_f,\theta_f)P(\theta_f), \tag{5.27}$$

where A_f and θ_f the real-valued true amplitude and phase of the oscillation signal at f, and $P(\theta_f)$ is the uniform probability density.

$$P(\tilde{d}_f|A_f,\theta_f) = \frac{\exp\left(-\frac{1}{2}\sum_{m,n\in\{\text{real},\text{imag}\}} \tilde{\delta}^m_f \tilde{N}^{-1}_{f,mn}\tilde{\delta}^n_f\right)}{\sqrt{(2\pi)^2\det(\tilde{N}_f)}} \tag{5.28}$$

is the probability density for obtaining $\tilde{d}_f$ for given signal parameters. $\tilde{\delta}_f$ is the difference of the LSSA of data minus signal

$$\tilde{\delta}_f \equiv \tilde{d}_f - F_f A_f \exp(i\theta_f), \tag{5.29}$$

and $\tilde{N}_f$ is a noise covariance matrix with elements

$$\tilde{N}_f = \begin{pmatrix} \langle|\tilde{n}^{\text{real}}_f|^2\rangle & \langle\tilde{n}^{\text{real}}_f\tilde{n}^{\text{imag}}_f\rangle \\ \langle\tilde{n}^{\text{imag}}_f\tilde{n}^{\text{real}}_f\rangle & \langle|\tilde{n}^{\text{imag}}_f|^2\rangle \end{pmatrix}, \tag{5.30}$$

where $\langle\cdot\rangle$ represents average over signflip noise simulations. Note that when the noise covariance is diagonal, the Eq. 5.27 is simplified as

$$P(\tilde{d}_f|A_f) = \frac{1}{\pi\langle|\tilde{n}_f|^2\rangle} I_0\left(\frac{2A_f|\tilde{d}_f|}{\langle|\tilde{n}_f|^2\rangle}\right)\exp\left(-\frac{|\tilde{d}_f|^2 + F_f^2A_f^2}{\langle|\tilde{n}_f|^2\rangle}\right). \tag{5.31}$$

where I_0 is the modified Bessel function of the first kind. The equivalent likelihood is obtained by considering that $2|\tilde{d}_f|^2/\langle|\tilde{n}_f|^2\rangle$ follows the non-central chi-square distribution with non-centrality of $2F_f^2A_f^2/\langle|\tilde{n}_f|^2\rangle$.

To evaluate the detection significance, we form the following test statistic, which quantifies the global significance of the preference for the signal over the null hypothesis:

$$\Delta\chi^2 = \max_f\left(\Delta\chi^2_f\right), \tag{5.32}$$

where

$$\Delta\chi^2_f = -2\log\left(\frac{P(\tilde{d}_f|A^{\text{best}}_f,\theta^{\text{best}}_f)}{P(\tilde{d}_f|0,0)}\right) = \sum_{m,n\in\{\text{real},\text{imag}\}} \tilde{d}^m_f\tilde{N}^{-1}_{mn}\tilde{d}^n_f$$

is the test statistic for the local significance at each frequency. A^{best}_f and θ^{best} are the parameters that maximize Eq. 5.28.

5.8.2 Estimation of ALP-photon coupling, g

We assume the stochastic ALP field (Eq. 5.2) to estimate the ALP-photon coupling, $g_{a\gamma\gamma}$. We consider the estimator for the square of the ALP photon coupling $g^2_{a\gamma\gamma}$ as

$$\hat{g}^2_{a\gamma\gamma} = \frac{|\tilde{d}_f|^2 - \langle|\tilde{n}_f|^2\rangle}{F_f^2\phi_{\mathrm{DM}}^2/4}. \tag{5.33}$$

and translate it into $g_{a\gamma\gamma}$. We treat $\hat{g}^2_{a\gamma\gamma}$ as a single parameter and allow it to be negative. The probability density for $\hat{g}^2_{a\gamma\gamma}$ is constructed by Monte Carlo simulations, using the probability density for obtaining $\tilde{d}_f$

$$P(\tilde{d}_f|g_{a\gamma\gamma},\phi_{\mathrm{DM}}) = \frac{\exp\left(-\frac{1}{2}\sum_{m,n\in\{\,\mathrm{real,imag}\,\}}\tilde{d}_f^m\tilde{C}^{-1}_{f,mn}\tilde{d}_f^n\right)}{\sqrt{(2\pi)^2\det(\tilde{C}_f)}}, \tag{5.34}$$

where $\tilde{C}_f$ is a covariance matrix of the noise and signal

$$\tilde{C}_f \equiv \tilde{N}_f + \frac{g^2_{a\gamma\gamma}}{4}F_f^2\tilde{S}_f. \tag{5.35}$$

The signal covariance matrix is

$$\tilde{S}_f \equiv \begin{pmatrix} \phi^2_{\mathrm{DM}}/2 & 0 \\ 0 & \phi^2_{\mathrm{DM}}/2 \end{pmatrix}. \tag{5.36}$$

Note that Eq. 5.34 is obtained by the multivariate Gaussian convolution of the probability density for the local stochastic ALP amplitude

$$P(\tilde{\phi}_f|\phi_{\mathrm{DM}}) = \frac{\exp\left(-\frac{1}{2}\sum_{m,n\in\{\,\mathrm{real,imag}\,\}}\tilde{\phi}_f^m\tilde{S}^{-1}_{f,mn}\tilde{\phi}_f^n\right)}{\sqrt{(2\pi)^2\det(\tilde{S}_f)}} = \frac{1}{\pi\phi^2_{\mathrm{DM}}}\exp\left(-\frac{\phi_c^2+\phi_s^2}{\phi^2_{\mathrm{DM}}}\right), \tag{5.37}$$

and the probability density for obtaining $\tilde{d}_f$ for given signal parameters (Eq. 5.28) substituting the stochastic ALP amplitude $\tilde{\phi}_f$ to $A_f\exp(i\theta_f)$ of Eq. 5.29.

It is immediately shown that $\hat{g}^2_{a\gamma\gamma}$ is an unbiased estimator because the variance of d_f is expressed as follows:

$$\langle|\tilde{d}_f|^2\rangle = \left\langle\left|\frac{g_{a\gamma\gamma}}{2}\tilde{s}_f + \tilde{n}_f\right|^2\right\rangle = \frac{g^2_{a\gamma\gamma}}{4}\langle|\tilde{s}_f|^2\rangle + \langle|\tilde{n}_f|^2\rangle = \frac{g^2_{a\gamma\gamma}}{4}F_f^2\phi^2_{\mathrm{DM}} + \langle|\tilde{n}_f|^2\rangle\,.$$

As discussed in Appendix C.2, the efficiency (variance) of this estimator is comparable to the estimator used in POLARBEAR Collaboration [152].

5.9 Data validation

To validate the data analysis, we test the internal consistency of the data using a blind analysis framework. Hereafter we call this test as a null test. We follow the similar formalism used in POLARBEAR Collaboration [152].

5.9.1 Null test data splits

The data-splits are largely divided into two types of splits. **Bolo-splits**: These splits probe the mis-calibration between detectors or the systematic error in each observation such as the time drift of the detector characteristics over one hour. **Observation-splits**: These splits probe the systematic variations between observations.

Bolo-splits

- **LR_SUBSCAN**. This split probes the systematic difference between the left-going subscans and the right-going subscans.
- **QU_PIXEL**. Pixels are fabricated on wafer in two orientations. This split can detect common systematic error between pixel orientations.
- **TOP_BOTTOM**. This split probes common systematic error between two orthogonal transmission lines. Each pixels has two TES bolometers connected to an orthogonal antennas and a pair of micsrostrip transmission lines. The transmission lines physically cross "top" and "bottom" while being electrically isolated.
- **THS_BHS**. This split probes the drift of detector responsibity, time-constant, and non-linearity effects within one observation. Since the telescope gradually changes elevation as it scans azimuth, this split corresponds to splitting one observation into the first and second halves.
- **LHS_RHS**. This split probes for the failure of turn-around masking or the failure of polynomial filtering due to the glitches around turn-arounds.
- **LEAK_BY_BOLO**. This split probes the contamination from residual intensity to polarization leakage. Splits data into to two sets of detectors with small and large intensity to polarization leakage coefficients.
- **AMP_2F_BY_BOLO**. This split corresponds to splitting the detector at the inner and outer physical locations on the focal plane.
- **AMP_4F_BY_BOLO**. This split probes for the systematic difference between detectors which measure larger instrumental polarization and smaller instrumental polarization.
- **QU_FLOOR_BY_BOLO**. This split probes for the systematic difference between noisy detectors and less noisy detectors.
- **ARG_2F_BY_BOLO, ARG_4F_BY_BOLO**. This split probes for the detector by detector mis-calibration of polarization angle in telescope frame.
- **TAU_BY_BOLO**. This split probes for the systematic difference between fast detectors and slow detectors.

Observation-splits

- **FIRST_SECOND**. This split probes for difference between first half of observations (4th season) and second half (5th season).
- **PWV**. This split probes for problems due to bad weather. Bad weather can cause detectors to saturate or latch. This can also probe mis-calibration of detector non-linearity effects.
- **GAIN_BY_CES**. This split probes for the systematics difference due to the difference of the detector gain.
- **SUN_DIST**. This split probes for contamination from sun scanning moon.
- **MOON_DIST**. This split probes for contamination from side lobe scanning moon.
- **LEAK_BY_CES**. This split probes for the mis-calibration of I2P leakage.
- **AMP_2F_BY_CES, AMP_4F_BY_CES**. This split probes for the systematic differences between observations which measure larger instrumental polarization and smaller instrumental polarization.
- **STACK_Q_FKNEE, STACK_U_FKNEE**. This split probes systematic effects due to residual $1/f$ noise. The residual $1/f$ noise in Q timestream arises from residual I2P leakage from non-linearity of detector responsivity. The residual $1/f$ noise in U timestream arises from residual I2P leakage from non-linearity of detector timeconstant or miscalculation of HWP angle.
- **QU_FLOOR_BY_CES**. This split probes for the systematic difference between noisy observations and less noisy observations.
- **ARG_2F_BY_CES, ARG_4F_BY_CES**. This split probes for the observation-by-observation mis-calibration of polarization angle in telescope frame.
- **PNTG_RA_BY_CES, PNTG_DEC_BY_CES**. This split probes systematic effects due to mis-calibration of boresight pointing.

Figure 5.18 shows the orthogonality of null test data splits. The orthogonality of data splits are calculated using a subscan of each detector for each observation as the smallest unit as follows.

$$\text{orthogonality} = \frac{\sum_{o,\ d,\ s} \mathrm{XNOR}(\mathrm{flag}_0(o,d,s), \mathrm{flag}_1(o,d,s))}{\sum_{o,\ d,\ s} \mathrm{OR1}}, \qquad (5.38)$$
$$o: \text{observations},\ d: \text{detectors},\ s: \text{subscans}$$

All mutual orthogonality of data splits are less than 0.7.

5.9.2 Null statistics

We construct three different types of null statistics. First, we take noise weighted difference as follows.

$$\chi^{\mathrm{DC}}_{\mathrm{null}} = \frac{\sum\limits_{t\,\in\,\mathrm{split0}} d_{t,0}\sigma_{t,0}^{-2}}{\sum\limits_{t\,\in\,\mathrm{split0}} \sigma_{t,0}^{-2}} - \frac{\sum\limits_{t\,\in\,\mathrm{split1}} d_{t,1}\sigma_{t,1}^{-2}}{\sum\limits_{t\,\in\,\mathrm{split1}} \sigma_{t,1}^{-2}}, \qquad (5.39)$$

where $d_{t,k}$ and $\sigma_{t,k}$ are the k-th split data and its error bar. For the data-splits which split the data periodically, we did not use χ_{DC} for null-test because of the risk of unblinding the signal (Table. 5.3).

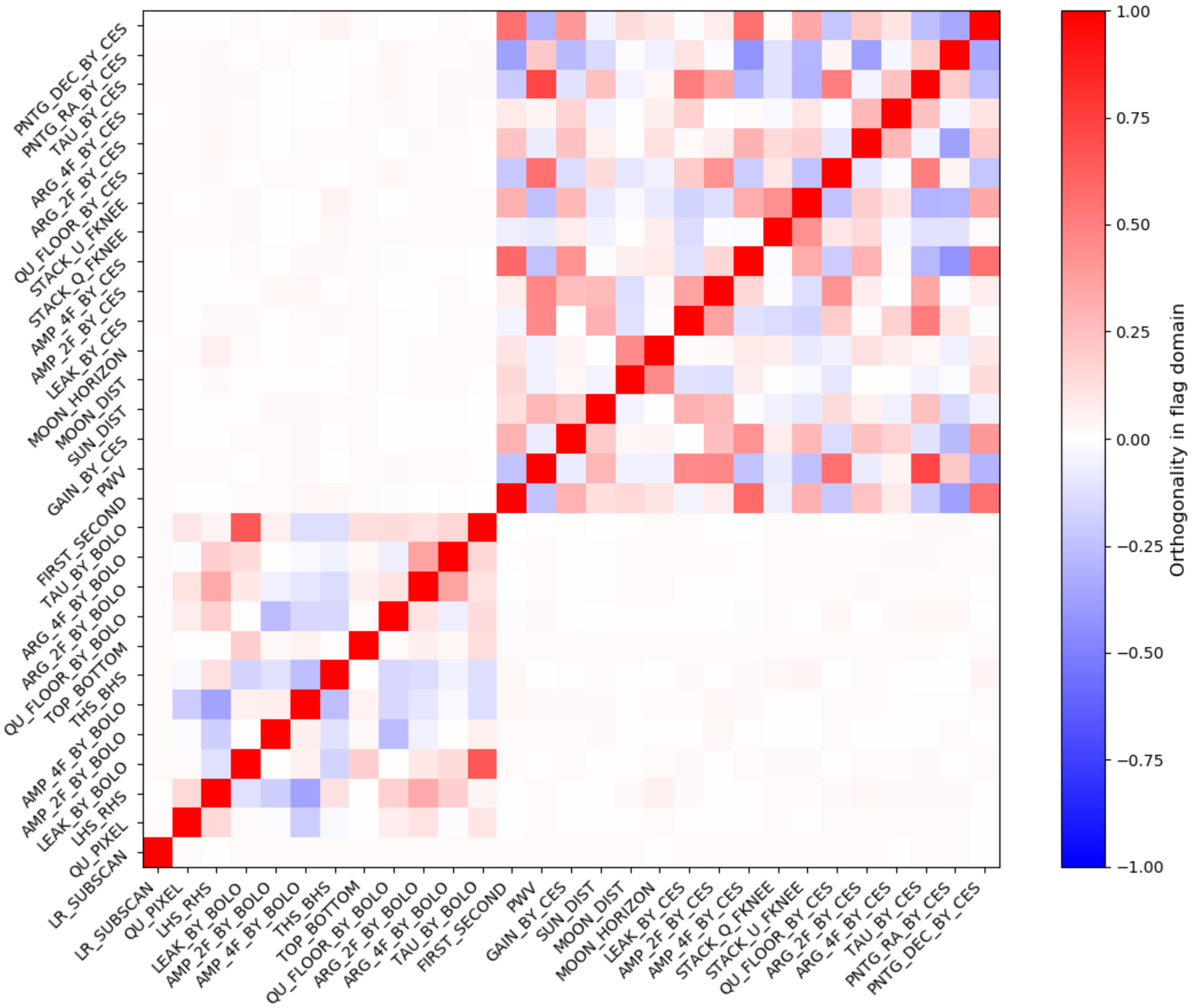

Fig. 5.18 Orthogonality of nullsplits computed in flag domain.

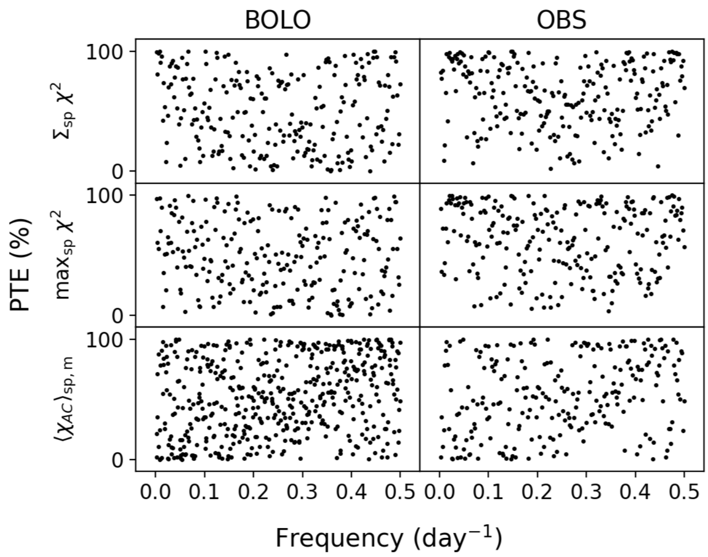

Fig. 5.19 PTEs of null statistics for individual frequency bins. The subscript "sp" denotes "data-splits". Although there are correlations between frequency bins, there is no significant deviation from a uniform distribution.

The other null statistics are constructed in frequency domain, by the difference of LSSAs for each data-split.

$$\chi^{\rm AC}_{\rm null} = (\tilde{d}^m_{f,0} - \tilde{d}^m_{f,1})/\tilde{D}_{mm} \tag{5.40}$$

$$\chi^2_{\rm null} = \sum_{m,n\in\{\,{\rm real},{\rm imag}\,\}} (\tilde{d}^m_{f,0} - \tilde{d}^m_{f,1})\tilde{D}^{-1}_{mn}(\tilde{d}^n_{f,0} - \tilde{d}^n_{f,1}), \tag{5.41}$$

where, $\tilde{d}_{f,j} = \tilde{d}^{\rm real}_{f,j} + i\tilde{d}^{\rm imag}_{f,j}$ is the LSSA of j-th data split (Eq. 5.25), $\tilde{D}_{ij}$ is the covariance matrix of the difference of LSSAs. $\chi_{\rm DC}$ and $\chi_{\rm AC}$ follows the chi-square distribution with one degree of freedom, $\chi^2_{\rm AC}$ follows the chi-square distribution with two degrees of freedom.

As discussed in Sec. 5.8, the null statistics for different frequency bins are correlated. The pattern of correlation differs for the observation-splits, which introduces imperfect signal cancellation in the null statistics for the observation-splits. This is especially problematic when large sinusoidal signals are present, but is sufficiently small in this study since we are verifying the presence of a sinusoidal signal, which is known to be small. For this reason, we do not apply the transfer function (Sec. 5.8) for the construction of null statistics (Eq. 5.41).

5.9.3 Null-test results

Table. 5.3 shows the null-statistics for each data-splits. The null statistics are compared with the 1440 noise only simulations[6] generated using bootstrap method (Sec. 5.7). Then we evaluate the probability to exceed value (PTE) by counting the number of simulation whose null statistics exceeds the real data.

Next, we compute six representative test statistics for bolo-splits and observation-splits separately, to probe the bias and outliers:

[6] 48 samples from each 30 signflip map.

Table 5.3 PTEs of null statistics for individual data-splits

Data split	PTE (%)			
	$\sum_f \chi^2$	$\max_f \chi^2$	$\langle \chi_{\mathrm{AC}} \rangle_{f,m}$	χ_{DC}
Observing conditions				
4th vs. 5th season*	14.2	7.2	31.5	95.3†
High vs. low PWV*	12.6	53.2	64.4	15.8
Sun distance*	11.4	4.2	20.8	15.8†
Moon distance*	13.0	48.0	79.5	15.8†
Left vs. right subscans	50.1	59.4	59.7	67.1
Instrument				
Top vs. bottom bolo	12.0	18.8	76.6	86.7
Q vs. U pixels	61.5	26.0	30.4	56.8
Top half vs. bottom half	11.3	11.8	49.5	34.3
Left half vs. right half	52.6	71.4	16.9	67.1
Data quality				
I2P leakage by obs*	12.2	13.5	5.1	64.8
I2P leakage by bolo	24.0	33.3	65.4	85.5
Common mode Q knee*	11.9	56.5	43.0	48.5
Common mode U knee*	14.4	22.6	18.5	16.5
Common noise by obs*	11.1	8.8	77.1	59.1
Common noise by bolo	98.5	84.7	15.3	46.5
2f amplitude by obs*	11.2	11.7	13.5	10.0
2f amplitude by bolo	30.1	41.2	68.4	39.2
4f amplitude by obs*	11.2	11.7	13.5	37.6
4f amplitude by bolo	30.1	41.2	68.4	39.2
2f angle by obs*	13.3	50.8	1.9	0.6
2f angle by bolo	78.4	57.7	15.2	33.5
4f angle by obs*	12.6	4.8	14.7	27.8
4f angle by bolo	57.3	30.3	14.5	94.7
Gain by obs*	11.2	11.7	13.5	38.1
Tau by bolo	16.5	28.3	57.1	65.8

NOTE: * indicates observation-split type of the data split. χ_{DC} with † were blinded during the data validation process, because these partially unblind oscillation signal at certain frequencies.

Table 5.4 PTEs of representative test statistics used for null test pass criteria.

Type of test	PTE (%)	
	BOLO	OBS
Average χ_{DC} overall	91.46	11.04
Average χ_{AC} overall	52.08	12.78
Extreme χ^2 overall	65.49	12.43
Extreme χ^2 by split	11.74	16.67
Extreme χ^2 by frequency	54.37	16.18
Total χ^2	36.60	14.37
Lowest p-value	40.90	35.42
Highest p-value	34.47	99.68

(1) Average χ_{DC} overall: $\langle \chi_{\mathrm{DC}} \rangle$
(2) Average χ_{AC} overall: $\langle \chi_{\mathrm{AC}} \rangle$
(3) Total chi square: $\sum_{f,\,\mathrm{split}} \chi^2$
(4) Most extreme χ^2: $\max\limits_{\mathrm{split}} \sum_f \chi^2$
(5) Most extreme χ^2 by split: $\max\limits_{f} \sum_{\mathrm{split}} \chi^2$
(6) Most extreme χ^2 by bin: $\max\limits_{f,\,\mathrm{split}} \chi^2$

(1) and (2) probe for the biases, (3)-(5) probe for the outliers specific to the data-splits or frequencies, and (6) probes for the mis-estimation of our uncertainties. The PTEs for the representative statistics are also computed by comparison with the noise simulation (Table. 5.4).

As a pass criteria of the null test, we require the PTE of the lowest PTE value to be larger than 5% to probe the biases and outliers. We require the PTE of lowest PTE to be larger than 5%, this means we choose the lowest PTE of the six statistics and evaluate its PTE again by comparing with the lowest PTEs from the noise simulations. We also require the PTE of highest PTE to be larger than 5% to check the mismatch between the real and estimated uncertainties[7]. The numerical values for these statistics is seen in Table. 5.4. Both bolo-splits and observation-splits pass the criteria.

5.9.4 Correlation with systematic template

In order to detect the possible systematic errors, we additionally checked the significance of the correlation coefficient between the systematic template and the measured Tau A angle[8]. We define the weighted correlation coefficient between data d_t with errorbar σ_t and systematic template T_t as

$$\mathrm{Corr}(d,T) = \frac{\mathrm{Cov}(d,T)}{\sqrt{\mathrm{Cov}(d,d)\,\mathrm{Cov}(T,T)}}, \tag{5.42}$$

[7]The Kolmogorov-Smirnov (KS) test [112] is often used to check the mismatch between the real and estimated uncertainties. However, the KS test is not a strong statistical test for this study because the null statistics of this study are highly correlated, while the KS test assumes independent and identically distributed samples of test statistics.

[8]We consider that the correlation coefficient does not violate the blind policy, because the correlation coefficient is only sensitive to the possible systematic contamination, and is insensitive to the variability of Tau A or the axion-like oscillation, since the systematic template is chosen to contain no signal.

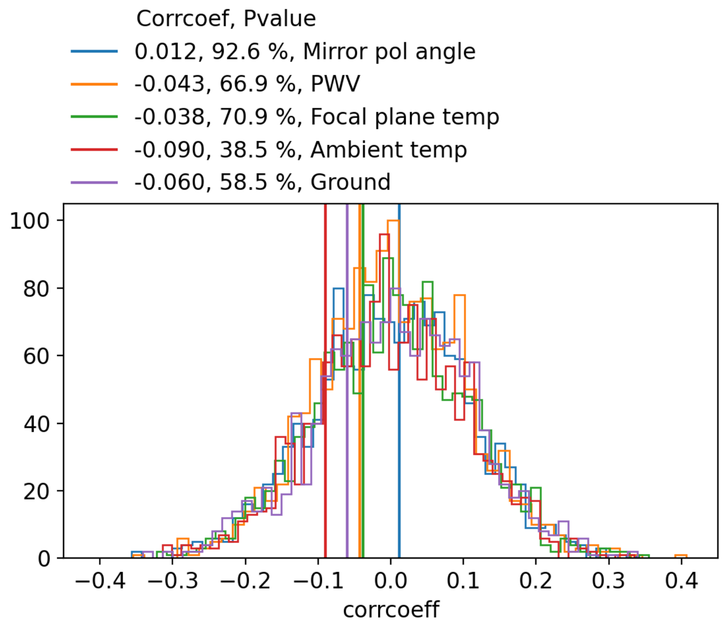

Fig. 5.20 Correlation coefficient between Tau A angle and systematic template.

where

$$\mathrm{Cov}(d, T) = \frac{\sum_t (d_t - \langle d \rangle)(T_t - \langle T \rangle) \cdot \sigma_t^{-2}}{\sum_t \sigma_t^{-2}}. \tag{5.43}$$

is the weighted covariance, and

$$\langle d \rangle = \frac{\sum_t d_t \cdot \sigma_t^{-2}}{\sum_t \sigma_t^{-2}}, \langle T \rangle = \frac{\sum_t T_t \cdot \sigma_t^{-2}}{\sum_t \sigma_t^{-2}} \tag{5.44}$$

are the weighted average. Figure 5.20 shows the significance of the correlation coefficients obtained by comparing the correlation coefficients for 1440 noise realizations. We performed test with the average of PWV, ambient temperature, focal plane stage temperature, and polarization angle of mirror polarization as templates, and no significant correlation was found. Earlier in the data analysis, this method was beneficial to identify systematics and determine the optimum calibration and analysis strategies. This method led to the detection of the PWV-dependent mis-estimation of the I2P leakage and the mis-calibration of the polarization angle in the telescope coordinate with correlation coefficients 0.51 and 0.55, respectively, resulting in the improvement of the angle calibration discussed in Sec 5.6.

5.10 Results

We report the results of Tau A polarization angle, its frequency spectrum, upper bounds of its oscillation amplitude, and the upper bounds of ALP-photon coupling, $g_{a\gamma\gamma}$.

Our estimated timestream of Tau A polarization angle is shown in the top panel of Fig. 5.21. The black dots in bottom panel of Fig. 5.21 shows its LSSA at frequency bins below f_{NYQ} (Eq. 5.21). To

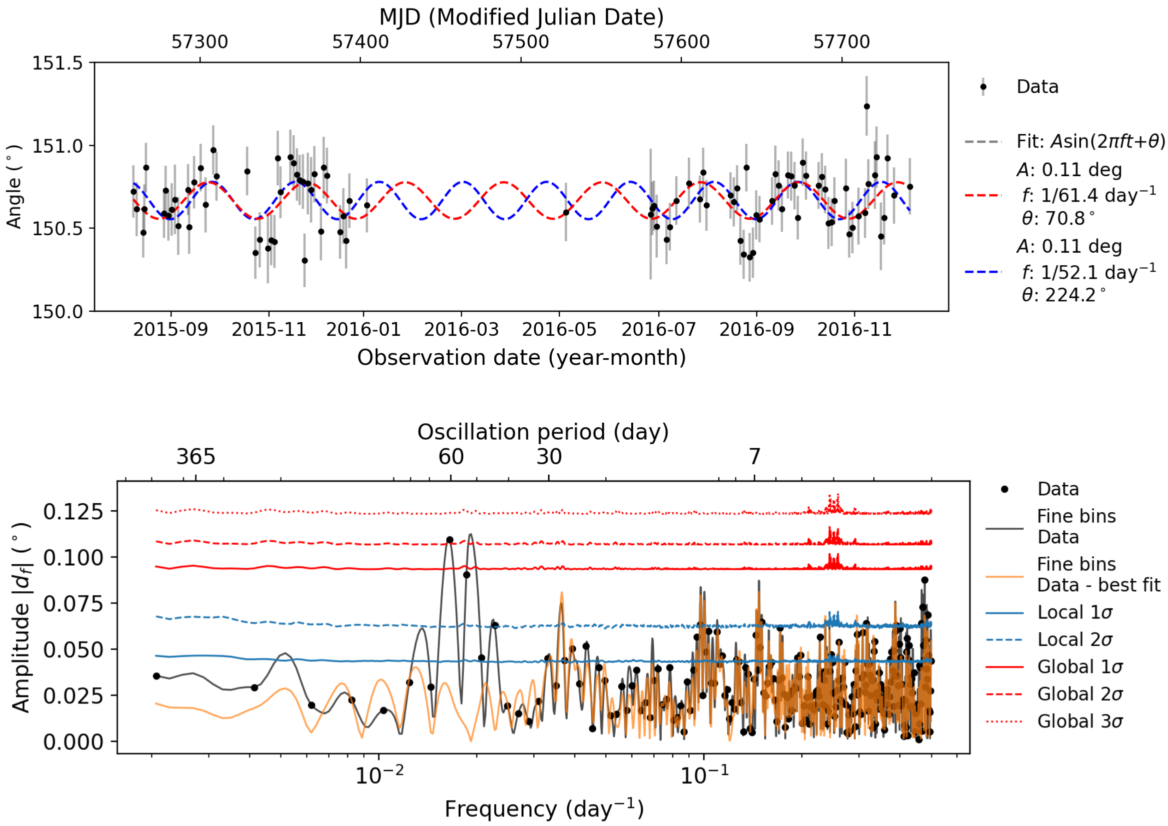

Fig. 5.21 Top: The measured polarization angle of Tau A superimposed on the best-fit sine curves. The phase of the oscillation (θ) is defined in MJD. Number of observations is small from January 2016 to July 2016, because angular distance between Sun and Tau A is small in this period, also because of the maintenance of the instruments. There are two equally significant oscillation modes. Bottom: Amplitudes of the LSSA of data compared with the approximated amplitudes with certain local and global significance levels. The black dots shows the LSSA of data at frequency bins of Eq. 5.21, the black line shows the LSSA of data at 10 times more finely sampled frequency bins.

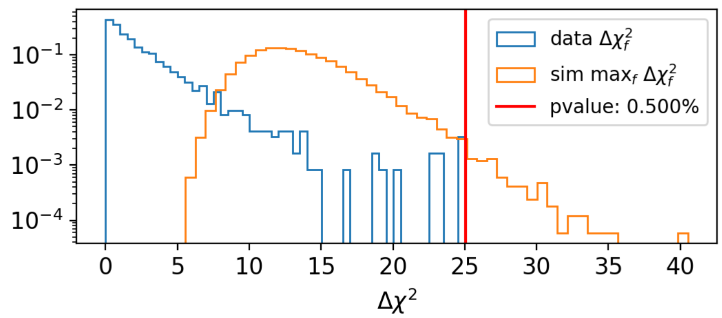

Fig. 5.22 The global significance of oscillation mode at 61 day^{-1} is 2.5σ, corresponding to a p-value of 0.5%. The red lines shows the global significance.

evaluate the detection significance, test statistics were computed using a total of 24,000 noise realizations generated based on the bootstrap method (Sec. 5.7) to have sufficient accuracy of the significance level up to 3σ. The blue lines and red lines in the bottom panel of Fig. 5.21 show the approximated amplitudes with certain local and global significance levels.[9] Figure 5.22 shows the distribution of test statistics, the largest significance level we found is p-value of 0.50%, corresponding to 2.5σ, at 1/61 day^{-1}.

The black solid line in Fig. 5.21 shows the LSSA with 10 times finer frequency bins than Eq 5.21. Another peak at 1/52 day^{-1} which is not captured by the sparse frequency bins is found to have the significance level of 2.5σ by calculating the test statistics over the 10 times finer frequency bins. The bottom panel of Fig. 5.21 also shows the spectrum of data minus the best fit sine curve. The data minus best fit is consistent with the null hypothesis, with the global significance level smaller than 1σ. This means that the two most significant oscillation modes are correlated, and the result can be interpreted as a hint of a single-mode oscillation signal. We also confirmed that the null-test pass criteria were still met with 10 times finer frequency bins.

The local significance level of these two most significant oscillation modes are found to be 4.4σ and 4.5σ analytically. The axion-like oscillation at 1/61 day^{-1} and 1/52 day^{-1} corresponds to ALP mass of 7.8×10^{-22} eV and 9.2×10^{-22} eV, respectively. The possible interpretations of the hint of signal is discussed in Sec. 5.12.

The 95% upper bounds on the oscillation amplitudes at frequency bins below $f_{\rm NYQ}$ are shown in top panel of Fig. 5.23. As a measure of our experimental sensitivity, we report the median upper bound below $f_{\rm NYQ}$ as 0.065°. The upper bound is obtained with the Frequentist approach by the classic Neyman construction [130] as[10]

$$\int_0^{\hat{A}_{\rm obs}} d\hat{A}\; P(\hat{A}|A^{95\%}) = 0.05, \tag{5.45}$$

where $P(\hat{A}|A)$ is the probability density for $\hat{A}$, which is obtained by Monte Carlo simulations of $\hat{A}$ using Eq. 5.27. The bottom paneld of Fig. 5.23 shows the 95% upper bounds extended to frequency bins larger than $f_{\rm NYQ}$ (Eq. 5.22). Due to aliasing, the signal seen at f ($< f_{\rm NYQ}$) may be aliased from higher

[9]For example, the amplitude of 1σ local significance level is $\sqrt{\mathrm{percentile}(\Delta\chi^2_f, 84.1)\,\langle|n_f|^2\rangle}$ and the amplitude of 1σ global significance level is $\sqrt{\mathrm{percentile}(\Delta\chi^2, 84.1)\,\langle|n_f|^2\rangle}$.

[10]Here, the alternative hypothesis is always equal to 1, because the likelihood (Eq. 5.27) is symmetric with respect to the sign of A, and $\hat{A}$ is always within the physical boundary $\hat{A} \geq 0$.

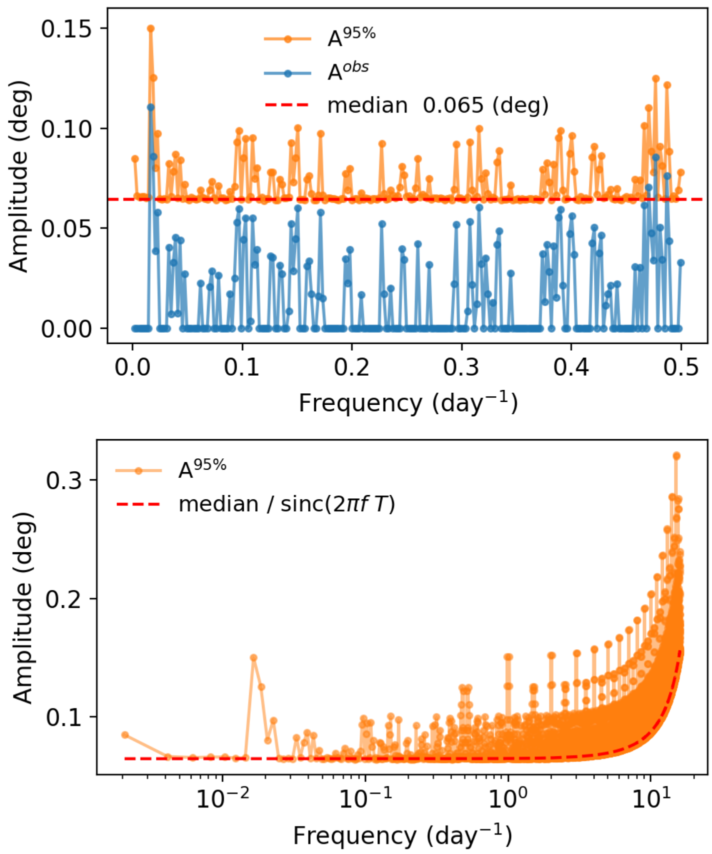

Fig. 5.23 Top: 95% upper bound and measured polarization oscillation amplitudes below $f_{\rm NYQ}$. Bottom: Extended 95% upper bound of polarization oscillation amplitudes.

frequencies. The red dashed curve represents smoothed approximation of our upper bounds [11]

$$A < (0.065^\circ) \times \mathrm{sinc}\left(\frac{f}{7.6\,\mathrm{day}^{-1}}\right)^{-1}. \tag{5.46}$$

The 95% upper bounds of $g_{a\gamma\gamma}$ assuming stochastic ALP field are also constructed using the Neyman construction. The detailed derivation of it is described in Appendix C.3[12]. The median 95% upper bound on the effective oscillation amplitudes below $f_{\rm NYQ}$ is $\sqrt{g^{2,95\%}} = 0.13^\circ$. Assuming that ALP constitutes all the density of the local dark matter ($\kappa = 1$, $\rho_0 = 0.3\,\mathrm{GeV/cm^3}$), the smoothed approximation of our stochastic bounds is

$$g_{a\gamma\gamma} \leq (2.16 \times 10^{-12}\,\mathrm{GeV}^{-1}) \times \left(\frac{m_a}{10^{-21}\,\mathrm{eV}}\right) \times \mathrm{sinc}\left(\frac{m_a}{3.7\times 10^{-19}\,\mathrm{eV}}\right)^{-1}. \tag{5.47}$$

[11] Smoothed approximation is constructed by the median below $f_{\rm NYQ}$ and the transfer function of one-hour averaging effect (Eq. C.4).

[12] The stochastic bounds obtained by this method are 2.2 times conservative than the deterministic bounds using Bayesian inference with a flat prior. The scaling between these two are consistent with our previous result demonstrated in Polarbear Collaboration [152].

Table 5.5 Error budget of the polarization angle of Tau A. The median statistical uncertainty per observation and the RMS of the systematic polarization angle fluctuations are shown.

Type of statistical error	Median σ_t (deg)
Statistical error of Tau A	0.16
Polarization angle calibration by A_4	0.02

Type of systematic error	RMS (deg)
I2P leakage	0.06
Ground	0.03
Residual $1/f$ noise	0.01
MD breaking	< 0.01
Pointing	0.006
TOD filter bias	0.005
Detector angle	0.002

Our bounds are shown in Fig. 5.24 along with the other selected constraints. Our bounds for individual frequencies and the smoothed approximation are shown by red and black curves, respectively. The black dashed line shows the 95% upper bounds assuming that the amplitude of the ALP field is deterministically given by the density of local DM, so called “deterministic bounds". Our smoothed approximation of our deterministic bounds is[13]

$$g_{a\gamma\gamma}^{\text{deterministic}} \leq (1.0 \times 10^{-12}\,\text{GeV}^{-1}) \times \left(\frac{m_a}{10^{-21}\,\text{eV}}\right) \times \text{sinc}\left(\frac{m_a}{3.7 \times 10^{-19}\,\text{eV}}\right)^{-1}. \tag{5.48}$$

Our primary science result is the stochastic bounds, because the deterministic bounds do not account for the expected variation of the ALP field.

5.11 Systematics

This section presents the dedicated studies for the evaluation of possible systematic errors. Table 5.5 shows the median statistical uncertainty per observation, and the RMS of the systematics, the systematic time-dependent polarization angle fluctuations.

The frequency distribution of systematic polarization angle fluctuation is estimated by its LSSA. The overall systematics as well as the individual systematics are shown in Fig. 5.25. The systematics is shown up to f_{NYQ}, because systematics and statistical error scales the same at frequencies higher than f_{NYQ}. The correlation coefficient between different systematics are found to be smaller than 0.3, as shown in right panel of Fig. 5.25. The overall systematics is formed by quadrature sum of individual systematics. We find the total systematic to be subdominant to the statistical error at all frequencies.

5.11.1 Polarization angle calibration

The uncertainty of polarization angle calibration in telescope coordinate produces additional statistical uncertainty in the measured Tau A polarization angle. The overall uncertainty of the polarization angle calibration in telescope coordinate is given by the statistical error of the instrumental polarization angle

[13] The upper bound of deterministic ALP field is obtained by substituting $A^{95\%}$ as the effective amplitude $\sqrt{g^2}$ in Eq. C.18.

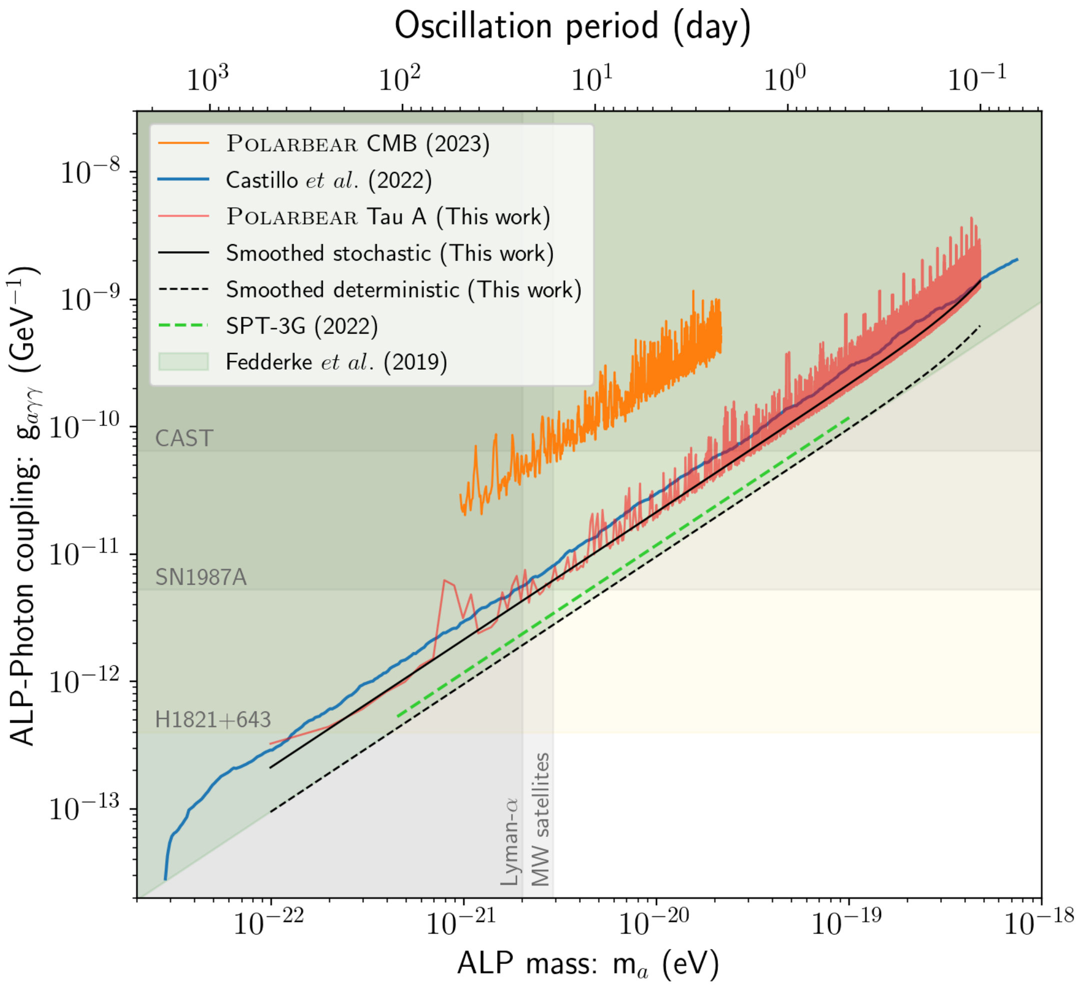

Fig. 5.24 95% Upper bound of $g_{a\gamma\gamma}$. The upper bounds assuming a stochastic ALP field is shown by solid lines. The orange solid curve represents a constraint by searching for axion-like oscillation from CMB [152]. The blue sold curve represents a constraint by searching for axion-like oscillation from various pulsars and Tau A [32]. The red solid curve represents our stochastic bounds, the primary results of this study. The black curve represents the smoothed approximation of our stochastic bounds (Eq. 5.47). The upper bounds assuming deterministic ALP field are shown by dashed curves. The green dashed line represents a constraint by searching for axion-like oscillation of CMB [179]. The black dashed curve represents the smoothed approximation of our deterministic bounds (Eq. 5.48). The green shaded bound represents a constraint from the absence of the suppression of CMB polarization due to the axion-like oscillation in the recombination era [49]. The upper bound from the CAST experiment [31], an absence of the gamma-ray excess of SN1987A [142], and an absence of the X-ray spectral distortions of the quasar H1821+643 [177] are shown. The lower bound on the ALP mass by the Lyman-α forest [77] and the Milky Way satellite galaxies [41] are also shown.

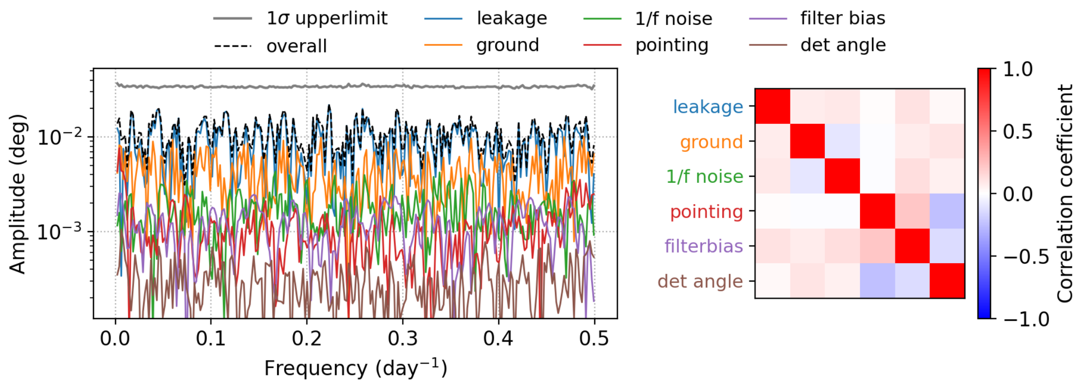

Fig. 5.25 Statistical uncertainty compared with the systematic error. The total systematic is formed by quadrature sum of amplitudes. The right panel shows the cross-correlation coefficients between dominant systematics. The cross-correlation among systematics is smaller than 0.3.

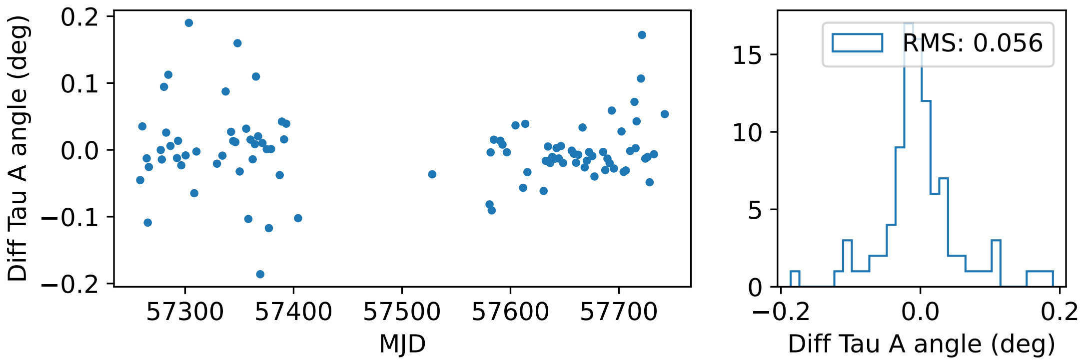

Fig. 5.26 Left: Estimated systematic polarization angle fluctuation of TauA due to I2P leakage. Right: Histogram of the estimated systematic polarization angle fluctuation of TauA due to I2P leakage.

per observation, 0.02° STD (Sec. 5.6.3). This uncertainty degenerately includes time constant, timing offset, and HWP angle uncertainties. The upper bound of the uncertainty due to the time constant and timing offset is estimated to be $< 0.04°$ and $< 0.03°$, respectively, from the chopped thermal source calibration.

5.11.2 Intensity to polarization leakage

The I2P leakage is the calibration parameter that requires the highest accuracy. Mis-estimation of the I2P leakage can produce systematic polarization angle fluctuation. Since the average polarization fraction of Tau A at 150 GHz is 7%, the uncertainty of the I2P leakage coefficient of 0.02% per observation leads to a systematic error of the Tau A polarization angle of $\sim 0.1°$ (Eq. 5.16). The systematics due to the uncertainty of I2P leakage was estimated by the difference of Tau A angle when different model of I2P (Sec. 5.6.2) are applied. The possible polarization angle fluctuation due to I2P mis-estimation is 0.06° RMS (Fig. 5.26).

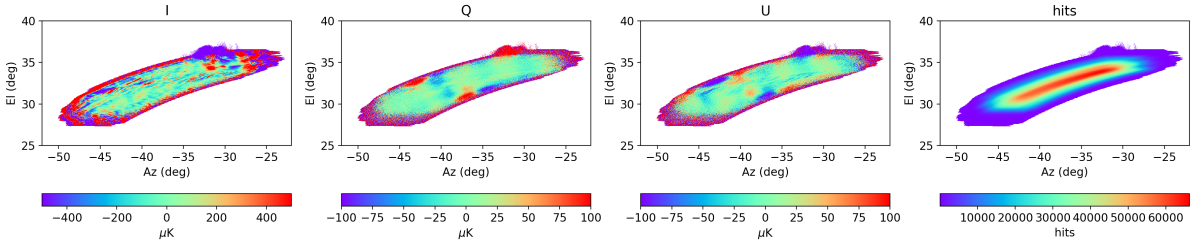

Fig. 5.27 Full coadded ground map

5.11.3 Ground

The systematic contamination of data synchronous with the telescope's pointing in ground coordinates is called ground contamination. During Tau A observations, the telescope tracks Tau A by changing azimuth and elevation simultaneously (Sec. 5.3). Due to its complexity of the scan strategy, the subtraction of the ground contamination is not performed in the time domain, in contrast to the CMB analysis. Here we evaluate the effect of signal synchronized with the ground coordinate on the polarization angle of Tau A. First, we generate a ground polarization map for each observation by stacking the timestreams in the ground coordinate, masking timestreams around Tau A within 12′ diameter. A Tau A hit map in ground coordinate for each observation is generated simultaneously from the masked timestreams. Figure 5.27 shows the full-season co-added ground map. The polarization signal synchronized to the ground coordinates is found to be about 100 μK maximum, which is more than order of magnitude smaller than the polarization signal of Tau A ($\simeq$20 mK). Polarization angle bias due to the ground contamination is evaluated by taking the average of ground map over the Tau A hit map with inverse noise weighting for each observation as

$$\psi + \Delta\psi = \frac{1}{2}\tan^{-1}\left(\frac{\sum_p^{\varnothing<12'} U_p^{\text{Tau A}} + \sum_p^{\text{Tau A hit}} U_p^{\text{Ground}}}{\sum_p^{\varnothing<12'} Q_p^{\text{Tau A}} + \sum_p^{\text{Tau A hit}} Q_p^{\text{Ground}}}\right). \tag{5.49}$$

The possible systematic polarization angle fluctuation due to the ground contamination is 0.03° RMS (Fig. 5.28).

5.11.4 Residual $1/f$ noise

The $1/f$ noise also produces systematic polarization angle fluctuation, because the statistical uncertainty for each observation is estimated by the detector-by-detector signflip noise estimation, which cancels the $1/f$ noise that is common between detectors (Sec. 5.7). This $1/f$ noise is modeled by stacking all detectors' timestreams in time domain, masking around Tau A within 12′ diameter for each observation (Eq. 5.7). The stacked timestream is projected to the sky using the pointing of each detector to make a residual $1/f$ map (Fig. 5.29). The polarization angle bias due to the $1/f$ noise is evaluated by adding the residual $1/f$ noise map to the Tau A signal as

$$\psi + \Delta\psi = \frac{1}{2}\tan^{-1}\left(\frac{\sum_p^{\varnothing<12'} U_p^{\text{Tau A}} + \sum_p^{\varnothing<12'} U_p^{1/f}}{\sum_p^{\varnothing<12'} Q_p^{\text{Tau A}} + \sum_p^{\varnothing<12'} Q_p^{1/f}}\right). \tag{5.50}$$

The systematic polarization angle fluctuation due to the residual $1/f$ is 0.01° RMS (Fig. 5.30).

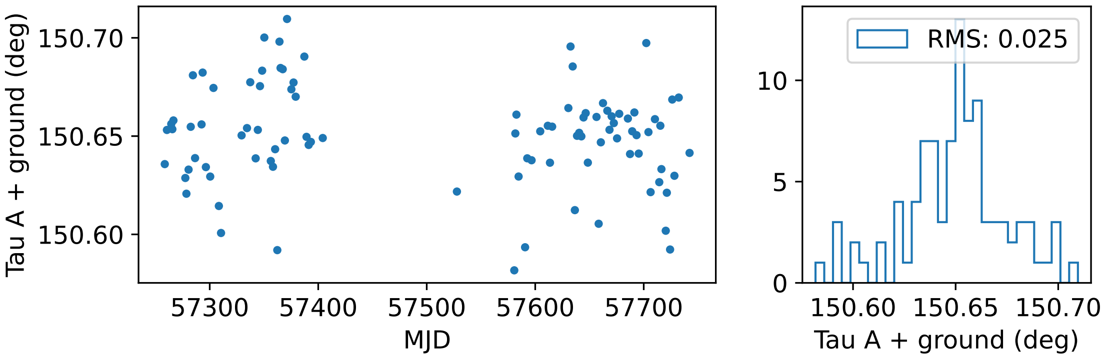

Fig. 5.28 Left: Estimated daily polarization angle of Tau A with the ground contamination. Right: Histogram of the polarization angle of Tau A plus ground contamination.

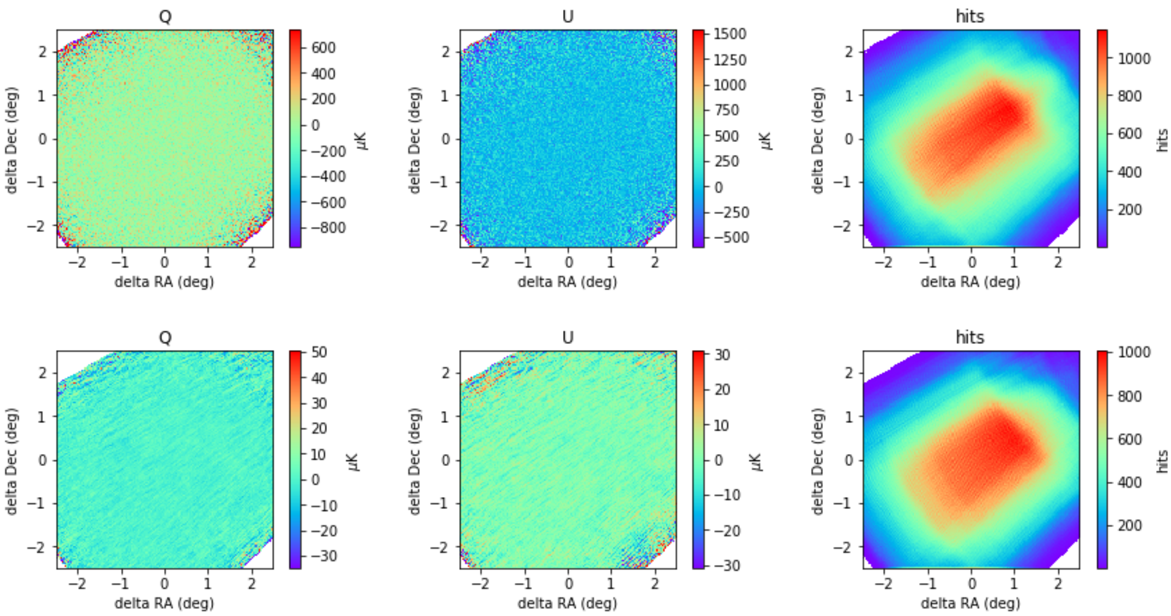

Fig. 5.29 Residual $1/f$ noise map (Bottom) compared with signflip map (Top). The residual $1/f$ noise is negligibly small compared with statistical noise.

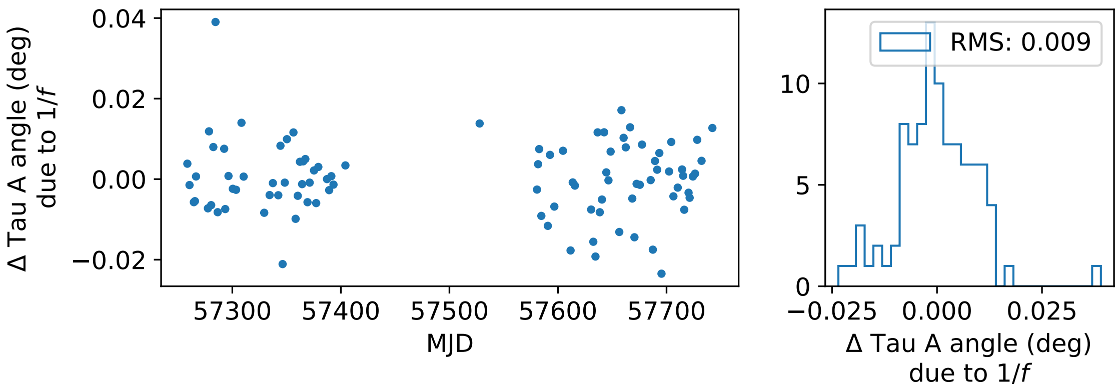

Fig. 5.30 Left: Estimated systematic polarization angle fluctuation due to residual $1/f$ noise. Right: Histogram of the systematic polarization angle fluctuation due to residual $1/f$ noise.

5.11.5 MD breaking

The POLARBEAR telescope is a off-center Gregorian design which satisfies Mizuguchi-Dragone (MD) condition to cancel the cross-polarization at the primary and secondary mirrors [121, 43]. The systematic contamination due to the cross polarization from breaking the MD condition by the HWP located at the prime focus of the telescope is expected to be negligibly small. Matsuda et al. [113] simulated the effects for the same telescope with POLARBEAR-2 receiver. We consider the leading effect the cross polarization, the dipole component of Q and U mixing, to put the upper limit of systematics. Dipole component of each detector cancel with each other due to its focal plane distribution, but the pattern of cancellation differs from day to day, resulting in time-dependent systematic errors.

$$\mathrm{Monopole}(\theta,\phi) = \frac{1}{\sqrt{\pi\sigma^2}}\exp\left(-\frac{\theta^2}{2\sigma^2}\right) \tag{5.51}$$

$$\mathrm{Dipole}(\theta,\phi) = \mathrm{Monopole}(\theta,\phi)(\theta\cos\phi - \theta\sin\phi)\sqrt{2}/\sigma \tag{5.52}$$

We simulated the upper limit of the bias due to the residual dipole component assuming the worst orientation of the dipole component and 2% of Q and U mixing.

$$\phi + \delta\phi = \arctan\left(\frac{\langle \mathrm{TauA}\ U \otimes M_{UU}\rangle + \langle \mathrm{TauA}\ Q \otimes M_{QU}\rangle}{\langle \mathrm{TauA}\ Q \otimes M_{QQ}\rangle + \langle \mathrm{TauA}\ U \otimes M_{UQ}\rangle}\right), \tag{5.53}$$

where $\otimes$ is a convolution, and assumed simplified Muller matrix as follows

$$B(\theta,\phi) = \begin{pmatrix} \mathrm{Monopole} & & & \\ & \mathrm{Monopole} & p\mathrm{Dipole} & \\ & p\mathrm{Dipole} & \mathrm{Monopole} & \\ & & & \mathrm{Monopole} \end{pmatrix}. \tag{5.54}$$

The upper bound of the systematic polarization angle fluctuation is found to be 0.01° (Fig. 5.32).

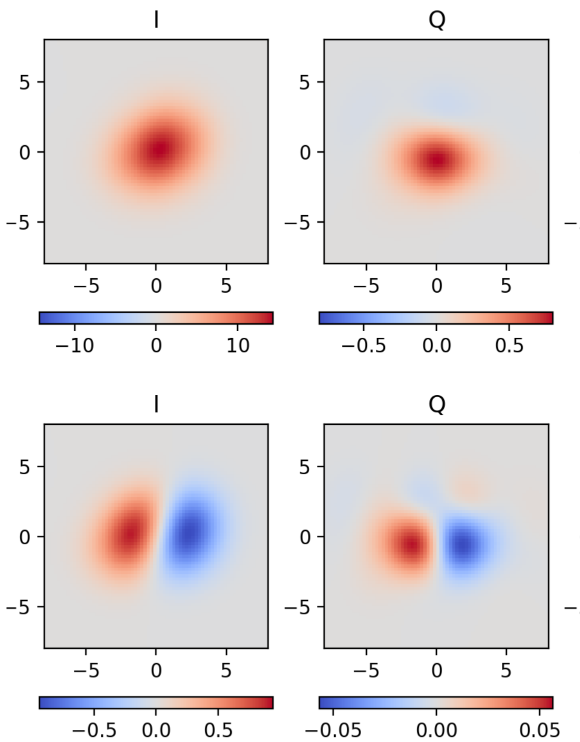

Fig. 5.31 Top: IRAM Tau A map convoluted by monopole Gaussian with 3.6′ FWHM. Bottom: IRAM Tau A map convoluted by Dipole Gaussian with 3.6′ FWHM.

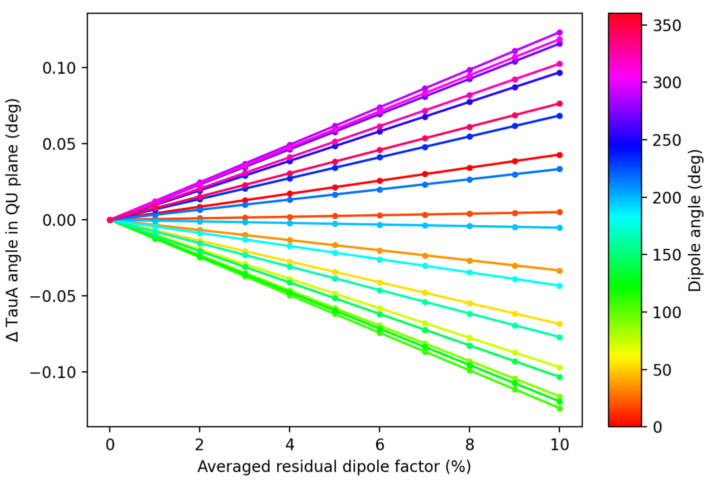

Fig. 5.32 Polarization angle bias due to residual dipole factor of MD breaking.

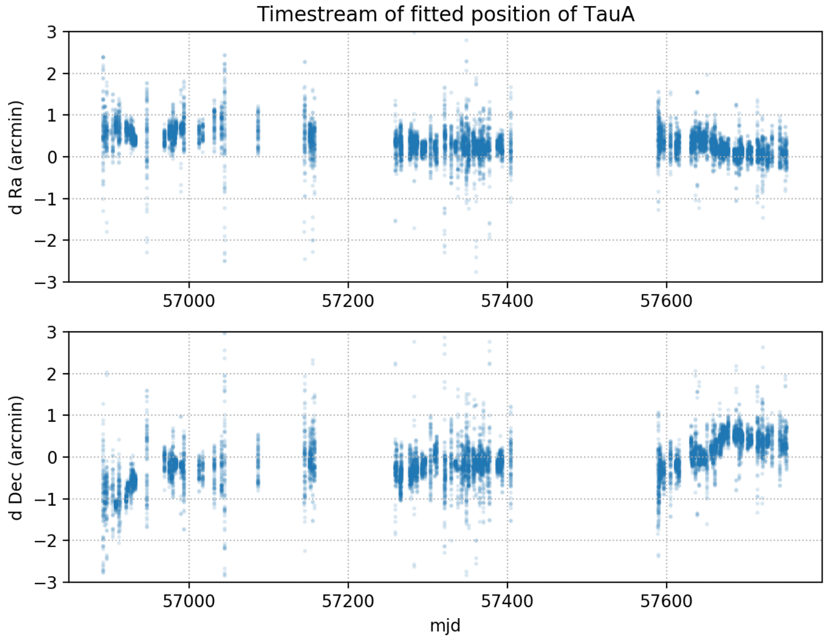

Fig. 5.33 The time trend of the fitted sky position of TauA.

5.11.6 Pointing

The boresight pointing of the telescope propagates to the polarization angle of Tau A through the transformation of polarization angle from telescope coordinate to sky coordinate. The observation-by-observation fluctuation of the boresight pointing was evaluated by the variation of the sky position of Tau A intensity signal. We evaluated the polarization uncertainty due to the uncertainty of boresight pointing by fitting the demodulated and filtered timestream of Tau A intensity in time-domain. The Tau A intensity time-domain model was constructed by convolving the Tau A map observed by IRAM [15] with the telescope beam and then scanning it on simulation. The possible systematic polarization angle fluctuation due to the boresight pointing error is 0.006° RMS.

Since the bias is negligibly small compared with statistical error and dominant systematic errors, we do not apply correction for this effect (Fig. 5.34).

5.11.7 TOD filter bias

Since we adopts the filtered binned mapmaking method, the Tau A angle estimated in map domain is biased (Sec. 5.7). We evaluated the amount of the bias of TOD filtering on the full TOD simulation of Tau A as follows. We used the Tau A map measured by IRAM [15] convoluted by telescope beam (3.6′ FWHM Gaussian) as the unbiased Tau A map, which is the input of full TOD simulation (Fig. 5.35). We scanned the unbiased map on simulation to obtain simulated timestream data, and then applied same TOD filters (demodulation and polynomial filter) as data to obtain the unbiased map. In the simulation, the imperfection of instruments are ignored, such as the time constant of detectors, inefficiency of polarization and intensity to polarization leakage. Figure 5.35 shows the unbiased map and biased map. The systematic polarization angle fluctuation due to the filtering and mapmaking is found to be 0.005° RMS (Fig. 5.36).

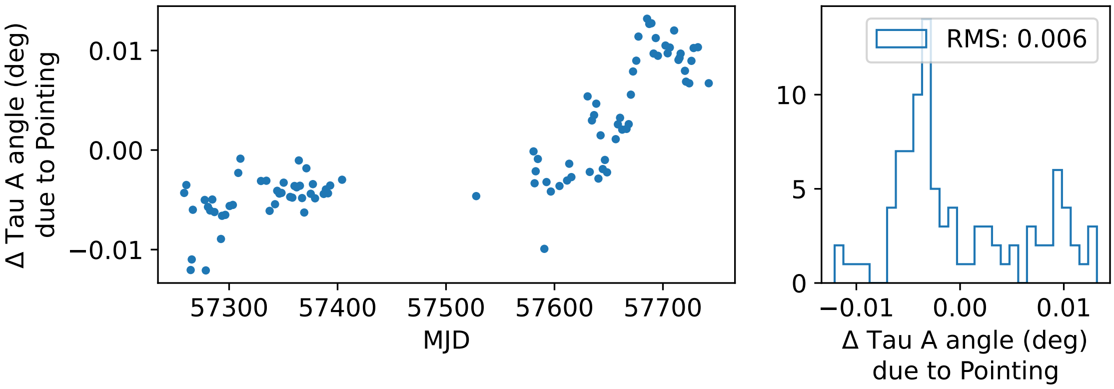

Fig. 5.34 Left: Estimated systematic polarization angle fluctuation of TauA due to pointing error. Right: Histogram of the estimated systematic polarization angle fluctuation of TauA due to pointing error.

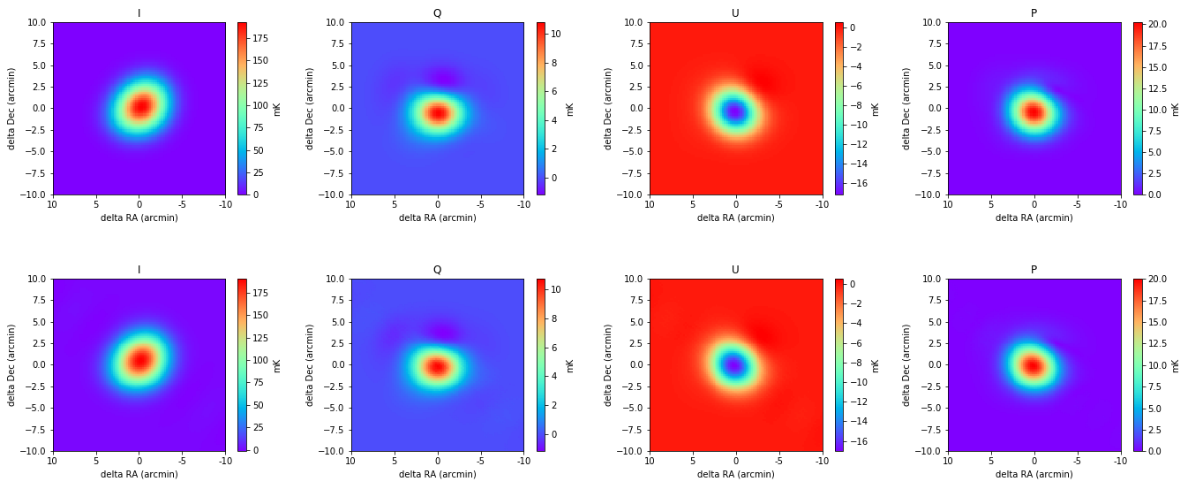

Fig. 5.35 The unbiased map used for Tau A simulation. the IRAM map is convulated by with the Gaussian beam with 3.6′ FWHM. Bottom: Biased map after data filtering.

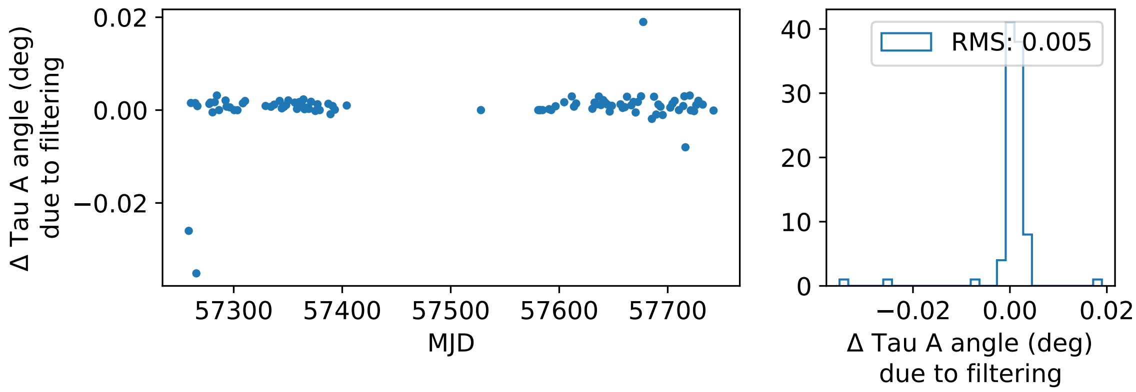

Fig. 5.36 Left: Estimated systematic polarization angle fluctuation of TauA due to TOD filtering and mapmaking biases. Right: Histogram of the estimated systematic polarization angle fluctuation of TauA due to TOD filtering and mapmaking biases.

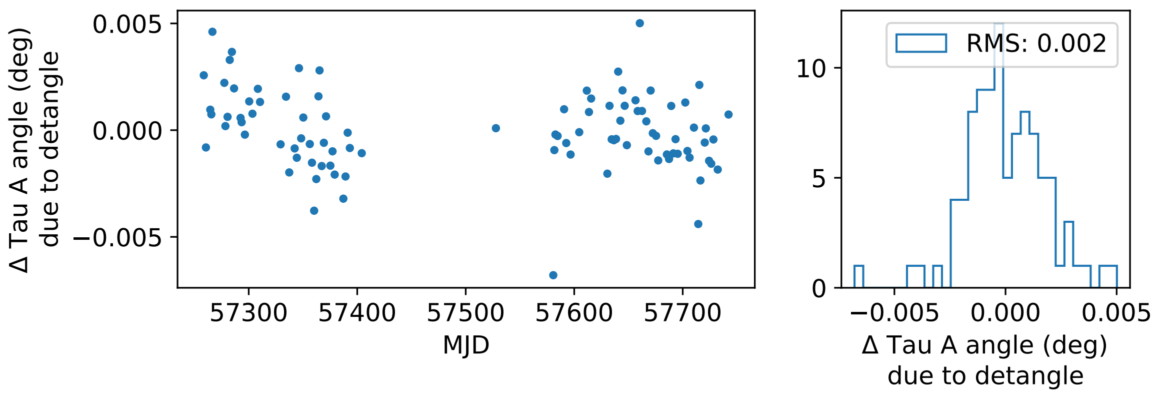

Fig. 5.37 Left: Estimated systematic polarization angle fluctuation due to detector angles, Right: Histogram of the systematic polarization angle fluctuation due to detector angles.

5.11.8 Detector angle

The mis-calibration of detector angle can produce systematic polarization angle fluctuation because the data selection is different for each observation. The possible systematic polarization angle fluctuation is estimated by the average detector angle uncertainty in each observation. The uncertainty of each detector angle, calibrated over the entire observation period, is estimated to be 0.1°, by the variation of the Tau A polarization angle measured by each detector. The estimated systematic polarization angle fluctuation due to the detector angle is 0.002° RMS (Fig. 5.37).

5.11.9 Circular polarization of Tau A

The upper bound of the circular polarization fraction of Tau A is set to 0.2% at 90 GHz by Wiesemeyer, H. et al. [198] The circular polarization of Tau A can propagates to the systematic error of polarization angle through the effect of mixing circular polarization and linear polarization due to the imperfection of HWP. The mixing effect is characterized to by the s parameter of the HWP Mueller matrix and is smaller than 0.2 [55]. In general, this circular and linear polarization mixing is not negligible because the polarization fraction of Tau A is 7% at 150 GHz. However, this effect is negligible for the case of the rapid modulation by rotating HWP, because the circular polarized signal gets modulated into the 2nd harmonic signal of the HWP rotation frequency, while the linear polarized signal gets modulated into the 4th harmonic signal [55].

5.12 Discussion

We discuss the possible interpretations for the hint of signal, periodic oscillation of Tau A polarization angle with significance level 2.5σ (Sec. 5.10).

5.12.1 Investigation of systematic contamination

This section presents the additional exploration of the systematic contamination. We estimated the potential systematics from the templates of environmental and instrumental conditions using the correlation of the measured Tau A polarization angle with them. The amount of systematics was modeled assuming that the systematics is proportional to the systematic templates. The proportionality coefficient ($\hat{c}$) for the conversion of the systematic template into angular units is determined by minimizing the cost function

$$\hat{c} = \underset{c}{\operatorname{argmin}} \left(|\mathrm{Corr}(T, d - cT)| \right) \tag{5.55}$$

where d is the Tau A angle, and T is the systematic template. As a conservative estimate, we construct the 95% upper bound of the proportionality coefficient as

$$\hat{c}^{95\%} = |\hat{c}^{\mathrm{best}}| + \mathrm{percentile}\left(\{|c| \mid c \in Cs\}, 95 \right) \tag{5.56}$$

$$Cs = \left\{ \underset{c}{\operatorname{argmin}} \left(|\mathrm{Corrcoef}(T, n_l - cT)| \right) \middle| \, l = 0, 1, ..., 1440 \right\}, \tag{5.57}$$

where n_l is the l-th noise realization based on the bootstrap method (Sec. 5.7). Figure 5.38 shows the spectrum of potential systematics modeled as $\hat{c}^{95\%}T$ compared with the 1σ upper bound of statistical uncertainty. No significant potential systematics is found around the frequency bins where we found the hint of signal. Potential systematics is larger than statistical uncertainty in some frequency bins, however this does not necessarily mean the actual systematics, because these are conservative estimates, and their accuracies are limited by the statistical error of the polarization angle of Tau A.

Another way to probe the systematics is to check the season-by-season consistency of the hint of signal as shown in Fig. 5.39. The hint of signal at $1/61\,\mathrm{day}^{-1}$ or $1/52\,\mathrm{day}^{-1}$ is consistently seen in both the 4th and 5th season. Additionally, we performed the null tests with 10 times higher resolution frequency bins and also by limiting the frequency bins to the two most significant bins. No residual systematics with a significance level larger than 2σ was found. Finally, we note that we did not do any on-site maintenance activities on 50 to 60 day cycles.

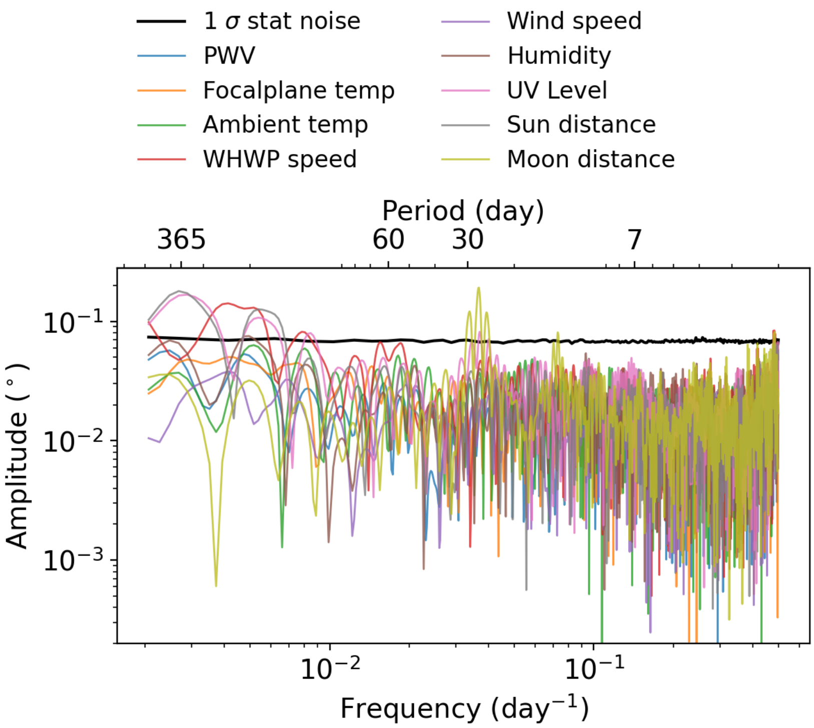

Fig. 5.38 2σ upperlimit of the LSSA of the systematic templates. The black solid line region shows the 1σ upper limit of the statistical noise.

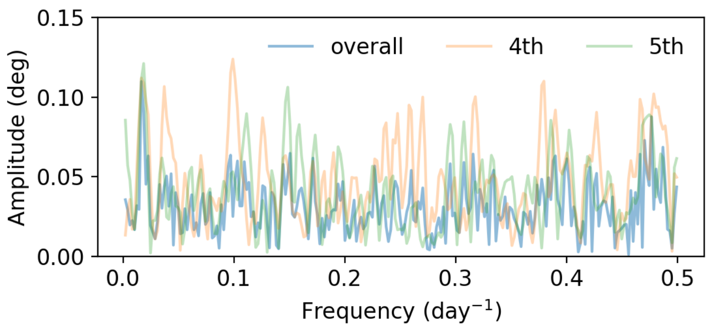

Fig. 5.39 Season by season spectrum of Tau A angle. The hint of signal at 1/61 day^{-1} or 1/52 day^{-1} is consistently seen in two seasons.

5.12.2 Time dependence of Tau A

Intrinsic polarization oscillation of Tau A could be the cause of the hint of signal, because our angular resolution prohibit us to distinguish it from the polarization oscillation induced by the ALP-photon coupling. Our measurement is the overall average of the polarized synchrotron radiation emitted by the charged particles coupled with the magnetic field spread over a range of several light-years. Therefore, even though the Crab pulsar inside the Crab Nebula is a dynamic astronomical object, our measurements are insensitive to the localized dynamics.

However, we cannot exclude the possibility that the Crab pulsar causes observed variability. The time variability of the Crab pulsar has been studied in a wide variety of timescales and wavelengths. To the best of our knowledge, the time variability in two-month period has not been observed. Here we summarize the known time variation of Tau A.

1. Crab pulsar has a rotational period of about 33 milliseconds [21].
2. Giant radio pulses with duration of < 1 minute are observed from Tau A [46, 45].
3. Variability of flux at X-ray or Gamma ray from Crab pulsar exits from years to decades [96, 7].
4. Large variation in the polarization of Crab pulsar and Crab Nebula is reported at X-ray [50, 29].

The polarization angle of Tau A has been measured in a number of experiments. However its time dependence or frequency dependence has been explored only recently. The 95% upper bound of oscillation amplitude of $\sim 1^\circ$ is placed from $6{\times}10^{-4}$ day^{-1} to 10 day^{-1} by Castillo et al. [32] Tau A has been measured in more experiments for intensity than for polarization. Therefore, we investigated if any correlated time dependence of Tau A intensity exists in the observation period of this study using the public daily light curve of the all-sky survey satellites. Figure 5.40 shows the spectrum of the light-curves. We found no significant correlation to our data.

5.12.3 Consistency with other ALP bounds

We discuss the consistency of our results with other ALP bounds. The consistency analysis discussed in this section is only valid if the hint of signal we found is purely from ALP. To the best of our knowledge, the tightest upper bound of the axion-like polarization oscillation of local ALP field is placed by SPTpol Collaboration [179], with the median upper bound of 0.071° from 1/100 day^{-1} to 1 day^{-1}, while our median upper bound is 0.065°. The largest discrepancy is found at the frequencies where we found the hint of oscillation. Fig 5.41 indicates the significance of the discrepancy.

A more significant discrepancy is found when we translate the polarization oscillation to the constraint of ALP-photon coupling. One of the tightest upper bounds of the axion-photon coupling is placed by the absence of the suppression of CMB *E*-mode power spectrum due to the axion-like oscillation in the recombination era [49],

$$g_{a\gamma\gamma} \le (9.6 \times 10^{-13}\,\mathrm{GeV}^{-1}) \times \left(\frac{m_a}{10^{-21}\,\mathrm{eV}}\right). \tag{5.58}$$

The 95.5% upper bound of 5.0×10^{-13} GeV^{-1} at $m_a < 10^{-12}$ eV is also placed from the absence of the distortions of the X-ray spectrum of the quasar H1821+643 due to the ALP-photon coupling [177]. The bottom panel of Fig. 5.41 indicates the significance of the discrepancy. The 95.5% upper bound of $5.0{\times}10^{-13}$ GeV^{-1} at $m_a < 10^{-12}$ eV is also placed from the absence of the distortions of the X-ray spectrum of the quasar H1821+643 due to the ALP-photon coupling [177]. Our bounds are complementary to

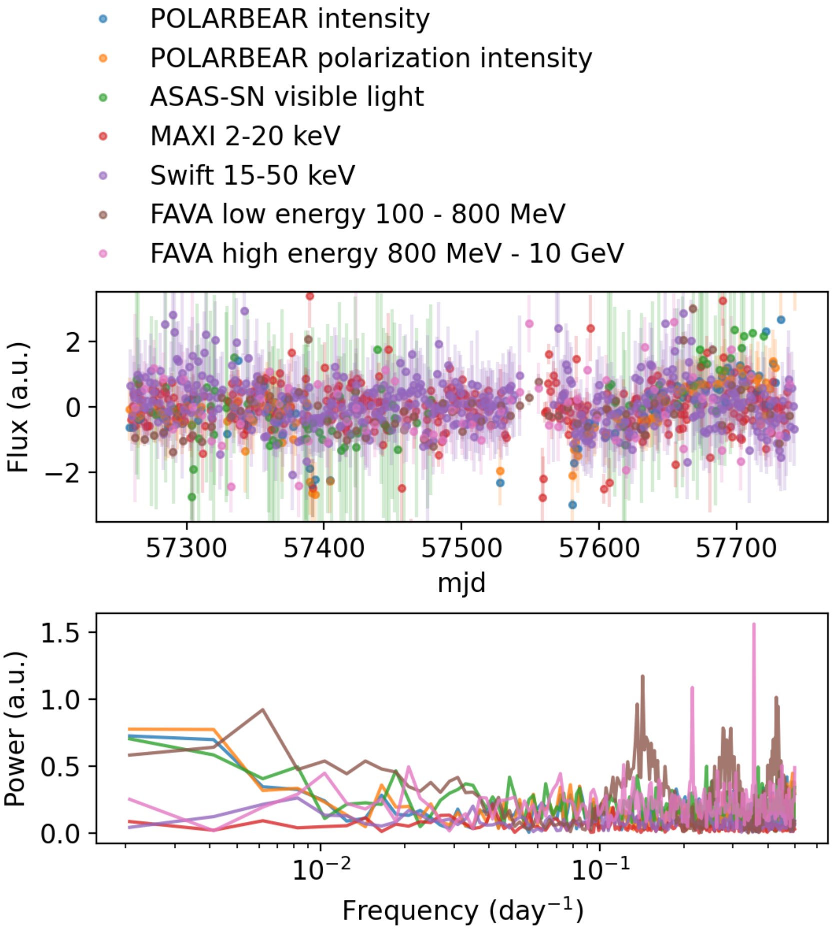

Fig. 5.40 Spectrum of light curve measured by [116, 98, 170, 93, 3].

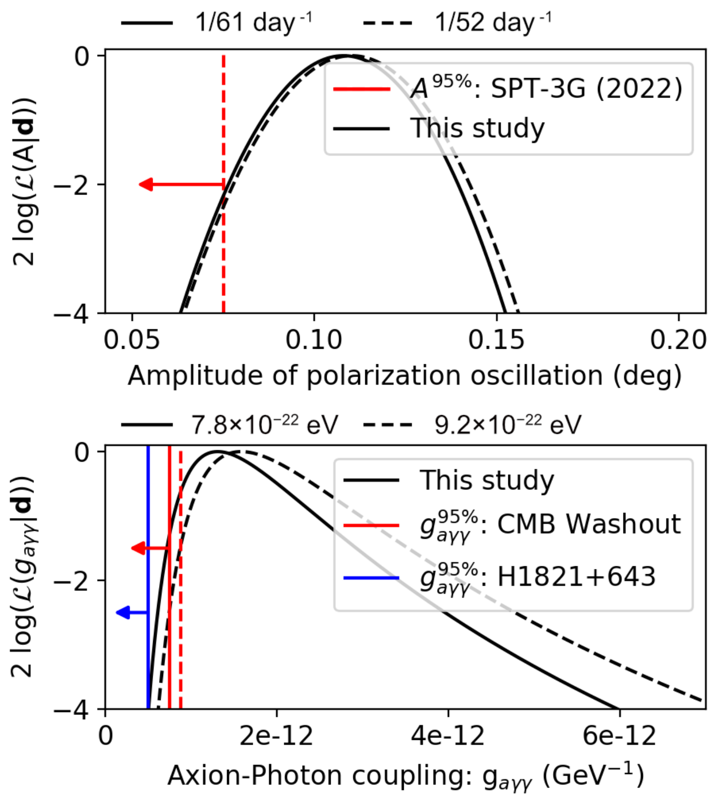

Fig. 5.41 Comparison of the two most significant signals found in this study with other bounds. The red and blue line shows the 95% upper bound by other measurements and the black line shows the likelihood of this study. Top panel compares the amplitude of the axion-like polarization oscillation. Bottom panel compares the ALP-photon coupling.

these bounds because the ALP search by the axion-like oscillation is less dependent on the cosmological model or the model for the galaxy cluster magnetic fields.

Several analyses have claimed to rule out the ultralight DM in mass region where we found a hint of signal, $m_a < 2.0 \times 10^{-21}$ eV by [77] and $m_a < 2.9 \times 10^{-21}$ eV by [41]. However, there are model dependencies in these analyses, our analysis is complementary in searching for an entirely different signal. Also our analysis applies even if the ALP constitutes some fraction of the DM, the bounds get worsen by the square root of the DM fraction, κ.

We also checked the consistency with our previous result, the search for the polarization oscillation in the CMB measured by POLARBEAR Collaboration [152]. The hint of signal we found is below its noise level, and POLARBEAR Collaboration [152] is consistent with this study.

5.13 Conclusion

We performed an improved analysis of the Tau A observations in 4th and 5th seasons of the POLARBEAR experiment. Our result demonstrates a sensitive search for the axion-like polarization oscillation using the calibration data of the ground-based CMB observatory located at the Atacama desert of Chile. To our knowledge, this work provided the tightest upper bound of the polarization oscillation amplitude of Tau A over the frequency range of 0.75 year^{-1} to 0.66 hour^{-1}. The precise measurement of the time dependence of Tau A's polarization angle is also beneficial for understanding the astronomical dynamics of Tau A. This work brought new methodologies for investigating potential systematics, which allowed us to improve the polarization angle calibration method.

Compared to the ALP search using the polarization of the CMB, the sensitivity per unit time is a significant advantage of ALP search with Tau A. Since Tau A is at declination 22°, the ALP search with Tau A is an advantage for the northern observatories, where the Tau A can be observed at higher elevation with less atmospheric loading.

A hint of polarization oscillation signal with amplitude 0.11° was found at 1/61 or 1/52 day^{-1} with global significance level of 2.5σ. The possibility of residual systematics or intrinsic variability of Tau A due to the yet unknown dynamics have been considered, resulting in no clear understanding for either of them. On the other hand, interpreting this as an ALP signal leads to significant tension with other constraints. Future measurements with more statistics will give more conclusive understanding for either possibility. A successor experiment, the Simons Array, employs dichroic detectors including 90 GHz and 150 GHz center band [181]. Since the polarized intensity of synchrotron radiation is proportional to $\nu^{-0.3}$ [196], a more sensitive observation can be expected from the lower frequency band. Also, since the axion-like polarization oscillation is independent from the optical frequency of light, the control of frequency dependent systematics is possible.

Chapter 6

Research impact

This dissertation advances the millimeter-wave polarimetry both in the instrumentation and scientific exploitation. This chapter briefly discusses the research impact of this dissertation.

6.1 Cryogenic half-wave plate modulator

We have developed the cryogenic continuously rotating half-wave plate polarization modulators for the small aperture telescopes of SO. Figure 6.1 shows the current status of the modulators on August 2023. The three CHWPs we developed have been integrated into the three telescopes in US, and one of the telescope (SAT-MF1) has deployed to the observatory in Chile, and planned to start commissioning observation in 2023. Validation of another telescope (SAT-MF2) has also finished, and will be deployed to Chile in 2023. The last telescope is under the final laboratory test in US.

The construction of three additional SATs and CHWPs are planned. The methodologies we developed will contribute to the construction of these CHWPs. Also the SO CHWP design and methodologies can also contribute to the design and trade study for future experiments such as CMB-S4.

6.2 ALP search

The demonstrated ALP search using the Tau A observation of POLARBEAR is extended to its successor experiment, Simons Array. POLARBEAR observed Tau A one hour per day at maximum because it was observed for calibration of the telescope. After the demonstration of the science exploitation from Tau A observations in this dissertation, SA is now conducting an ALP search as one of the science targets with dedicated Tau A observations. Figure 6.2 shows the maximum daily observation time of Tau A by SA, limited by the elevation angle of Tau A observed by SA and the observed angular distance between Tau A and Sun. Figure 6.3 shows the demonstration of dedicated Tau A observation by SA. By maximizing the daily observation time of Tau A, a more sensitive search for ALP is expected.

The methods we have developed, including the phenomenology of the VULF, the validation of the data analysis, and the efficient statistical analysis, can be applied to the search for axion-like polarization using any type of light source.

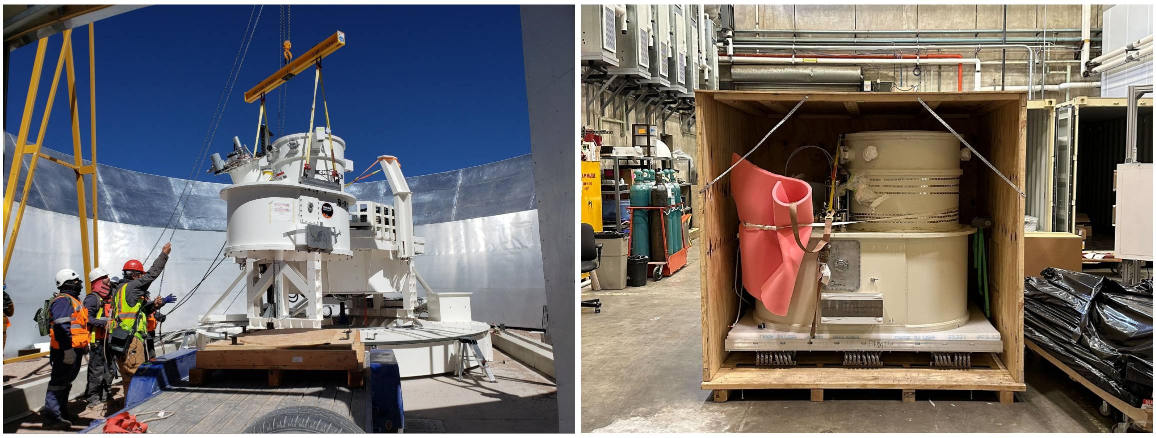

Fig. 6.1 The status of the SO SATs on August 2023. Left: SAT-MF1 is deployed to the observation site and Chile and start commissioning in 2023. Photo credit: Hironobu Nakata. Right: SAT-MF2 has finished laboratory testing at Princeton university and shipped to Chile. Photo credit: Yuhan Wang.

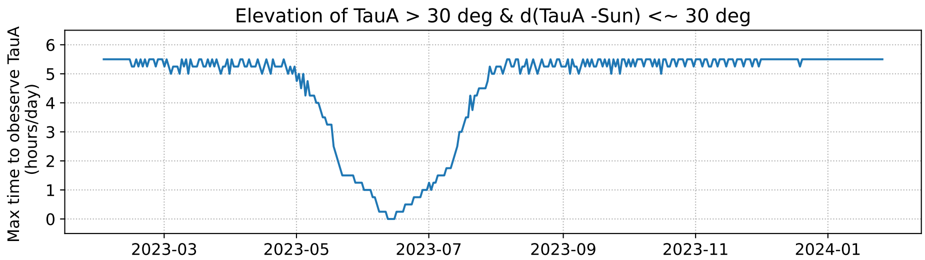

Fig. 6.2 Daily observable time of Tau A from Atacama desert.

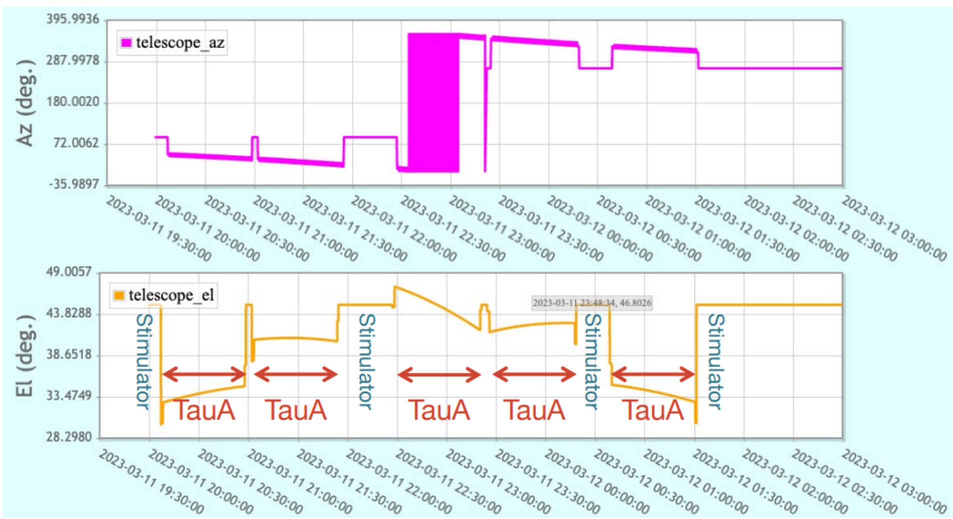

Fig. 6.3 Demonstration of dedicated Tau A observations by SA.

6.3 Conclusion

This dissertation advanced millimeter-wave astrophysics in both the instrumentation and science exploitation. The presented development of CHWPs advances the SO to discover inflation through improved sensitivity and systematic error control. The demonstrated accurate polarization measurements of Tau A advances the dark matter search through the ALP-induced polarization oscillation, and understanding of the dynamics of Tau A.

Appendix A

CHWP

A.1 Scan synchronous modulation of HWP rotation

Here we derive the scan modulation of the angular velocity of the CHWP, (Eq. 3.4). Figure A.1 shows the schematic diagram of the rotating CHWP on the scanning telescope. The coordinate system cab be taken as shown, without the loss of generality. We define r and θ as the circular coordinate of the rotor and $\rho(r,\theta)$ as the density of the rotor, which is symmetric with respect to θ. The angular momentum of the rotating CHWP is

$$L_{\mathrm{HWP}} = \dot{\chi} \iint r\, dr d\theta\, \rho r^2 = \dot{\chi} I, \tag{A.1}$$

where I is the moment of inertia of the rotor.

Next, we calculate the angular momentum induced by the telescope scanning. Let r_0 be the radial distance from the axis of the scan to the center of the rotor. We assume that the bearing is infinitely rigid. This means that the net angular momentum contribution from the telescope scan is only along the direction of the rotor's rotation axis. As shown in Fig. A.1, the angular momentum at each point of the rotor induced by the telescope scan is

$$\begin{aligned}
\delta L_{\mathrm{scan}} &= \hat{n}_{\mathrm{HWP}} \cdot \left(\overrightarrow{r} \times \rho \overrightarrow{v}\right) \\
&= \begin{pmatrix} \cos\theta_{\mathrm{el}} \\ 0 \\ \sin\theta_{\mathrm{el}} \end{pmatrix} \cdot \left\{ \begin{pmatrix} r \sin\theta_{\mathrm{el}} \cos\theta \\ r\sin\theta \\ -r\cos\theta_{\mathrm{el}} \end{pmatrix} \times \rho\dot{\phi} \begin{pmatrix} -r\sin\theta \\ r_0 + r\sin\theta_{\mathrm{el}}\cos\theta \\ 0 \end{pmatrix} \right\} \\
&= \rho\dot{\phi}\left(r_0 r\cos\theta + r^2 \sin\theta_{\mathrm{el}}\right)
\end{aligned} \tag{A.2}$$

where ϕ and θ_{el} are the azimuth and elevation angles of the telescope, respectively. The total angular momentum is obtained by integrating over the rotor as

$$L_{\mathrm{scan}} = \iint r\, dr d\theta\, \delta L_{\mathrm{scan}} = \dot{\phi} \sin\theta_{\mathrm{el}} I \tag{A.3}$$

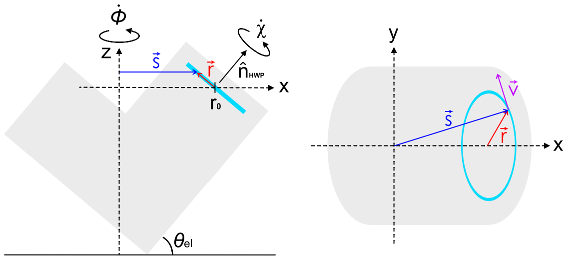

Fig. A.1 Schematic diagram of the rotating CHWP on the scanning telescope. The gray area represents a schematic of the telescope's receiver, while the light blue circle represents the rotor.

From the conservation law of angular momentum, the following equation holds.

$$L_{\text{scan}} + L_{\text{HWP}} = \text{const.} \tag{A.4}$$

Thus, Eq. 3.4 holds.

A.2 Measurement of the displacement of rotor

Here we elaborate on the methods used to make the displacement measurements summarized in Sec. 3.4.5. Displacement measurements along the optical axis are made using the gripping mechanisms (Sec. 3.3.3) and a Hall probe (Sec. 3.3.6) installed below the rotor's magnet ring. The measurement begins by pointing the receiver at an elevation of 90° and fully gripping the rotor. The actuators controlling the gripper positions are then retracted, allowing the rotor to sink along the optical axis. The gripper head geometry is designed such that retraction distance corresponds directly to the rotor displacement, and changes in the Hall probe's measured field are monitored. The total displacement of the rotor is estimated from the distance the grippers have moved while the Hall probe changes linearly. Figure A.2 shows a schematic of the measurement setup and the measured magnetic field of the rotor magnet as the grippers are gradually retracted. The systematic error of the displacement is ±0.3 mm, resulting from changes in the Hall probe sensitivity and the rotor magnet's field caused by temperature drift during the measurement.

The off-center displacement is calculated by the measured additional angle offset between a pair of encoders placed 180° from one another as shown in Fig. A.3. The additional angle offset is

$$d\chi_j = \pi f_{\text{HWP j}} \left(t^0_j - t^1_{j+570} \right), \tag{A.5}$$

where t^i_j is the timing when i-th encoder reads the j-th encoder slot and

$$f_{\text{HWP j}} = \frac{1}{1140(t^0_j - t^0_{j+1})} = \frac{1}{1140(t^1_j - t^1_{j+1})} \tag{A.6}$$

is the rotation frequency. Since the total number of encoder slots is 1140, the slot 570 positions away is at the opposite side of the encoder plate. If the CHWP is completely centered, $d\chi_j$ is always zero. If there is an off-center displacement of the rotor perpendicular to the line connecting the encoders, diametrically opposite slots will travel different distances between detection, resulting in a time delay

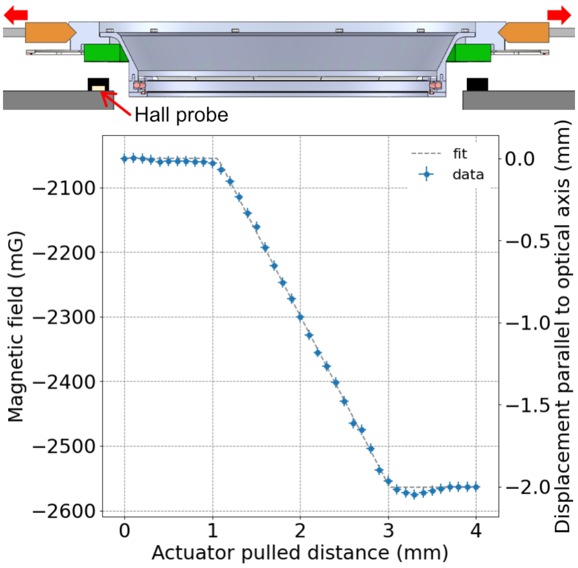

Fig. A.2 Top panel: schematic diagram of the measurement setup for the rotor displacement along the optical axis. The Hall probe is located right below the magnet ring to measure the relative displacement of the rotor. Grippers are completely clear of the rotor when retracted 9 mm. Bottom panel: measurement of the displacement along the optical axis. From 0-1 mm, the rotor is not moving due to the play in the joints of the grippers. From 1-3 mm, the rotor is sliding down the wedge of the gripper heads. From 3 mm onwards, the rotor is floating.

that can be converted to the angle offset, $d\chi_j$. The pair of encoders are synchronized by the shared IRIG-B reference signal described in Sec. 3.4.6. The displacement perpendicular to the line connecting the pair of encoders is thus

$$\text{Displacement}_j = R \times \tan(d\chi_j), \tag{A.7}$$

where $R = 334$ mm is the radius of the encoder slots.

The measurement accuracy of the encoder angle shift due to off-center displacement is 0.02°, which is negligible compared to the required accuracy of the polarization angle calibration. The SAT platform will rotate the boresight ± 60°. Since the phase shift between the pair of encoders is at its maximum when the boresight angle is 0°, the requirement of the accuracy of the polarization angle is satisfied at any boresight angle.

A.3 Precautions

Successful operation of the CHWP requires paying careful attention to a number of system characteristics. This section presents a summary of the precautions we learned to take while building the CHWP and evaluating its performance.

Physical interference of the rotor is the most common inhibitor of CHWP rotation. This interference can be caused by misplaced or loose screws, nuts, tape, motor sprocket magnets, encoder or motor cables, or multi-layer insulation. To avoid the risk of physical interference, use of nuts and tape are minimized, screws are secured with thread-locker (LOCTITE 263) and the motor sprocket magnets are

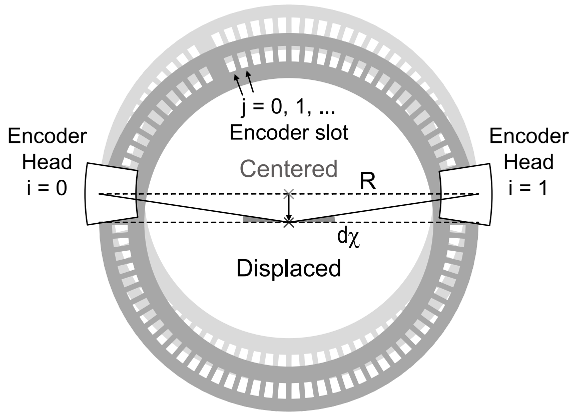

Fig. A.3 The schematic diagram of the measurement setup of the off-center displacement. When the rotor is off-centered perpendicular to the line connecting the encoders, the pair incorrectly measures the rotation angle by $d\chi$. The off-center displacement can be calculated by Eq. A.7.

secured with epoxy (Stycast 2850 FT). Moreover, the magnetic screws or mechanical parts, including 304 stainless steel, must not be used. This is because the rotor's magnet ring is strong enough to dislodge them and cause physical interference.

Care must also be taken in the operation of electrical devices, including the encoders, motors, and grippers. Protective measures for electrical devices are crucial, such as the protection circuit for the optical encoders, the current limit function for the motor drive power source, and the limit switch for the grippers. Finally, drastic temperature changes must be avoided while the encoder LEDs are biased, as exposure to rapidly changing environments can cause degradation.

Appendix B

Dark matter

This section describes the derivation of the two point function of VULF, which is first derived by Derevianko [40].

B.1 Two point function of VULF

From Eq. 4.25, the two point function of VULF is expressed as follows.

$$
\begin{aligned}
\left\langle \phi(\vec{x},t)\phi(\vec{y},s) \right\rangle \propto & \left\langle \int d\vec{k} \sqrt{f_{\mathrm{DM}}\left(\vec{k}\right)} \left\{ c_k \cos\left(\omega_c(1+k^2/2k_0^2)t + \vec{k}\cdot\vec{x}\right) + s_k \sin\left(\omega_c(1+k^2/2k_0^2)t + \vec{k}\cdot\vec{x}\right) \right\} \right. \\
& \left. \times \int d\vec{k} \sqrt{f_{\mathrm{DM}}\left(\vec{k}\right)} \left\{ c_k \cos\left(\omega_c(1+k^2/2k_0^2)t + \vec{k}\cdot\vec{x}\right) + s_k \sin\left(\omega_c(1+k^2/2k_0^2)t + \vec{k}\cdot\vec{x}\right) \right\} \right\rangle \\
= & \iint d\vec{k}' d\vec{k} \sqrt{f_{\mathrm{DM}}\left(\vec{k}\right) f_{\mathrm{DM}}\left(\vec{k}'\right)} \langle c_k c_{k'} \rangle \cos\left(\omega_c(1+k^2/2k_0^2)t + \vec{k}\cdot\vec{x}\right) \cos\left(\omega_c(1+k'^2/2k_0^2)s + \vec{k}'\cdot\vec{y}\right) \\
& + \iint d\vec{k}' d\vec{k} \sqrt{f_{\mathrm{DM}}\left(\vec{k}\right) f_{\mathrm{DM}}\left(\vec{k}'\right)} \langle c_k s_{k'} \rangle \cos\left(\omega_c(1+k^2/2k_0^2)t + \vec{k}\cdot\vec{x}\right) \sin\left(\omega_c(1+k'^2/2k_0^2)s + \vec{k}'\cdot\vec{y}\right) \\
& + \iint d\vec{k}' d\vec{k} \sqrt{f_{\mathrm{DM}}\left(\vec{k}\right) f_{\mathrm{DM}}\left(\vec{k}'\right)} \langle s_k c_{k'} \rangle \sin\left(\omega_c(1+k^2/2k_0^2)t + \vec{k}\cdot\vec{x}\right) \cos\left(\omega_c(1+k'^2/2k_0^2)s + \vec{k}'\cdot\vec{y}\right) \\
& + \iint d\vec{k}' d\vec{k} \sqrt{f_{\mathrm{DM}}\left(\vec{k}\right) f_{\mathrm{DM}}\left(\vec{k}'\right)} \langle s_k s_{k'} \rangle \sin\left(\omega_c(1+k^2/2k_0^2)t + \vec{k}\cdot\vec{x}\right) \sin\left(\omega_c(1+k'^2/2k_0^2)s + \vec{k}'\cdot\vec{y}\right)
\end{aligned}
\tag{B.1}
$$

Since $\{c_{\vec{k}'},\ s_{\vec{k}}\}$ are all independent Gaussian random variables, following equations hold.

$$\langle c_{\vec{k}'} c_{\vec{k}} \rangle = \langle s_{\vec{k}'} s_{\vec{k}} \rangle = \delta^3\left(\vec{k} - \vec{k}'\right) \tag{B.2}$$

$$\langle c_{\vec{k}'} s_{\vec{k}} \rangle = 0. \tag{B.3}$$

Therefore,

$$\begin{aligned}\left\langle\phi(\vec{x},t)\phi(\vec{y},s)\right\rangle &= \frac{\sqrt{\rho_{\mathrm{DM}}(\vec{x})\rho_{\mathrm{DM}}(\vec{y})}}{m^2}\int d\vec{k} f_{\mathrm{DM}}\left(\vec{k}\right)\cos\left(\omega_c(1+k^2/2k_0^2)t+\vec{k}\cdot\vec{x}\right)\cos\left(\omega_c(1+k^2/2k_0^2)s+\vec{k}\cdot\vec{y}\right)\\ &+\frac{\sqrt{\rho_{\mathrm{DM}}(\vec{x})\rho_{\mathrm{DM}}(\vec{y})}}{m^2}\int d\vec{k} f_{\mathrm{DM}}\left(\vec{k}\right)\sin\left(\omega_c(1+k^2/2k_0^2)t+\vec{k}\cdot\vec{x}\right)\sin\left(\omega_c(1+k^2/2k_0^2)s+\vec{k}\cdot\vec{y}\right)\\ &=\frac{\sqrt{\rho_{\mathrm{DM}}(\vec{x})\rho_{\mathrm{DM}}(\vec{y})}}{m^2}\int d\vec{k} f_{\mathrm{DM}}\left(\vec{k}\right)\cos\left(\omega_c(1+k^2/2k_0^2)|t-s|+\vec{k}\cdot|\vec{x}-\vec{y}|\right)\end{aligned} \tag{B.4}$$

Therefore the correlation between the two points of VULF is determined only by the distance as follows:

$$\gamma(\vec{d},\tau)=\int d\vec{k} f_{\mathrm{DM}}\left(\vec{k}\right)\cos\left(\omega_c(1+k^2/2k_0^2)\tau+\vec{k}\cdot\vec{d}\right), \tag{B.5}$$

where $\vec{d}=\vec{x}-\vec{y}$ is the spatial distance and $\tau=t-s$ is the time distance.

B.2 Correlation function in galactic rest frame

The correlation function in galactic rest frame is obtained by substituting the velocity distribution of VULF as

$$f_{\mathrm{DM}}(\vec{k})=\left(\frac{1}{2\pi k_{vir}^2}\right)^{3/2}\int d\vec{k}\exp\left(-\frac{k^2}{2k_{vir}^2}\right), \tag{B.6}$$

where $k_{\mathrm{vir}}=mv_{\mathrm{vir}}/\hbar$ is the wave vector of the virial velocity. Then, the the correlation function leads to

$$\begin{aligned}\gamma(\vec{d},\tau)&=\left(\frac{1}{2\pi k_{vir}^2}\right)^{3/2}\int d\vec{k}\exp\left(-\frac{k^2}{2k_{vir}^2}\right)\cos(\omega_c(1+k^2/2k_0^2)\tau+\vec{k}\cdot\vec{d})\\ &=\left(\frac{\lambda_{\mathrm{coh}}^2}{2\pi}\right)^{3/2}\frac{\exp(i\omega_c\tau)}{2}\int_0^{2\pi}d\phi\int_{-\infty}^{\infty}k^2dk\exp\left(-\frac{k^2\lambda_{\mathrm{coh}}^2}{2}(1-i\tau/\tau_{\mathrm{coh}})\right)\int_0^{2\pi}\sin\theta d\theta\exp\left(ikd\cos\theta\right)+cc.,\end{aligned} \tag{B.7}$$

where cc. stands for complex conjugate. We substitute $t=\cos\theta$.

$$\gamma(\vec{d},\tau)=\left(\frac{\lambda_{\mathrm{coh}}^2}{2\pi}\right)^{3/2}\pi\exp(i\omega_c\tau)\int_{-\infty}^{\infty}k^2dk\exp\left(-\frac{k^2\lambda_{\mathrm{coh}}}{2}(1-i\tau/\tau_{\mathrm{coh}})\right)\int_{-1}^{1}dt\exp\left(ikd\cdot t\right)+cc. \tag{B.8}$$

$$=\left(\frac{\lambda_{\mathrm{coh}}^2}{2\pi}\right)^{3/2}\frac{2\pi\exp(i\omega_c\tau)}{id}\int_{-\infty}^{\infty}dk\,k\exp\left(-\frac{k^2\lambda_{\mathrm{coh}}}{2}(1-i\tau/\tau_{\mathrm{coh}})\right)\sin(kd)+cc. \tag{B.9}$$

From the residue theorem, the following equation holds.

$$\int_{-\infty}^{\infty}x\exp(-ax^2)\sin(bx)=\frac{1}{2}\sqrt{\frac{\pi}{a^3}}b\exp\left(-\frac{b^2}{4a}\right). \tag{B.10}$$

Therefore,

$$\gamma(\vec{d},\tau) = -i\exp(i\omega_c\tau)\left(\frac{1}{1-i\tau/\tau_{\rm coh}}\right)^{3/2}\exp\left(-\frac{d^2}{2\lambda_{\rm coh}^2}\frac{1}{1-i\tau/\tau_{\rm coh}}\right)+cc. \tag{B.11}$$

The following equation holds for $z \in C, a, b \in \mathcal{R}$,

$$z\exp(a+ib)+cc. = \mathrm{norm}(z)\exp(a)\cos(b+\mathrm{argument}(z)). \tag{B.12}$$

Therefore, we obtain the correlation function in galactic rest frame.

$$\gamma(\vec{d},\tau) = \frac{\exp\left(-\frac{|\vec{d}|^2}{2\lambda_{\rm coh}^2}\frac{1}{1+\tau^2/\tau_{\rm coh}^2}\right)}{(1+\tau^2/\tau_{\rm coh}^2)^{3/4}}\cos\left(\omega_c\tau+\frac{|\vec{d}|^2}{2\lambda_{\rm coh}^2}\frac{\tau/\tau_{\rm coh}}{1+\tau^2/\tau_{\rm coh}^2}-\frac{3}{2}\arctan(\tau/\tau_{\rm coh})\right) \tag{B.13}$$

B.3 Correlation function in lab-frame

The correlation function in lab-frame which is moving at the velocity of $\vec{v}_g(\ll c)$ with respect to the galactic rest frame, is obtained by the coordinate transformation. The wave function is transformed by Galilean boosts from galaxy rest frame to moving frame as follows [103].

$$\begin{aligned}\Psi(\vec{x},t) &= \sum_{\vec{k}} A_k\exp(i\vec{k}\cdot\vec{x}-i\omega t)\\ &\to \exp\left(-i\frac{m}{\hbar}\vec{v}\cdot\vec{x}-i\frac{mv^2}{2c^2}t\right)\sum_{\vec{k}}A_k\exp\left(i\vec{k}\cdot(\vec{x}+\vec{v}t)-i\omega t\right)\end{aligned} \tag{B.14}$$

Therefore the correlation in lab-frame is obtained as

$$\gamma(\vec{d},\tau) = \frac{\exp\left(-\frac{|\vec{d}-\vec{v}\tau|^2}{2\lambda_{\rm coh}^2}\frac{1}{1+\tau^2/\tau_{\rm coh}^2}\right)}{(1+\tau^2/\tau_{\rm coh}^2)^{3/4}}\cos\left(\omega_c(1+v^2/2c^2)\tau+\frac{m}{\hbar}\vec{v}\cdot\vec{d}+\frac{|\vec{d}-\vec{v}\tau|^2}{2\lambda_{\rm coh}^2}\frac{\tau/\tau_{\rm coh}}{1+\tau^2/\tau_{\rm coh}^2}-\frac{3}{2}\arctan(\tau/\tau_{\rm coh})\right), \tag{B.15}$$

where $\omega_c(1+v_g^2/2c^2)$ is a Doppler shifted Compton frequency. Usually, the time scale of interest (τ) is much shorter than the coherence time of the VULF ($\tau_{\rm coh}$), and the correlation function is simplified as

$$\gamma(\vec{d},\tau) = \exp\left(-\frac{|\vec{d}-\vec{v}_g\tau|^2}{2\lambda_{\rm coh}^2}\right)\cos\left(\omega_c(1+v_g^2/2c^2)\tau+\frac{m}{\hbar}\vec{v}_g\cdot\vec{d}\right). \tag{B.16}$$

Appendix C

ALP search

C.1 Transfer function

This section describes the derivation of the transfer functions shown in Fig. 5.17. First, the estimation of Tau A angle by averaging over the single observation period of one hour biases the oscillation signal at higher frequency. We consider observing an axion-like polarization oscillation of Tau A at f with unit amplitude and phase θ as

$$\psi(t) = \psi_0 + \sin(2\pi f t + \theta). \tag{C.1}$$

The polarization oscillation averaged from t_s to t_e is

$$\begin{aligned} \psi_t &= \frac{1}{t_e - t_s}\int_{t_s}^{t_e} dt'\ \psi(t') && \text{(C.2)} \\ &= \psi_0 + \mathrm{sinc}(\pi f \Delta T)\sin\left(2\pi f t + \theta\right), && \text{(C.3)} \end{aligned}$$

where $\Delta T = t_e - t_s(\simeq$ one hour) is the observation period, $t = (t_s + t_e)/2$ is the average observation time, and we used a unnormalized sinc function. The corresponding transfer function is

$$F_f^{\text{average}} = \mathrm{sinc}(\pi f \Delta T). \tag{C.4}$$

Second, the observation timing jitter acts like a low-pass filter, but is negligible compared to the time averaging.

Third, the calibration of the relative polarization angle between detectors (Sec. 5.6.1) also biases the signal. With the axion-like polarization oscillation of Eq. C.1, the polarization angle of Tau A measured by i-th detector will be biased by

$$\Delta\psi_i = \sum_{t\in t(i)}(\psi_t \sigma_{t,i}^{-2}) / \sum_{t\in t(i)} \sigma_{t,i}^{-2} - \psi_0, \tag{C.5}$$

where $\sigma_{t,i}$ is the i-th detector's statistical uncertainty of the polarization angle of Tau A per observation, and $t(i)$ is timing of the set of observations when the i-the detector is operating. Since we calibrate each detector's polarization angle using the Tau A polarization angle averaged over the entire observation period, $\Delta\psi_i$ is equivalent to the amount of each detectors' mis-calibration. Then, the measured axion-like polarization oscillation is biased as

$$\hat{\psi}_t = \frac{\sum_{i\in i(t)} (\psi_t - \Delta\psi_i) \times \sigma_{t,i}^{-2}}{\sum_{i\in i(t)} \sigma_{t,i}^{-2}}, \tag{C.6}$$

where $i(t)$ is a set of detectors working in the observation performed at t. We calculate the bias from detector angle calibration by averaging over the phase of oscillation for each frequency as

$$F_f^{\mathrm{polcal}} = \frac{1}{2\pi}\int_0^{2\pi} \left|\sum_t F_{ft}\hat{\psi}_t\right| d\theta. \tag{C.7}$$

Finally, the calibration of the absolute polarization angle (ψ_0) also biases the LSSA as

$$F_f^{\mathrm{abscal}} = \frac{1}{2\pi}\int_0^{2\pi} \left|\sum_t F_{ft}\left(\hat{\psi}_t - \frac{\sum_t \hat{\psi}_t\sigma_t^{-2}}{\sum_t \sigma_t^{-2}}\right)\right| d\theta. \tag{C.8}$$

C.2 Estimator

This section compares the methods for estimating $g_{a\gamma\gamma}$. In this study, we estimate $g_{a\gamma\gamma}$ by maximizing the probability density for obtaining the LSSA of the data. We call this estimator the "frequency estimator". This is understood if we consider the case where the noise covariance matrix (Eq. 5.30) is diagonal, i.e., when the timestamp is regularly spaced and the error bars are uniformly distributed. In this case, $2|\tilde{d}_f|^2/\langle|n_f|^2\rangle$ follows chi-square distribution with two degrees of freedom and Eq. 5.34 is simplified as

$$P(\tilde{d}_f|g_{a\gamma\gamma},\phi_{\mathrm{DM}}) = \frac{\exp\left(-\frac{|\tilde{d}_f|^2}{\langle|\tilde{n}_f|^2\rangle + g_{a\gamma\gamma}^2F_f^2\phi_{\mathrm{DM}}^2/4}\right)}{\pi(\langle|\tilde{n}_f|^2\rangle + g_{a\gamma\gamma}^2F_f^2\phi_{\mathrm{DM}}^2/4)}. \tag{C.9}$$

Eq. 5.33 is a maximum likelihood estimator for this likelihood function.

On the other hand, POLARBEAR Collaboration [152] estimates the $g_{a\gamma\gamma}$ by maximizing the probability density for obtaining time-domain data[1]. We call this estimator as "full estimator". The likelihood function is

$$P(d_t|g_{a\gamma\gamma}) = \iint d\phi_c d\phi_s\, P(d_t|\phi_c,\phi_s,g_{a\gamma\gamma})P(\phi_c)P(\phi_s), \tag{C.10}$$

where

$$P(\phi_c) = \frac{\exp\left(-\frac{\phi_c^2}{\phi_{\mathrm{DM}}^2}\right)}{\sqrt{\pi\phi_{\mathrm{DM}}^2}},\ P(\phi_s) = \frac{\exp\left(-\frac{\phi_s^2}{\phi_{\mathrm{DM}}^2}\right)}{\sqrt{\pi\phi_{\mathrm{DM}}^2}} \tag{C.11}$$

[1] The stochastic ALP field with 2D Gaussian distributed complex amplitude and Rayleigh distributed amplitude and uniform distributed phase is equivalent.

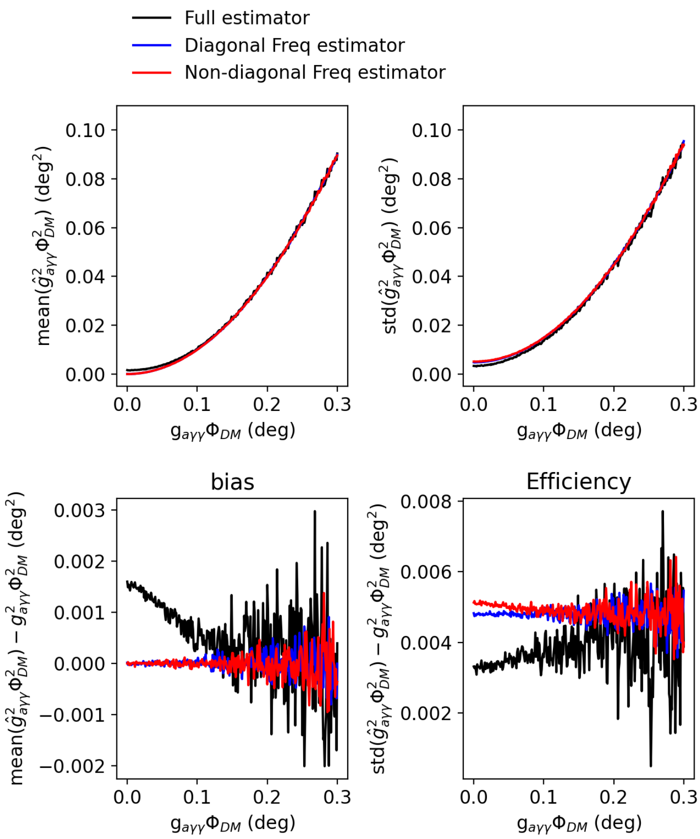

Fig. C.1 Comparison the bias and efficiency of estimators of $g^2_{a\gamma\gamma}$. The frequency bin with the most non-diagonal noise covariance is compared.

is the probability density for the stochastic oscillation amplitudes of ALP, and

$$P(d_t|\phi_c, \phi_s, g_{a\gamma\gamma}) = \prod_t \frac{e^{-\frac{1}{2}\left[(d_t-\psi(t))/\sigma_t\right]^2}}{\sqrt{2\pi\sigma_t^2}} \tag{C.12}$$

is the probability density for obtaining data when the stochastic oscillation amplitudes of ALP are given.

Figure C.1 compares the bias and efficiency of the "frequency estimator" and "full estimator". The frequency estimator is unbiased but the efficiency is slightly larger than "full estimator". The "full estimator" is biased when the signal is small. Another advantage of the "frequency estimator" is its small computational cost. This is because "full estimator" requires convolution for constructing likelihood (Eq. C.10), while the corresponding convolution is analytically conducted for the "frequency estimator".

C.3 Upper bound

This section describes the method for estimating the upper bound of $g_{a\gamma\gamma}$. First, we consider the constraint on $g^2 \equiv g^2_{a\gamma\gamma} F_f^2 \phi^2_{\rm DM}/4$, the square of the effective amplitude of polarization oscillation, then we convert it to the constraint on $g_{a\gamma\gamma}$.

The probability density for $\hat{g}^2$, $P(\hat{g}^2|g^2_{\rm true})$, can be generated by the Monte Carlo simulation using Eqs. 5.33 and 5.34. To quantify the preference of null hypothesis over the presence of signal, we compare the probability to obtain $\hat{g}^2$ less often than $g^2_{\rm obs}$ (=$P_{\rm null}$) over that of alternative hypothesis (=$P_{\rm alt}$). The probability $P_{\rm null}$ is obtained with the following ordering:

$$P_{\rm null}(g^2_{\rm true}) = \int_{\Sigma(\hat{g}^2)} P(\hat{g}^2|g^2_{\rm true}), \tag{C.13}$$

where the integration range is determined to satisfy following three conditions:

$$\Sigma(\hat{g}^2) = \{\, \hat{g}^2 \mid g^2 \leq g_1^2 \text{ or } g_2^2 \leq g^2 \,\} \tag{C.14}$$
$$P(\hat{g}^2 \leq \hat{g}_1^2|g^2_{\rm true}) = P(\hat{g}_2^2 \leq \hat{g}^2|g^2_{\rm true}) \tag{C.15}$$
$$\hat{g}_1^2 = \hat{g}^2_{\rm obs} \text{ or } \hat{g}_2^2 = \hat{g}^2_{\rm obs}. \tag{C.16}$$

The probability for the alternative hypothesis is obtained in similar way, $P_{\rm alt} = P_{\rm null}(g^2_{\rm best}(\hat{g}^2_{\rm obs}))$. The $g^2_{\rm best}(\hat{g}^2_{\rm obs})$ is $g^2_{\rm true}$ which maximizes $P_{\rm null}$ within the physical region. Finally, we obtain the 90% confidence interval of g^2 as

$$\mathrm{CI} = \left\{ g^2_{\rm true} \;\middle|\; \frac{P_{\rm null}(g^2_{\rm true})}{P_{\rm alt}} \geq 0.9 \right\} \tag{C.17}$$

Since we do not find signal with significance larger than 3σ, we only report the 95% upper bound from the upper side of the 90% confidence interval. The upper bound of $g_{a\gamma\gamma}F_f\phi_{\rm DM}/2$ is square root of that of g^2. From the relation between the mean amplitude of ALP (= $\phi_{\rm DM}$) and the DM density (Eq. 5.3), the 95% upper bound of $g_{a\gamma\gamma}/$ is

$$g_{a\gamma\gamma} \leq (1.60 \times 10^{-11}\ \mathrm{GeV}^{-1}) \times \left(\frac{\sqrt{g^{2,95\%}}/F_f}{1^\circ}\right)\left(\frac{m_a}{10^{-21}\ \mathrm{eV}}\right)\left(\frac{\kappa\rho_0}{0.3\ \mathrm{GeV/cm^3}}\right)^{-1/2}, \tag{C.18}$$

where κ is the fraction of DM that ALP constitutes and ρ_0 is the local DM density.

Acronyms

AC	Alternating Current
ALP	Axion like particle
AR	Anti-Reflection
Az	azimuthal angle
BAO	Baryon Acoustic Oscillation
BBB	BeagleBone Black
CAD	Computer-aided design
CDM	Cold Dark Matter
CES	Constant Elevation Scan
CHWP	Cryogenic half-wave plate
CI	Confidence Interval
CMB	Cosmic Microwave Background
CV	Cosmic variance
DC	Direct Current
Dec	declination angle
DfMux	Digital Frequency-Domain Multiplexing
DFSZ	Dine–Fischler–Srednicki–Zhitnitsky
DM	Dark matter
DR	Dilution refrigerator
El	Elevation angle
EOM	Equation of Motion
FLRW	Friedmann–Lemaitre–Robertson–Walker
FWHM	Full Width at Half Maximum
GUT	Grand Unified Theory
HWP	Half-wave plate
HWPSS	Half-wave plate synchronous signal
IC	integrated circuit
IR	Infra-red
IRIG	Inter-range instrumentation group timecodes
KS	Kolmogorov–Smirnov
KSVZ	Kim–Shifman–Vainshtein–Zakharov
ΛCDM	Λ and Cold Dark Matter
LED	Light-emitting diode
LF	Low frequency
LAT	Large aperture telescope
LBNL	Lawrence Berkeley National Laboratory
LSSA	Least Square Spectral Analysis Amplitude
MC	Monte-Carlo
MD	Mizuguchi-Dragone
MF	Middle frequency
MJD	Modified Julian Date
MW	Milky Way Galaxy

NdFeB	Neodymium magnet
NEP	Noise equivalence power
NET	Noise equivalence temperature
Pa	Parallactic angle
PB	POLARBEAR
PD	Photo Detector
PID	Proportional-Integral-Differential
PSD	Power Spectrum Density
PTC	Pulse tube cooler
PTE	Probability to exceed
PWV	Precipitable Water Vapor
QCD	Quantum Chromo Dynamics
RA	Right Ascention
SA	Simons Array
SAT	Small Aperture Telescope
SHM	Standard Halo Model
SMB	Super conducitng Magnetic Bearing
SO	Simons Observatory
SQUID	Superconducting quantum interference device
SSS	Scan synchronous signal
STD	Standard deviation
TES	Transition Edge sensor
TOD	Time ordered data
UCSD	University of California, San Diego
UHF	Ultra high frequency
VULF	Virialized Ultralight Field
WHWP	Warm half-wave plate
WIMP	Weakly Interacting Massive Particle
YBCO	Yttrium barium copper oxide

Glossaries

$1/f$ noise	Noise whose power spectrum depends on frequency as power law with negative index
I2P	Intensity to Polarization
Tau A	The Crab Nebula

Bibliography

[1] K. N. Abazajian, P. Adshead, Z. Ahmed, et al., "CMB-S4 Science Book, First Edition", arXiv:1610.02743 [astro-ph, physics:gr-qc, physics:hep-ph, physics:hep-th] (2016).

[2] L. Abbott and S. Pi, *Inflationary Cosmology* (World Scientific Publishing Company, 1986).

[3] S. Abdollahi, M. Ackermann, M. Ajello, et al., "The Second Catalog of Flaring Gamma-Ray Sources from the Fermi All-sky Variability Analysis", The Astrophysical Journal **846**, 34 (2017).

[4] M. H. Abitbol, Z. Ahmed, D. Barron, et al., "CMB-S4 Technology Book, First Edition", arXiv:1706.02464 [astro-ph] (2017).

[5] M. H. Abitbol et al. (Simons Observatory), "The Simons Observatory: Astro2020 Decadal Project Whitepaper", Bull. Am. Astron. Soc. **51**, 147 (2019).

[6] P. Ade, J. Aguirre, Z. Ahmed, et al., "The Simons Observatory: Science goals and forecasts", Journal of Cosmology and Astroparticle Physics **2019**, 10.1088/1475-7516/2019/02/056 (2019).

[7] J. Aleksić, S. Ansoldi, L. A. Antonelli, et al., "Measurement of the Crab Nebula spectrum over three decades in energy with the MAGIC telescopes", Journal of High Energy Astrophysics **5-6**, 30 (2015).

[8] A. Ali, S. Adachi, K. Arnold, et al., "Small Aperture Telescopes for the Simons Observatory", Journal of Low Temperature Physics **200**, 461 (2020).

[9] L. Antony and C. Anthony, *Code for Anisotropies in the Microwave Background (CAMB)*, https://camb.info/.

[10] G. Arcadi, M. Dutra, P. Ghosh, et al., "The waning of the WIMP? A review of models, searches, and constraints", Eur. Phys. J. C **78**, 203 (2018).

[11] K. Arnold et al., "The bolometric focal plane array of the Polarbear CMB experiment", Proc. SPIE Int. Soc. Opt. Eng. **8452**, 84521D (2012).

[12] K. Arnold et al., "The POLARBEAR CMB polarization experiment", Proc. SPIE Int. Soc. Opt. Eng. **7741**, 77411E (2010).

[13] A. Arvanitaki, S. Dimopoulos, S. Dubovsky, N. Kaloper, and J. March-Russell, "String axiverse", Phys. Rev. D **81**, 123530 (2010).

[14] Atmospheric InfraRed Sounder (AIRS) database, https://airs.jpl.nasa.gov/data/.

[15] J. Aumont, L. Conversi, C. Thum, et al., "Measurement of the Crab nebula polarization at 90 GHz as a calibrator for CMB experiments", Astronomy & Astrophysics **514**, A70 (2010).

[16] J. Aumont, J. F. Macı´as-Pérez, A. Ritacco, N. Ponthieu, and A. Mangilli, "Absolute calibration of the polarisation angle for future CMB *B*-mode experiments from current and future measurements of the Crab nebula", Astron. Astrophys. **634**, A100 (2020).

[17] J. E. Austermann, K. A. Aird, J. A. Beall, et al., "SPTpol: an instrument for CMB polarization measurements with the South Pole Telescope", Proc. SPIE Int. Soc. Opt. Eng. **8452**, 84521E (2012).

[18] N. Banik and P. Sikivie, "Axions and the galactic angular momentum distribution", Phys. Rev. D **88**, 123517 (2013).

[19] D. Barkats, C. Bischoff, P. Farese, et al., "Cosmic Microwave Background Polarimetry Using Correlation Receivers with the PIQUE and CAPMAP Experiments", The Astrophysical Journal Supplement Series **159**, 1 (2005).

[20] A. Basu, J. Goswami, D. J. Schwarz, and Y. Urakawa, "Searching for Axionlike Particles under Strong Gravitational Lenses", Physical Review Letters **126**, 191102 (2021).

[21] W. Becker and B. Aschenbach, "ROSAT HRI Observations of the Crab Pulsar: an Improved Temperature Upper Limit for PSR 0531+21", NATO Sci. Ser. C **450**, 47 (1995).

[22] C. L. Bennett, A. J. Banday, K. M. Górski, et al., "Four-Year COBE DMR Cosmic Microwave Background Observations: Maps and Basic Results", The Astrophysical Journal **464**, L1 (1996).

[23] Bersanelli, M., Mandolesi, N., Butler, R. C., et al., "Planck pre-launch status: Design and description of the Low Frequency Instrument", A&A **520**, A4 (2010).

[24] BICEP/Keck Collaboration, "BICEP/ Keck XIV: improved constraints on axionlike polarization oscillations in the cosmic microwave background", Physical Review D **105**, 022006 (2022).

[25] BICEP/Keck Collaboration, "BICEP/Keck XII: constraints on axionlike polarization oscillations in the cosmic microwave background", Physical Review D **103**, 042002 (2021).

[26] BICEP/Keck Collaboration, "Improved Constraints on Primordial Gravitational Waves using Planck, WMAP, and BICEP/Keck Observations through the 2018 Observing Season", Phys. Rev. Lett. **127**, 151301 (2021).

[27] J. Bovy and S. Tremaine, "On the local dark matter density", The Astrophysical Journal **756**, 89 (2012).

[28] S. Bryan and The SPIDER Collaboration, "A cryogenic rotation stage with a large clear aperture for the half-wave plates in the Spider instrument", Review of Scientific Instruments **87**, 14501 (2016).

[29] N. Bucciantini, R. Ferrazzoli, M. Bachetti, et al., "Simultaneous space and phase resolved X-ray polarimetry of the Crab pulsar and nebula", Nature Astronomy **7**, 602 (2023).

[30] S. M. Carroll, G. B. Field, and R. Jackiw, "Limits on a Lorentz- and parity-violating modification of electrodynamics", Physical Review D **41**, 1231 (1990).

[31] CAST Collaboration, "New CAST limit on the axion–photon interaction", Nature Physics **13**, 584 (2017).

[32] A. Castillo, J. Martin-Camalich, J. Terol-Calvo, et al., "Searching for dark-matter waves with PPTA and QUIJOTE pulsar polarimetry", Journal of Cosmology and Astroparticle Physics **2022**, 014 (2022).

[33] G. P. Centers et al., "Stochastic fluctuations of bosonic dark matter", Nature Commun. **12**, 7321 (2021).

[34] M.-T. Chen, C.-T. Li, Y.-J. Hwang, et al., "AMiBA: Broadband Heterodyne CMB Interferometry", The Astrophysical Journal **694**, 1664 (2009).

[35] S. Chigusa, T. Moroi, and K. Nakayama, "Signals of axion like dark matter in time dependent polarization of light", Physics Letters B **803**, 135288 (2020).

[36] S. E. Church, "Predicting residual levels of atmospheric sky noise in ground-based observations of the cosmic background radiation", Monthly Notices of the Royal Astronomical Society **272**, 551 (1995).

[37] M. Cicoli, M. D. Goodsell, and A. Ringwald, "The type IIB string axiverse and its low-energy phenomenology", Journal of High Energy Physics **2012**, 146 (2012).

[38] D. Clowe, M. Bradač, A. H. Gonzalez, et al., "A Direct Empirical Proof of the Existence of Dark Matter*", The Astrophysical Journal **648**, L109 (2006).

[39] K. D. Crowley, P. Dow, J. E. Shroyer, et al., "The Simons Observatory: A large-diameter truss for a refracting telescope cooled to 1 K", Review of Scientific Instruments **93**, 055106 (2022).

[40] A. Derevianko, "Detecting dark-matter waves with a network of precision-measurement tools", Physical Review A **97**, 042506 (2018).

[41] DES Collaboration, "Constraints on Dark Matter Properties from Observations of Milky Way Satellite Galaxies", Physical Review Letters **126**, 091101 (2021).

[42] M. Dine, W. Fischler, and M. Srednicki, "A simple solution to the strong CP problem with a harmless axion", Physics Letters B **104**, 199 (1981).

[43] C. Dragone, "Offset multireflector antennas with perfect pattern symmetry and polarization discrimination", The Bell System Technical Journal **57**, 2663 (1978).

[44] R. Dünner, M. Hasselfield, T. A. Marriage, et al., "The atacama cosmology telescope: data characterization and mapmaking", The Astrophysical Journal **762**, 10 (2012).

[45] T. Eftekhari, K. Stovall, J. Dowell, F. K. Schinzel, and G. B. Taylor, "A Low Frequency Survey of Giant Pulses from the Crab Pulsar", The Astrophysical Journal **829**, 62 (2016).

[46] S. W. Ellingson, T. E. Clarke, J. Craig, et al., "Observations of Crab Giant Pulses in 20-84 MHz using LWA1", Astrophys. J. **768**, 136 (2013).

[47] J. Errard, P. Ade, Y. Akiba, et al., "MODELING ATMOSPHERIC EMISSION for CMB GROUND-BASED OBSERVATIONS", Astrophysical Journal **809**, 10.1088/0004-637X/809/1/63 (2015).

[48] T. Essinger-Hileman, A. Kusaka, J. W. Appel, et al., "Systematic effects from an ambient-temperature, continuously-rotating half-wave plate", Review of Scientific Instruments **87**, 10.1063/1.4962023 (2016).

[49] M. A. Fedderke, P. W. Graham, and S. Rajendran, "Axion dark matter detection with CMB polarization", Physical Review D **100**, 015040 (2019).

[50] H. Feng, H. Li, X. Long, et al., "Re-detection and a possible time variation of soft X-ray polarization from the Crab", Nature Astronomy **4**, 511 (2020).

[51] E. G. M. Ferreira, "Ultra-Light Dark Matter", Astronomy and Astrophysics Review **29**, 7 (2021).

[52] D. J. Fixsen, E. S. Cheng, J. M. Gales, et al., "The cosmic microwave background spectrum from the full cobe* firas data set", The Astrophysical Journal **473**, 576 (1996).

[53] J. W. Foster, N. L. Rodd, and B. R. Safdi, "Revealing the Dark Matter Halo with Axion Direct Detection", Phys. Rev. D **97**, 123006 (2018).

[54] K. Freese, J. A. Frieman, and A. V. Olinto, "Natural inflation with pseudo Nambu-Goldstone bosons", Phys. Rev. Lett. **65**, 3233 (1990).

[55] T. Fujino, S. Takakura, Y. Chinone, et al., "Characterization of a half-wave plate for cosmic microwave background circular polarization measurement with POLARBEAR", Review of Scientific Instruments **94**, 10.1063/5.0140088 (2023).

[56] T. Fujita, R. Tazaki, and K. Toma, "Hunting Axion Dark Matter with Protoplanetary Disk Polarimetry", Physical Review Letters **122**, 191101 (2019).

[57] N. Galitzki et al., "The Simons Observatory: Instrument Overview", Proc. SPIE Int. Soc. Opt. Eng. **10708**, 1070804 (2018).

[58] N. Galitzki et al., *The Simons Observatory: Integration and testing of the first small aperture telescope, SAT-MF1*, In preparation.

[59] J. E. Golec, J. J. McMahon, A. M. Ali, et al., "Design and fabrication of metamaterial anti-reflection coatings for the Simons Observatory", Proc. SPIE Int. Soc. Opt. Eng. **11451**, 114515T (2020).

[60] D. A. Green, "A revised catalogue of 294 Galactic supernova remnants", Journal of Astrophysics and Astronomy **40**, 36, 36 (2019).

[61] R. Gualtieri, J. P. Filippini, P. A. R. Ade, et al., "SPIDER: CMB Polarimetry from the Edge of Space", Journal of Low Temperature Physics **193**, 1112 (2018).

[62] A. H. Guth, "Inflationary universe: a possible solution to the horizon and flatness problems", Phys. Rev. D **23**, 347 (1981).

[63] A. H. Guth, M. P. Hertzberg, and C. Prescod-Weinstein, "Do dark matter axions form a condensate with long-range correlation?", Phys. Rev. D **92**, 103513 (2015).

[64] D. Harari and P. Sikivie, "Effects of a Nambu-Goldstone boson on the polarization of radio galaxies and the cosmic microwave background", Physics Letters B **287**, 65 (1990).

[65] K. Harrington, R. Datta, K. Osumi, et al., "Two Year Cosmology Large Angular Scale Surveyor (CLASS) Observations: Long Timescale Stability Achieved with a Front-end Variable-delay Polarization Modulator at 40 GHz", The Astrophysical Journal **922**, 212 (2021).

[66] S. W. Henderson et al., "Highly-multiplexed microwave SQUID readout using the SLAC microresonator radio frequency (SMuRF) electronics for future CMB and sub-millimeter surveys", Proc. SPIE Int. Soc. Opt. Eng. **10708**, 1070819 (2018).

[67] J. J. Hester, "The Crab Nebula: An Astrophysical Chimera", Annual Review of Astronomy and Astrophysics **46**, 127 (2008).

[68] C. A. Hill, A. Kusaka, P. Ashton, et al., "A cryogenic continuously rotating half-wave plate mechanism for the POLARBEAR-2b cosmic microwave background receiver", Review of Scientific Instruments **91**, 124503 (2020).

[69] C. A. Hill, S. Beckman, Y. Chinone, et al., "Design and development of an ambient-temperature continuously-rotating achromatic half-wave plate for CMB polarization modulation on the POLARBEAR-2 experiment", Proc. SPIE Int. Soc. Opt. Eng. **9914**, 99142U (2016).

[70] R. Hlozek, D. Grin, D. J. E. Marsh, and P. G. Ferreira, "A search for ultralight axions using precision cosmological data", Phys. Rev. D **91**, 103512 (2015).

[71] W. Hu, R. Barkana, and A. Gruzinov, "Fuzzy Cold Dark Matter: The Wave Properties of Ultralight Particles", Phys. Rev. Lett. **85**, 1158 (2000).

[72] W. Hu and S. Dodelson, "Cosmic Microwave Background Anisotropies", Annual Review of Astronomy and Astrophysics **40**, 171 (2002).

[73] W. Hu and M. White, "A cmb polarization primer", New Astronomy **2**, 323 (1997).

[74] L. Hui, "Wave Dark Matter", Annual Review of Astronomy and Astrophysics **59**, 247 (2021).

[75] L. Hui, J. P. Ostriker, S. Tremaine, and E. Witten, "Ultralight scalars as cosmological dark matter", Phys. Rev. D **95**, 043541 (2017).

[76] Y. Inoue, T. Matsumura, M. Hazumi, et al., "Cryogenic infrared filter made of alumina for use at millimeter wavelength", Applied Optics **53**, 1727 (2014).

[77] V. Iršič, M. Viel, M. G. Haehnelt, J. S. Bolton, and G. D. Becker, "First Constraints on Fuzzy Dark Matter from Lyman-α Forest Data and Hydrodynamical Simulations", Physical Review Letters **119**, 031302 (2017).

[78] N. Jarosik, C. L. Bennett, M. Halpern, et al., "Design, Implementation, and Testing of the Microwave Anisotropy Probe Radiometers", The Astrophysical Journal Supplement Series **145**, 413 (2003).

[79] B. R. Johnson, J. Collins, et al., "MAXIPOL: Cosmic Microwave Background Polarimetry Using a Rotating Half-Wave Plate", The Astrophysical Journal **665**, 42 (2007).

[80] B. R. Johnson, F. Columbro, D. Araujo, et al., "A large-diameter hollow-shaft cryogenic motor based on a superconducting magnetic bearing for millimeter-wave polarimetry", Review of Scientific Instruments **88**, 105102 (2017).

[81] M. Kam, S. Trippe, D.-Y. Byun, et al., "Using the Crab Nebula as Polarization Angle Calibrator for the Korean VLBI Network", Journal of The Korean Astronomical Society **56**, 1 (2023).

[82] M. Kamionkowski, A. Kosowsky, and A. Stebbins, "A Probe of Primordial Gravity Waves and Vorticity", Physical Review Letters **78**, 2058 (1997).

[83] M. Kamionkowski, A. Kosowsky, and A. Stebbins, "Statistics of cosmic microwave background polarization", Phys. Rev. D **55**, 7368 (1997).

[84] D. L. Kaplan, S. Chatterjee, B. M. Gaensler, and J. Anderson, "A Precise Proper Motion for the Crab Pulsar, and the Difficulty of Testing Spin-Kick Alignment for Young Neutron Stars", The Astrophysical Journal **677**, 1201 (2008).

[85] Z. Kermish et al., "The POLARBEAR Experiment", Proc. SPIE Int. Soc. Opt. Eng. **8452**, 1C (2012).

[86] M. Kesden, A. Cooray, and M. Kamionkowski, "Separation of Gravitational-Wave and Cosmic-Shear Contributions to Cosmic Microwave Background Polarization", Physical Review Letters **89**, 11304 (2002).

[87] J. E. Kim, "Weak-Interaction Singlet and Strong CP Invariance", Phys. Rev. Lett. **43**, 103 (1979).

[88] K. Kiuchi et al., *The simons observatory: cryogenic optics tube for small aperture telescopes*, In preparation.

[89] K. Kiuchi, S. Adachi, A. M. Ali, et al., "The Simons Observatory Small Aperture Telescope overview", Proc. SPIE Int. Soc. Opt. Eng., 162 (2020).

[90] J. Klein and The EBEX Collaboration, "A cryogenic half-wave plate polarimeter using a superconducting magnetic bearing", Proc. SPIE Int. Soc. Opt. Eng. **8150**, 815004 (2011).

[91] J. R. Klein and A. Roodman, "Blind analysis in nuclear and particle physics", Annual Review of Nuclear and Particle Science **55**, 141 (2005).

[92] L. Knox and Y.-S. Song, "Limit on the Detectability of the Energy Scale of Inflation", Physical Review Letters **89**, 11303 (2002).

[93] C. S. Kochanek, B. J. Shappee, K. Z. Stanek, et al., "The All-Sky Automated Survey for Supernovae (ASAS-SN) Light Curve Server v1.0", Publications of the Astronomical Society of the Pacific **129**, 104502 (2017).

[94] E. Komatsu, "New physics from the polarized light of the cosmic microwave background", Nature Rev. Phys. **4**, 452 (2022).

[95] B. J. Koopman, J. Lashner, L. J. Saunders, et al., "The Simons Observatory: Overview of data acquisition, control, monitoring, and computer infrastructure", Proc. SPIE Int. Soc. Opt. Eng. **11452**, 1145208 (2020).

[96] T. Kouzu, M. S. Tashiro, Y. Terada, et al., "Spectral Variation of Hard X-Ray Emission from the Crab Nebula with the Suzaku Hard X-Ray Detector", Publications of the Astronomical Society of Japan **65**, 10.1093/PASJ/65.4.74 (2013).

[97] J. M. Kovac and D. Barkats, "CMB from the South Pole: Past, Present, and Future", arXiv:0707.1075 [astro-ph] (2007).

[98] H. A. Krimm, S. T. Holland, R. H. D. Corbet, et al., "The Swift/BAT Hard X-ray Transient Monitor", The Astrophysical Journal Supplement Series **209**, 14 (2013).

[99] A. Kusaka, T. Essinger-Hileman, et al., "Modulation of cosmic microwave background polarization with a warm rapidly rotating half-wave plate on the Atacama B-Mode Search instrument", Review of Scientific Instruments **85**, 24501 (2014).

[100] A. Kusaka, J. Appel, T. Essinger-Hileman, et al., "Results from the Atacama B-mode Search (ABS) experiment", Journal of Cosmology and Astroparticle Physics **2018**, 5 (2018).

[101] K. Lee, J. Choi, R. T. Génova-Santos, et al., "GroundBIRD: A CMB Polarization Experiment with MKID Arrays", Journal of Low Temperature Physics **200**, 384 (2020).

[102] E. M. Leitch, J. M. Kovac, N. W. Halverson, et al., "Degree Angular Scale Interferometer 3 Year Cosmic Microwave Background Polarization Results", The Astrophysical Journal **624**, 10 (2005).

[103] J.-M. Levy-Leblond, "Galilei Group and Nonrelativistic Quantum Mechanics", Journal of Mathematical Physics **4**, 776 (1963).

[104] Y. Li, K. Arnold, Z. Atkins, et al., "Assembly and integration process of the high-density detector array readout modules for the simons observatory", **199**, 985 (2020).

[105] A. Linde, "Inflationary Cosmology", in *Inflationary cosmology* (Springer Berlin Heidelberg, Berlin, Heidelberg, 2007), pp. 1–54.

[106] A. Linde, *Particle Physics and Inflationary Cosmology*, 2005.

[107] H. Liu, B. D. Elwood, M. Evans, and J. Thaler, "Searching for axion dark matter with birefringent cavities", Phys. Rev. D **100**, 023548 (2019).

[108] T. Liu, X. Lou, and J. Ren, "Pulsar Polarization Arrays", Phys. Rev. Lett. **130**, 121401 (2023).

[109] T. Liu, G. Smoot, and Y. Zhao, "Detecting axionlike dark matter with linearly polarized pulsar light", Physical Review D **101**, 063012 (2020).

[110] D. J. Marsh, "Axion cosmology", Physics Reports **643**, Axion cosmology, 1 (2016).

[111] R. Massey, T. Kitching, and J. Richard, "The dark matter of gravitational lensing", Reports on Progress in Physics **73**, 086901 (2010).

[112] F. J. Massey Jr., "The Kolmogorov-Smirnov Test for Goodness of Fit", Journal of the American Statistical Association **46**, 68 (1951).

[113] F. T. Matsuda et al., "Cross-polarization systematics due to Mizuguchi-Dragone condition breaking by a continuously rotating half-wave plate at prime focus in the Huan Tran telescope", Proc. SPIE Int. Soc. Opt. Eng. **10708**, 1070849 (2018).

[114] F. T. Matsuda, "Optics design development of the Simons Observatory Small Aperture Telescopes", Proc. SPIE Int. Soc. Opt. Eng. **11445**, 114456Z (2020).

[115] T. Matsumura, "A cosmic microwave background radiation polarimeter using superconducting magnetic bearings", PhD thesis (University of Minnesota, Minnesota, USA, 2006).

[116] M. Matsuoka, K. Kawasaki, S. Ueno, et al., "The MAXI Mission on the ISS: Science and Instruments for Monitoring All-Sky X-Ray Images", Publications of the Astronomical Society of Japan **61**, 999 (2009).

[117] H. McCarrick, E. Healy, Z. Ahmed, et al., "The simons observatory microwave squid multiplexing detector module design", The Astrophysical Journal **922**, 38 (2021).

[118] C. F. McKee, A. Parravano, and D. J. Hollenbach, "Stars, Gas, and Dark Matter in the Solar Neighborhood", The Astrophysical Journal **814**, 13 (2015).

[119] N. J. Miller, D. T. Chuss, T. A. Marriage, et al., "Recovery of Large Angular Scale CMB Polarization for Instruments Employing Variable-delay Polarization Modulators", The Astrophysical Journal **818**, 151 (2016).

[120] Y. Minami and E. Komatsu, "New Extraction of the Cosmic Birefringence from the Planck 2018 Polarization Data", Phys. Rev. Lett. **125**, 221301 (2020).

[121] Y. Mizugutch, M. Akagawa, and H. Yokoi, "Offset dual reflector antenna", in 1976 antennas and propagation society international symposium, Vol. 14 (1976), pp. 2–5.

[122] L. Moncelsi, P. A. R. Ade, F. E. Angilè, et al., "Empirical modelling of the BLASTPol achromatic half-wave plate for precision submillimetre polarimetry", Monthly Notices of the Royal Astronomical Society **437**, 2772 (2013).

[123] M. Monelli, E. Komatsu, A. E. Adler, et al., "Impact of half-wave plate systematics on the measurement of cosmic birefringence from CMB polarization", Journal of Cosmology and Astroparticle Physics **2023**, 034 (2023).

[124] P. Moran, A. Shearer, R. P. Mignani, et al., "Optical polarimetry of the inner Crab nebula and pulsar", Monthly Notices of the Royal Astronomical Society **433**, 2564 (2013).

[125] T. W. Morris, R. Bustos, E. Calabrese, et al., "The Atacama Cosmology Telescope: Modeling bulk atmospheric motion", Phys. Rev. D **105**, 042004 (2022).

[126] S. Moyerman, E. Bierman, P. A. R. Ade, et al., "Scientific verification of Faraday Rotation Modulators: Detection of diffuse polarized Galactic emission", The Astrophysical Journal **765**, 64 (2013).

[127] M. Murata, H. Nakata, K. Iijima, et al., "The Simons Observatory: A fully remote controlled calibration system with a sparse wire grid for cosmic microwave background telescopes", arXiv:2309.02035 [astro-ph] (2023).

[128] K. Nagano, T. Fujita, Y. Michimura, and I. Obata, "Axion dark matter search with interferometric gravitational wave detectors", Physical Review Letters **123**, 111301 (2019).

[129] H. Nakatsuka, S. Morisaki, T. Fujita, et al., "Stochastic effects on observation of ultralight bosonic dark matter", 10.48550/arxiv.2205.02960 (2022).

[130] J. Neyman, "Outline of a Theory of Statistical Estimation Based on the Classical Theory of Probability", Philosophical Transactions of the Royal Society of London. Series A, Mathematical and Physical Sciences **236**, 333 (1937).

[131] R. O'Brient, P. Ade, K. Arnold, et al., "A dual-polarized multichroic antenna-coupled TES bolometer for terrestrial CMB Polarimetry", Proc. SPIE Int. Soc. Opt. Eng. **7741**, 77410J (2010).

[132] C. W. O'Dell, B. G. Keating, A. de Oliveira-Costa, et al., "CMB polarization at large angular scales: Data analysis of the POLAR experiment", Phys. Rev. D **68**, 042002 (2003).

[133] C. O'Hare, *cajohare/AxionLimits: AxionLimits*, https://cajohare.github.io/AxionLimits/, version v1.0, July 2020.

[134] I. Obata, T. Fujita, and Y. Michimura, "Optical Ring Cavity Search for Axion Dark Matter", Physical Review Letters **121**, 161301 (2018).

[135] A. Otárola, T. Travouillon, M. Schöck, et al., "Thirty Meter Telescope Site Testing X: Precipitable Water Vapor", Publications of the Astronomical Society of the Pacific **122**, 470 (2010).

[136] L. Page, G. Hinshaw, E. Komatsu, et al., "Three-Year Wilkinson Microwave Anisotropy Probe (WMAP) Observations: Polarization Analysis", The Astrophysical Journal Supplement Series **170**, 335 (2007).

[137] S. Pancharatnam, "Achromatic combinations of birefringent plates", Proc. Indian Acad. Sci. A **41**, 137 (1955).

[138] S. C. Parshley, M. Niemack, R. Hills, et al., "The optical design of the six-meter CCAT-prime and Simons Observatory telescopes", Proc. SPIE Int. Soc. Opt. Eng. **10700**, 1070041 (2018).

[139] I. de Pater, "A comparison of the radio data and model calculations of Jupiter's synchrotron radiation, 1. The high energy electron distribution in Jupiter's inner magnetosphere", Journal of Geophysical Research **86**, 3397 (1981).

[140] I. de Pater and D. E. Dunn, "VLA observations of Jupiter's synchrotron radiation at 15 and 22 GHz", Icarus **163**, 449 (2003).

[141] A. Payez, C. Evoli, T. Fischer, et al., "Constraining the photon coupling of ultra-light dark-matter axion-like particles by polarization variations of parsec-scale jets in active galaxies", Journal of Cosmology and Astroparticle Physics **2019**, 059 (2019).

[142] A. Payez, C. Evoli, T. Fischer, et al., "Revisiting the SN1987A gamma-ray limit on ultralight axion-like particles", Journal of Cosmology and Astroparticle Physics **2015**, 006 (2015).

[143] R. D. Peccei and H. R. Quinn, "CP Conservation in the Presence of Pseudoparticles", Phys. Rev. Lett. **38**, 1440 (1977).

[144] A. A. Penzias and R. G. Wilson, "A measurement of excess antenna temperature at 4080-mc/s", The Astrophysical Journal **142**, 419 (1965).

[145] M. J. Persky, "Review of black surfaces for space-borne infrared systems", Review of Scientific Instruments **70**, 2193 (1999).

[146] M. A. Petroff, J. R. Eimer, K. Harrington, et al., "Two-year Cosmology Large Angular Scale Surveyor (CLASS) Observations: A First Detection of Atmospheric Circular Polarization at Q band", The Astrophysical Journal **889**, 120 (2020).

[147] Planck Collaboration, "Planck 2018 results - VI. Cosmological parameters", A&A **641**, A6 (2020).

[148] Planck Collaboration, "Planck 2018 results - XI. Polarized dust foregrounds", A&A **641**, A11 (2020).

[149] Polarbear Collaboration, "A Measurement of the Cosmic Microwave Background B -mode Polarization Power Spectrum at Subdegree Scales from Two Years of polarbear Data", The Astrophysical Journal **848**, 121 (2017).

[150] Polarbear Collaboration, "A Measurement of the Cosmic Microwave Background B-Mode Polarization Power Spectrum at Sub-Degree Scales with POLARBEAR", The Astrophysical Journal **794**, 171 (2014).

[151] Polarbear Collaboration, "A Measurement of the Degree-scale CMB B-mode Angular Power Spectrum with Polarbear", The Astrophysical Journal **897**, 55 (2020).

[152] Polarbear Collaboration, "Constraints on axionlike polarization oscillations in the cosmic microwave background with POLARBEAR", Phys. Rev. D **108**, 043017 (2023).

[153] Polarbear Collaboration, "Improved Upper Limit on Degree-scale CMB B-mode Polarization Power from the 670 Square-degree POLARBEAR Survey", The Astrophysical Journal **931**, 101 (2022).

[154] Polarbear Collaboration, "Search for axion-like polarization oscillation in Crab nebula with Polarbear", (In preparation).

[155] QUIET Collaboration et al., "First Season QUIET Observations: Measurements of CMB Polarization Power Spectra at 43 GHz in the Multipole Range $25 \leq \ell \leq 475$", The Astrophysical Journal **741**, 111 (2011).

[156] QUIET Collaboration et al., "Second Season QUIET Observations: Measurements of the CMB Polarization Power Spectrum at 95 GHz", The Astrophysical Journal **760**, 145 (2012).

[157] Range Commanders Council, *IRIG Standard 200-16: IRIG Serial Time Code Formats*, Sept. 2016.

[158] M. J. Rees, "Polarization and spectrum of the primeval radiation in an anisotropic universe.", Astrophys. J. **153**, 10.1086/180208 (1968).

[159] V. C. Rubin, N. Thonnard, and K. Jr.FordW., “Extended rotation curves of high-luminosity spiral galaxies. I - The angle between the rotation axis of the nucleus and the outer disk of NGC 3672”, The Astrophysical Journal **217**, 10.1086/182526 (1977).

[160] K. Sakaguri, M. Hasegawa, Y. Sakurai, C. Hill, and A. Kusaka, “Broadband multi-layer anti-reflection coatings with mullite and duroid for half-wave plates and alumina filters for cmb polarimetry”, Journal of Low Temperature Physics **209**, 1264 (2022).

[161] Y. Sakurai, T. Matsumura, N. Ktayama, et al., “Development of a Cryogenic Remote Sensing Thermometer for CMB Polarization Experiment”, ISSTT2018, 169 (2018).

[162] Y. Sakurai, T. Matsumura, N. Katayama, et al., “Design and development of a polarization modulator unit based on a continuous rotating half-wave plate for LiteBIRD”, Proc. SPIE Int. Soc. Opt. Eng. **10708**, 107080E (2018).

[163] Y. Sakurai, P. Ashton, A. Kusaka, et al., “Half-meter Scale Superconducting Magnetic Bearing for Cosmic Microwave Background Polarization Experiments”, Journal of Physics: Conference Series **1590**, 012060 (2020).

[164] Y. Sakurai, T. Matsumura, N. Katayama, et al., “Breadboard model of the polarization modulator unit based on a continuously rotating half-wave plate for the low-frequency telescope of the LiteBIRD space mission”, Proc. SPIE Int. Soc. Opt. Eng. **11453**, 114534E (2020).

[165] Y. Sakurai, T. Matsumura, H. Kataza, S. Utsunomiya, and R. Yamamoto, “Estimation of the Heat Dissipation and the Rotor Temperature of Superconducting Magnetic Bearing Below 10 K”, IEEE Transactions on Applied Superconductivity **27**, 1 (2017).

[166] M. Salatino, J. Lashner, M. Gerbino, S. M. Simon, J. Didier, et al., “Studies of systematic uncertainties for Simons Observatory: polarization modulator related effects”, Proc. SPIE Int. Soc. Opt. Eng. **10708**, 1070848 (2018).

[167] U. Seljak and M. Zaldarriaga, “Direct Signature of Evolving Gravitational Potential from Cosmic Microwave Background”, Physical Review D **60**, 10.1103/PhysRevD.60.043504 (1999).

[168] U. Seljak and C. M. Hirata, “Gravitational lensing as a contaminant of the gravity wave signal in the CMB”, Physical Review D **69**, 43005 (2004).

[169] S. di Serego Alighieri, F. Finelli, and M. Galaverni, “Limits on Cosmological Birefringence from the UV Polarization of Distant Radio Galaxies”, The Astrophysical Journal **715**, 33 (2010).

[170] B. J. Shappee, J. L. Prieto, D. Grupe, et al., “The Man Behind the Curtain: X-rays Drive the UV through NIR Variability in the 2013 AGN Outburst in NGC 2617”, The Astrophysical Journal **788**, 48 (2014).

[171] M. Shifman, A. Vainshtein, and V. Zakharov, “Can confinement ensure natural CP invariance of strong interactions?”, Nuclear Physics B **166**, 493 (1980).

[172] M. Shimon, B. Keating, N. Ponthieu, and E. Hivon, “CMB polarization systematics due to beam asymmetry: Impact on inflationary science”, Phys. Rev. D **77**, 083003 (2008).

[173] P. Sikivie, “Experimental Tests of the "Invisible" Axion”, Physical Review Letters **49**, 1413 (1981).

[174] P. Sikivie and J. R. Ipser, “Phase-space structure of cold dark matter halos”, Physics Letters B **291**, 288 (1992).

[175] P. Sikivie and Q. Yang, “Bose-Einstein Condensation of Dark Matter Axions”, Phys. Rev. Lett. **103**, 111301 (2009).

[176] Simons Observatory Collaboration, *simonsobs/bolocalc-so-model*, https://github.com/simonsobs/bolocalc-so-model/, version v3r7.

[177] J. Sisk-Reynés, J. H. Matthews, C. S. Reynolds, et al., “New constraints on light axion-like particles using Chandra transmission grating spectroscopy of the powerful cluster-hosted quasar H1821 + 643”, MNRAS **510**, 1264 (2022).

[178] S. Sivertsson, H. Silverwood, J. I. Read, G. Bertone, and P. Steger, “The local dark matter density from SDSS-SEGUE G-dwarfs”, mnras **478**, 1677 (2018).

[179] SPTpol Collaboration, “Searching for axionlike time-dependent cosmic birefringence with data from SPT-3G”, Phys. Rev. D **106**, 042011 (2022).

[180] J. Y. Suen, M. T. Fang, and P. M. Lubin, “Global Distribution of Water Vapor and Cloud Cover—Sites for High-Performance THz Applications”, IEEE Transactions on Terahertz Science and Technology **4**, 86 (2014).

[181] A. Suzuki, P. Ade, Y. Akiba, et al., “The Polarbear-2 and the Simons Array Experiments”, Journal of Low Temperature Physics **184**, 805 (2016).

[182] D. S. Swetz, P. A. R. Ade, M. Amiri, et al., “Overview of the Atacama Cosmology Telescope: Receiver, instrumentation, and telescope systems”, The Astrophysical Journal Supplement Series **194**, 41 (2011).

[183] Y. D. Takahashi, P. A. R. Ade, D. Barkats, et al., “Characterization of the BICEP Telescope for High-precision Cosmic Microwave Background Polarimetry”, ApJ **711**, 1141 (2010).

[184] S. Takakura, M. A. O. Aguilar-Faúndez, Y. Akiba, et al., “Measurements of Tropospheric Ice Clouds with a Ground-based CMB Polarization Experiment, POLARBEAR”, The Astrophysical Journal **870**, 102 (2019).

[185] S. Takakura, “Characterization of a continuous polarization modulator using a half-wave plate for measurements of degree-scale cosmic microwave background with the POLARBEAR experiment”, PhD thesis (Osaka University, 2017).

[186] S. Takakura, M. Aguilar, Y. Akiba, et al., “Performance of a continuously rotating half-wave plate on the POLARBEAR telescope”, Journal of Cosmology and Astroparticle Physics **2017**, 008 (2017).

[187] D. Tanabe et al., “High-precision temperature monitoring system for room-temperature equipment in astrophysical observations”, J. Astron. Telesc. Instrum. Syst. **8**, 036003 (2022).

[188] The EBEX Collaboration, “The EBEX Balloon-borne Experiment—Optics, Receiver, and Polarimetry”, The Astrophysical Journal Supplement Series **239**, 7 (2018).

[189] The Planck Collaboration, “Planck 2018 results. XI. Polarized dust foregrounds”, Astronomy & Astrophysics, 10.1051/0004-6361/201832618 (2018).

[190] The Simons Observatory collaboration, “The Simons Observatory: Science goals and forecasts”, JCAP **02**, 056 (2019).

[191] P. Tiwari, X. D. Wu, S. R. Foltyn, et al., “Study of high-quality epitaxial YBCO thin films grown directly on y-cut LiNbO3”, Journal of Electronic Materials **25**, 131 (1996).

[192] H. Tran, A. Lee, S. Hanany, M. Milligan, and T. Renbarger, “Comparison of the crossed and the Gregorian Mizuguchi-Dragone for wide-field millimeter-wave astronomy”, Appl. Opt. **47**, 103 (2008).

[193] M. Tristram, A. J. Banday, K. M. Górski, et al., “Improved limits on the tensor-to-scalar ratio using bicep and *planck* data”, Phys. Rev. D **105**, 083524 (2022).

[194] S. Uros and Z. Matias, “Signature of Gravity Waves in Polarization of the Microwave Background”, Physical Review Letters **78**, 2054 (1997).

[195] P. Vaníček, “Approximate spectral analysis by least-squares fit”, Astrophysics and Space Science **4**, 387 (1969).

[196] J. L. Weiland, N. Odegard, R. S. Hill, et al., “Seven-Year Wilkinson Microwave Anisotropy Probe (WMAP) Observations: Planets and Celestial Calibration Sources”, ApJS **192**, 19 (2011).

[197] S. Weinberg, “A New Light Boson?”, Phys. Rev. Lett. **40**, 223 (1978).

[198] Wiesemeyer, H., Thum, C., Morris, D., Aumont, J., and Rosset, C., “A sensitive upper limit to the circular polarization of the Crab nebula at λ3mm”, A&A **528**, A11 (2011).

[199] D. W. Wisander, L. P. Ludwig, and R. L. Johnson, “Wear and Friction of Various Polymer Laminates in Liquid Nitrogen and in Liquid Hydrogen.”, Materials Science, Engineering (1966).

[200] E. Witten, “Some properties of O(32) superstrings”, Physics Letters B **149**, 351 (1984).

[201] Z. Xu, S. Adachi, P. Ade, et al., “The Simons Observatory: The Large Aperture Telescope (LAT)”, Research Notes of the AAS **5**, 100 (2021).

[202] K. Yamada, B. Bixler, Y. Sakurai, et al., “The Simons Observatory: Cryogenic Half Wave Plate Rotation Mechanism for the Small Aperture Telescopes”, arXiv:2309.14803 [astro-ph] (2023).

[203] M. Zaldarriaga and U. Seljak, “Gravitational lensing effect on cosmic microwave background polarization”, Physical Review D **58**, 23003 (1998).

[204] M. Zaldarriaga and U. Seljak, “An All-Sky Analysis of Polarization in the Microwave Background”, Physical Review D **55**, 1830 (1997).

[205] A. P. Zhitnitskii, “Possible suppression of axion-hadron interactions”, Sov. J. Nucl. Phys. (Engl. Transl.); (United States) **31:2** (1980).

[206] N. Zhu, T. Bhandarkar, G. Coppi, et al., “The Simons Observatory Large Aperture Telescope Receiver”, The Astrophysical Journal Supplement Series **256**, 23 (2021).

[207] F. Zwicky, “Die Rotverschiebung von extragalaktischen Nebeln”, Helvetica Physica Acta. **6**, 110 (1933).